

Multifunctional hydrogels with injectable, self-healing, and shape-morphing capabilities for biomedical applications

*A research work submitted for
Sun Pharma Science Foundation research fellowship*

by

Pritiranjana Mondal



**Department of Materials Engineering
Indian Institute of Science
Bangalore-560012, India**

August 2024

Declaration

I, Pritiranjana Mondal, hereby declare that I am the first (main) author of this research work titled “*Multifunctional hydrogels with injectable, self-healing, and shape-morphing capabilities for biomedical applications*” and that the work reported here has been carried out by me at the Department of Materials Engineering, Indian Institute of Science, Bangalore, India, under the supervision of Prof. Kaushik Chatterjee.

August 2024

Indian Institute of Science, Bangalore

A rectangular box containing a handwritten signature in dark ink. The signature is written in a cursive style and reads "Pritiranjana Mondal".

Pritiranjana Mondal

Abstract of the research work:

In recent years, there has been a notable surge in interest surrounding implantable biomaterials due to their potential applications in treating physical defects and traumas. Hydrogels have garnered growing attention among implantable biomaterials due to their favorable rheological properties and adjustable structures. However, conventional hydrogel materials are prone to mechanical failures and cause patient discomfort during routine operations, which are significant challenges. This thesis presents novel findings on the development of hydrogels for biomedical applications that are endowed with superior attributes such as injectability, self-healing, and the ability to process by three-dimensional (3D) printing.

To address these shortcomings, hydrogels endowed with injectability and self-healing capabilities, enabling them to recover their structural integrity, offer numerous advantages such as vehicles for controlled, sustained, and localized delivery in a minimally invasive manner for biomedical applications. The first part of this thesis focuses on the development of a novel generation of multifunctional polysaccharide-based injectable hydrogels through rational engineering with a prolonged lifespan due to their robust self-healing nature, thus tremendously enhancing their potential for clinical translation. These hydrogels are endowed with injectability and self-healing capabilities, enabling them to recover their structural integrity and offer numerous advantages over conventional hydrogels for biomedical applications, such as vehicles for controlled, sustained, and localized delivery in a minimally invasive manner. Furthermore, a generalized easy approach for surface modification of nanomaterials with a bioligand was developed to prepare a degradable polysaccharide-based injectable hydrogel that is shown to be multifunctional, including self-healing, flexible, and antibacterial properties for biomedical applications.

Another significant limitation in the current clinical scenario is the inability to fabricate complex, patient-specific geometries and tissue architectures that will find potential applications in *ex vivo* tissue models, patient-specific implants and tissue scaffolds, deployable devices, soft robotics, and drug delivery systems. Manufacturing of such structures necessitates the development of techniques offering precise spatial control with excellent resolution, and advanced manufacturing in the form of three-dimensional (3D) and four-dimensional (4D) printing offers such advantages, along with the added possibility of encapsulating biological agents (cells, peptides, drugs, etc.). The second part of the thesis presents work on a novel 4D (bio)printing approach that employs biocompatible and versatile biomaterial ink design to encode an innovative shape-morphing strategy that can facilitate the development of smart solutions for challenging biomedical challenges. Finally, the potential applications of additively manufactured hydrogel structures for healthcare are now being extended to new frontiers, such as human-machine interfaces, wearable medical devices, soft robotics, biosensors, and engineered living systems. To this end, a 3D printable hydrogels endowed with conducting and anti-freezing capabilities were developed, which successfully retained other functionalities and cytocompatibility. These reversible shape deformation in 3D printed constructs in this system, which offers possibilities for use in advanced biomedical applications under extreme temperature conditions.

Taken together, the work presented in this thesis is critically important for developing tuneable, multifunctional, affordable, self-healing, and injectable hydrogel systems and 4D printable ink and techniques that are expected to find applications in healthcare, biosensors, deployable devices, and soft robotics for clinical translation.

Background and justification of the research work

In recent years, there has been a notable surge in engineering a new generation of resorbable biomaterials as implants to regenerate tissues and organs that are non-functional due to diseases, congenital defects, and traumas. Hydrogels have garnered much attention among this new class of biomaterials due to their favorable rheological properties and tunability while offering a tissue-like hydrated cellular microenvironment. However, the performance of conventional hydrogels is often limited by mechanical failures during routine procedures, which are significant impediments to clinical success. Hydrogels endowed with injectability and self-healing capabilities can overcome these limitations, owing to their ability to recover their structural integrity post-damage, thus offering numerous advantages for biomedical applications. Novel formulations of self-healing injectable hydrogel systems with 3D printability are highly sought-after for three-dimensional (3D) printing. Based on dynamic and reversible chemical bonding, these hydrogels may exhibit shear thinning behavior. These distinctive features of the emerging class of hydrogels provide significant advantages over conventional hydrogels. Most notably, they can be administered in a locally targeted and minimally invasive manner using a narrow syringe, obviating the need for invasive surgical procedures. Consequently, injected hydrogels play a pivotal role in biomedical applications through several mechanisms, including spatiotemporally controlled delivery of cells or therapeutic agents, providing mechanical support, and local recruitment and remodeling of injured or ruptured tissue. Therefore, multifunctional injectable hydrogels that synchronously perform on self-healing ability are in emerging demand in numerous bioengineering applications.

Additionally, another significant limitation in the current clinical scenario is the inability to fabricate complex, patient-specific geometries and tissue architectures that will find potential applications in ex vivo tissue models, patient-specific implants and tissue scaffolds, deployable

devices, soft robotics, and drug delivery systems to name a few. Manufacturing of such structures necessitates the development of techniques offering precise spatial control and excellent resolution, and additive manufacturing in the form of three-dimensional (3D) and four-dimensional (4D) printing offers such advantages, along with the added possibility of encapsulating biological agents (cells, peptides, drugs, etc.). Therefore, developing a biocompatible and versatile biomaterial ink design and a novel 4D (bio)printing technique is highly demanding to solve these outstanding biomedical challenges.

Objectives of the research work

Hence, the first part of the research work in the thesis aims to develop a novel class of polysaccharide-based injectable hydrogels engineered to exhibit multifunctional properties such as intrinsic antibacterial and self-healing properties for biomedical applications involving tissue regeneration and sustained delivery. The second part of this research aims to develop novel 4D (bio)printing approaches based on biocompatible and versatile biomaterial inks design-encoded for 4D shape-morphing strategy that can facilitate the development of smart solutions for outstanding biomedical challenges.

Methodology of the research work

Methods

The following chapter describes the protocols and instruments used for the work carried out in this research.

1.1 Methods

1.1.1 Synthesis of quaternized chitosan (QCS)

Quaternized chitosan was synthesized, as reported previously[7, 8]. Briefly, chitosan (1 g) (degree of deacetylation 75%, MW = 270 to 310 kDa) was dispersed in 40 mL DI water. Glycidyl trimethylammonium chloride (GTMAC) (2.77 g) was added, and the mixture was stirred for 15 h at 60°C. The reaction products were precipitated in an ethanol and acetone mixture. Then, the precipitated product was resuspended and dialyzed against ultrapure water for 3 days and lyophilized to obtain the quaternized chitosan (QTS) for further use.

1.1.2 Synthesis of oxidized alginate (Ox-Alg)

The diol group in the backbone of alginate (Alg) was oxidized, as reported previously[4, 9]. Briefly, 100 mL of DI water was used to dissolve 2 g of Alg (molecular weight: 120 to 190 kDa and the ratio of mannuronic acid to guluronic acid (M/G ratio): 1.56). This was followed by the addition of 2.16 g (10 mmol) of sodium periodate, followed by stirring for 6 h at 25 °C in the dark. Next, ethylene glycol (1.5 mL) was added and stirred for another 1 h to terminate the reaction. The reaction solution was dialyzed (MWCO 12000) against ultrapure water with repeated water changes for 3 days. Ox-Alg was obtained following lyophilization.

1.1.3 Determination of the degree of oxidation (DO) of aAlg

DO was calculated by defining the concentration of periodate left by iodometry after the oxidation reaction[6]. Briefly, 4 mL of 20% potassium iodide solution was added to 10 mL aliquot of the reaction mixture. Then 10 mL of 10% sodium bicarbonate solution was added to neutralize it. After that, the reaction was mixed at 25 °C for 30 min in the dark condition. The iodine that was liberated was titrated with standardized 0.01 mol L⁻¹ sodium thiosulphate solution where 1% starch served as the indicator.

1.1.4 Synthesis of nanomaterials

1.1.4.1 Synthesis of CuO nanosheets (CuO)

CuO nanostructures were synthesized by precipitation method using copper nitrate ($\text{Cu}(\text{NO}_3)_2 \cdot 3\text{H}_2\text{O}$) as a precursor material. First, $\text{Cu}(\text{NO}_3)_2 \cdot 3\text{H}_2\text{O}$ was dissolved in 75 mL of deionized water to prepare a 0.5 M solution. Then, NaOH solution (0.2 M) was added dropwise to the solution under vigorous stirring at 50° C until pH reached 8. Subsequently, the solution mixture was heated at 120 °C for 0.5 h, followed by 110 °C for 3.5 h under reflux conditions. After that, nanoparticles were collected with centrifugation at 10⁴ RPM with several washes.

1.1.4.2 Synthesis of ZnO nanoflowers

ZnO nanostructures were synthesized by precipitation method using Zinc nitrate ($\text{Zn}(\text{NO}_3)_2 \cdot 6\text{H}_2\text{O}$). First, the precursor was dissolved in 75 ml of deionized water to form a 0.5 M concentration. NaOH solution (0.2 M) was slowly dropped under vigorous stirring until pH reached to 8 at 50° C. Subsequently, the solution mixture was heated at 120 °C for 4 h, followed under reflux conditions. Thereafter, nanoparticles were collected with centrifugation at 10⁴ rpm with several washes.

1.1.4.3 Surface modification of CuO nanosheets (F-CuO) and ZnO nanoflowers (F-ZnO)

The surfaces of synthesized CuO nanosheets and ZnO nanoflowers were modified with folate ligands by cyclomixing the CuO and ZnO suspension with 0.05 M Na-folate solution (pH 7) for 24 h at room temperature, respectively. Hereafter, ligand-modified CuO is termed F-CuO and ligand-modified ZnO is termed as F-ZnO.

1.1.5 Synthesis of methacrylated derivatives of chitosan (CS-MA), carboxymethyl cellulose (CMC-MA), poly(ethylene glycol) (PEGDMA), alginate (Alg-MA), and κ -carrageenan (κ -CA-MA)

(i) **CMC-MA:** Chemical modification of sodium carboxymethyl cellulose was carried out as described in [10] with minor changes. Briefly, 1 g of CMC was dissolved in 100 mL of deionized (DI) water at a temperature of 60 °C, with continuous stirring to prevent agglomeration. The solution was subsequently cooled to 0 °C, and 4 mL of methacrylic anhydride was slowly added to the CMC solution. The pH of the reaction mixture was maintained at 8.0 by the periodic addition of 3 M sodium hydroxide (NaOH) solution. The reaction was allowed to continue for a period of 24 hours under constant stirring within an ice bath. The methacrylated CMC (CMC-MA) solution was then transferred to a dialysis membrane with a molecular weight cutoff of 12 to 14 kDa and dialyzed against DI water at room temperature for a period of 3 days. The resultant solution was frozen at –80 °C and subsequently lyophilized for a duration of 3 days. The lyophilized CMC-MA foam was stored at –80 °C until further use.

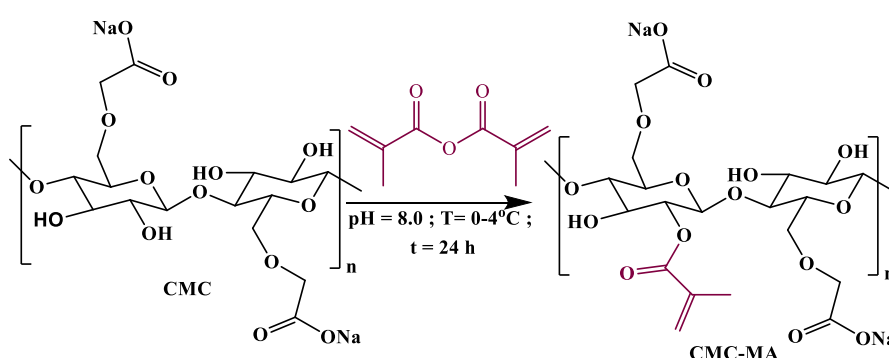


Figure 1- 1: Schematic representation of methacrylate modification of carboxymethyl cellulose (CMC).

(ii) **CS-MA:** Methacrylation of chitosan was performed according to the procedure laid down in [11] following suitable modifications. Briefly, 1 g of chitosan was dissolved in 100 ml of 0.4 M acetic acid solution at 50 °C with constant stirring for 24 hours. Subsequently, 5 mL of glycidyl methacrylate (GMA) was gradually added to the chitosan solution, and the reaction was allowed to continue under constant stirring at 50 °C for a period of 24 hours. The methacrylated chitosan (CS-MA) solution was then transferred to a dialysis membrane with a molecular weight cutoff of 12 to 14 kDa and dialyzed against deionized (DI) water at room temperature for a period of 3 days. The solution was then frozen at –80 °C and subsequently lyophilized for a duration of 3 days. The lyophilized CS-MA foam was stored at –80 °C until further use.

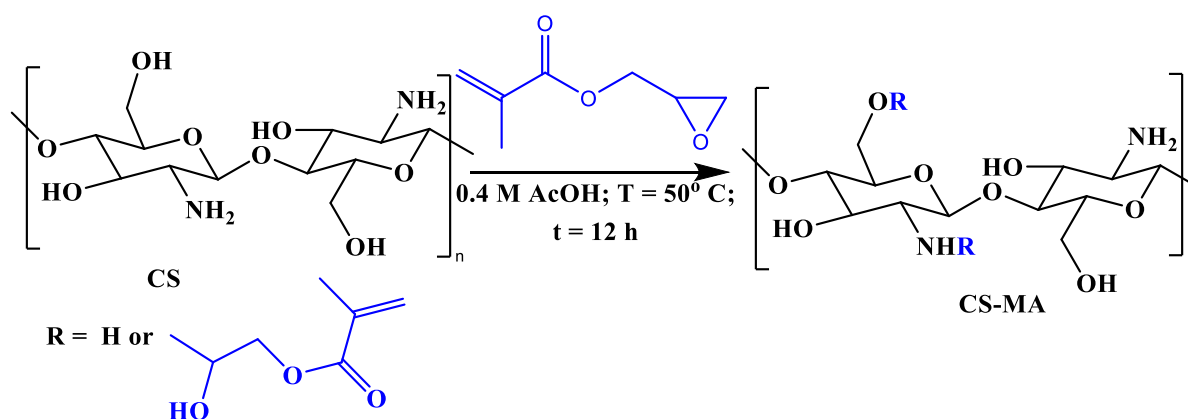


Figure 1- 1: Schematic representation of methacrylate modification of chitosan (CS).

(iii) **PEGDMA:** The synthesis of poly(ethylene glycol) dimethacrylate (PEGDMA) was conducted in accordance with the procedure described in [12]. In brief, poly(ethylene glycol) was mixed with a 10-fold excess of methacrylic anhydride in a scintillation vial and subjected to microwave irradiation at a maximum power of 900 W for a duration of 7 minutes, with a 1-

minute interval after each minute of irradiation, during which the vials were vortexed. Subsequently, the reaction mixture was cooled to room temperature and solubilized in dichloromethane. Unreacted methacrylic anhydride was then eliminated by precipitating PEGDMA in excess of diethyl ether, and the process was repeated thrice. Following precipitation, the resulting product was filtered and subjected to overnight drying in a vacuum oven.

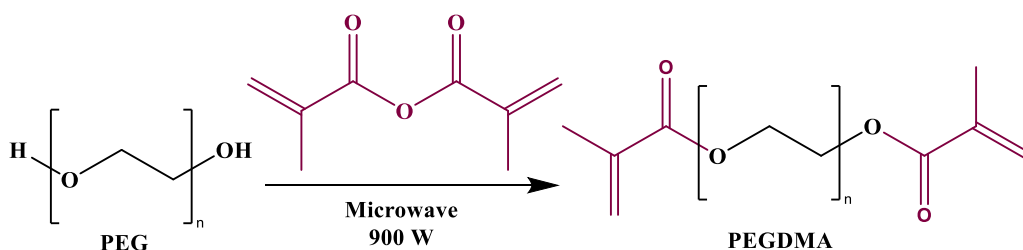


Figure 1- 2: Schematic representation of methacrylate modification of poly(ethylene glycol) (PEG).

(iv) Alg-MA: Chemical modification of sodium alginate (Alg) was carried out as described in [13] with minor changes. Briefly, 2 g of Alg was dissolved in 100 mL of deionized (DI) water at a temperature of 60 °C, with continuous stirring to prevent agglomeration. The solution was subsequently cooled to 0 °C, and 10 mL of methacrylic anhydride was slowly added to the Alg solution. The pH of the reaction mixture was maintained at 8.0 by the periodic addition of 3 M sodium hydroxide (NaOH) solution. The reaction was allowed to continue for a period of 24 hours under constant stirring within an ice bath. The methacrylated Alg (Alg-MA) solution was then transferred to a dialysis membrane with a molecular weight cutoff of 12 to 14 kDa and dialyzed against DI water at room temperature for a period of 3 days. The resultant solution was frozen at −80 °C and subsequently lyophilized for a duration of 3 days. The lyophilized CMC-MA foam was stored at −80 °C until further use.

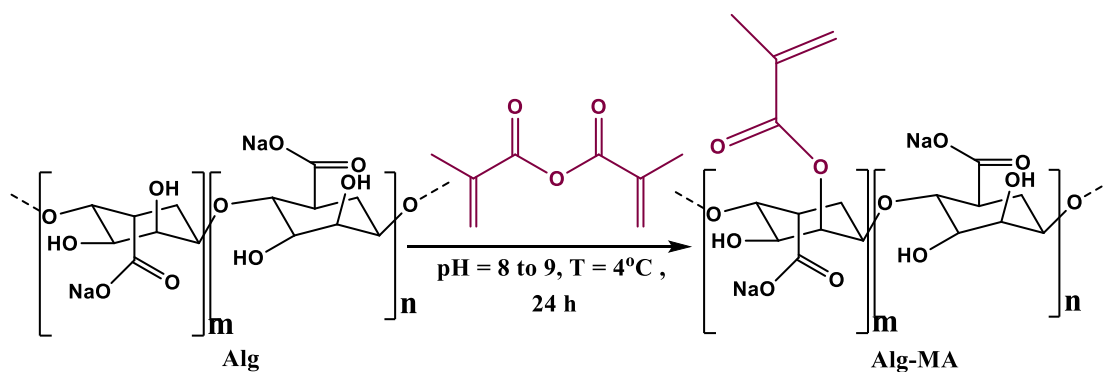


Figure 1- 3: Schematic representation of methacrylate modification of sodium alginate (Alg).

(v) **κ -CA-MA:** κ -carrageenan (κ -CA) was modified following the procedure laid down in [14]. Briefly, 1 g of κ -CA was dissolved in 100 mL of deionized (DI) water at a temperature of 60 °C, with continuous stirring to prevent agglomeration. Subsequently, 12 mL of methacrylic anhydride was slowly added to the κ -CA solution, and the pH of the reaction mixture was adjusted to 8.0 with 5 M sodium hydroxide (NaOH) solution. The reaction was allowed to continue for a period of 12 hours under constant stirring at 60 °C. The methacrylated κ -CA (κ -CA -MA) solution was then transferred to a dialysis membrane with a molecular weight cutoff of 12 to 14 kDa and dialyzed against DI water at room temperature for a period of 3 days. The resultant solution was frozen at -80 °C and subsequently lyophilized for a duration of 3 days. The lyophilized CMC-MA foam was stored at -80 °C until further use.

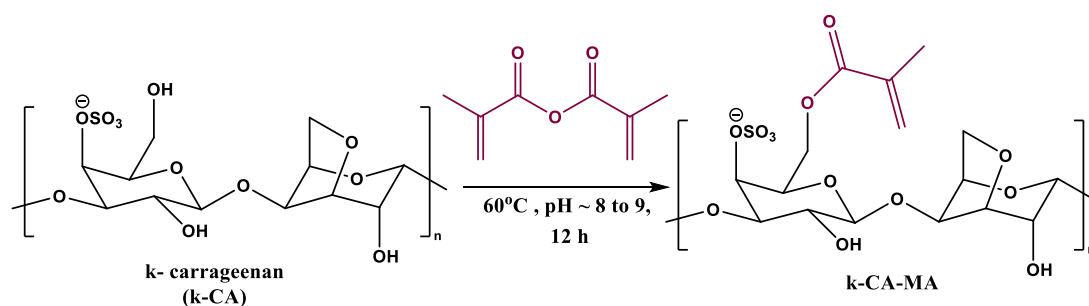


Figure 1- 4: Schematic representation of methacrylate modification of κ -carrageenan (κ -CA).

1.1.6 Synthesis of Pluronic F127 dimethacrylate (PF127DMA)

The synthesis of Pluronic F127 dimethacrylate (PF127DMA) was conducted similarly to the synthesis of PEGDMA. In brief, Pluronic F127 was mixed with a 10-fold excess of methacrylic anhydride in a scintillation vial and exposed to microwave irradiation at a maximum power of 900 W for 7 minutes, with a 1-minute interval after each minute of irradiation while mixing the contents of the vial using a vortex mixer. Subsequently, the reaction mixture was cooled to room temperature and solubilized in dichloromethane. Excess methacrylic anhydride was removed by precipitating PF127MA in cold diethyl ether, repeating the process thrice. After precipitation, the resulting product was filtered and subjected to overnight drying in a vacuum oven.

1.1.7 3D printing

1.1.7.1 Extrusion based 3D printing

For Chapter 5, the 3D models were designed in SolidWorks (Dassault Systems) and sliced using Slic3r software to generate the G-codes used in this work. The G-codes were subsequently imported into the Bio-X 3D bioprinter (CELLINK, Sweden) for the fabrication of the hydrogel constructs. The precursor solutions loaded in the cartridges were extruded through a 25-gauge nozzle and deposited onto a Teflon surface, with the printing parameters specified in Table 2- 1. Following the printing process, the constructs were photocrosslinked using the in-built 405 nm blue light in the bioprinter. The details of the ink compositions are described in their respective chapters.

Table 1- 1: Printing parameters

Ink	Pressure	Printing speed
CMC-MA/MC	150 ± 30 kPa	9 ± 3 mm/s

CS-MA/PEGDMA/MC	140 ± 30 kPa	13 ± 3 mm/s
Alg-MA/MC	200 ± 20 kPa	10 ± 2 mm/s
κ-CA-MA/MC	180 ± 20 kPa	$1. \pm 2$ mm/s

1.1.7.2 Light-assisted 3D printing (DLP)

For Chapter 6, all three-dimensional (3D) models were developed using SolidWorks (Dassault Systems) or Microsoft 3D Builder software and subsequently converted into STL files for transfer to the LumenX printer (CELLINK). Slicing of the models was performed using the built-in software, with a layer thickness of 100 μ m along the z-axis for each structure. A polydimethylsiloxane (PDMS) plate served as the substrate for the photocurable ink. Following the preparation of the build plate, printing parameters were set with an exposure time of 10 seconds at 65% power (22 mW/cm²) for each layer. The initial layers of each structure were crosslinked with an exposure time four times longer than that of the subsequent layers. Upon completion of printing, the structures were removed from the build plate and characterized. The details of the ink compositions are described in their respective chapters.

1.1.8 Chemical and physical characterization

1.1.8.1 Fourier transform infrared (FTIR) spectroscopy

Synthesized prepolymer, and the hydrogels were characterized, after freeze-drying, by Fourier transform infrared (FTIR) spectroscopy (Perkin-Elmer Frontier IR/NIR systems, USA) in attenuated total reflection (ATR) mode. All spectra were measured from 650 to 4000 cm⁻¹ with 4 cm⁻¹ resolution and 32 consecutive scans.

1.1.8.2 Nuclear magnetic resonance (NMR) spectroscopy

¹H nuclear magnetic resonance (¹H NMR) (AV400, Bruker) was conducted at 400 MHz to validate the successful synthesis or modification of all prepolymer using D₂O as the solvent.

The baseline was adjusted using Mnova-Mestrelab before the integration of the peak of interest. The degree of substitution (DS) was determined through ¹H NMR spectroscopy.

1.1.8.3 Scanning electron microscopy (SEM)

Cross-sectional surfaces of hydrogels were imaged using a scanning electron microscope (Ultra55 FE-SEM, Carl Zeiss). For SEM imaging, the hydrogels were freeze-dried by dipping them first in liquid nitrogen and then stored at -80°C before lyophilizing for 24 h. Thereafter, the samples were cryo-sectioned and coated with gold by sputtering before imaging. The pore size was quantified with the ImageJ software by analyzing the SEM images for > 25 randomly selected pores for each gel composition.

1.1.8.4 Swelling ratio

The swelling behavior was characterized by immersing the hydrogels in PBS (pH 7.4) at 37°C. The sample weight was assessed at predetermined intervals until it became constant. Triplicates of each hydrogel were measured. The swelling ratio was calculated using the following equation:

$$\text{Swelling ratio (\%)} = \frac{W_t - W_i}{W_i} \times 100$$

Where W_i and W_t are the initial weight of the hydrogels and the weight of the hydrogel at individual time points, respectively.

1.1.8.5 Degradation behavior

The degradation behavior of the hydrogels was investigated based on their weight loss. Briefly, hydrogels were lyophilized, and the weight was measured at the initial time (W_i). The gels were incubated in 10 mL PBS (pH 7.4) or high glucose Dulbecco's modified Eagle's medium (DMEM) supplemented with 10% (v/v) heat-inactivated FBS (complete culture medium, CCM) at physiological temperature (37 °C). To measure the mass loss, the hydrogel was

removed from the solution at predetermined time intervals, lyophilized, and the weight was measured in the dry state (W_i). The degradation rate was calculated by the following equation:

$$\text{Remaining weight (\%)} = \left(\frac{W_t}{W_i} \right) \times 100$$

1.1.8.6 Water retention

The moisture retention time was assessed by measuring the water loss over time. The hydrogel discs were allowed to swell to saturation in PBS and measured weight (W_i). The saturated hydrogels were kept in an incubator at 37 °C and measured weight at predetermined intervals (W_t) until a constant value was obtained. The experiment was performed without sealing the samples. The percentage of moisture retained was calculated by the following equation.

$$\text{Water retention} = \left(\frac{W_t}{W_i} \times 100 \right)$$

To quantify the water retention performance of hydrogels, the printed hydrogel discs were placed in an oven at 45°C, and the weights were recorded every 30 min. The water retention rate is calculated using the same equation.

1.1.8.7 Mechanical properties of hydrogels

A universal testing machine (Multitest – 10i, Mechmesin) was used to perform the compression tests on the hydrogels (8 mm diameter × 6 mm height). 25 N load cell and 2 mm/min displacement rate was used for all the measurements. Displacement was continued until a sudden drop in the stress-strain curve, and this drop point was considered as the fracture strength. The compressive modulus was evaluated by considering the slope in the linear portion of the stress–strain curve in the 5 to 20% strain.

Dog-bone structures (15 mm gage length, 4 mm width, 2 mm thickness) were 3D printed to evaluate the mechanical behavior of the printed conducting hydrogel constructs. All tensile and

cyclic loading-unloading measurements were conducted using a 25 N load cell and a displacement rate of 10 mm/min. The engineering stresses (σ) and strain (γ) were calculated using the following equation.

$$\sigma = \frac{F}{A_0}$$

$$\% \gamma = \left(\frac{\Delta l}{l} \right) \times 100$$

F is the applied force, and A0 is the initial cross-sectional area. l is the gauge length of the dog bone printed hydrogel. Toughness was calculated by evaluating the area under the stress-strain curve, and %Elongation was measured as per the following equation.

$$\% \text{Elongation} = (\% \gamma \text{ at fracture point} - 100)$$

The hysteresis test was performed under various % strain from 20% to 100% at a constant stretching rate of 10 mm/min and immediately unloaded at the same strain speed. Then, the successive loading-unloading test was conducted for 20 cycles at 50% strain. The dissipated energy was defined as the area in the hysteresis loop encompassing the loading-unloading profile. Sample dimensions were detailed in the corresponding chapter.

1.1.8.8 Self-healing ability

The self-healing performance of hydrogels was evaluated with qualitative self-healing tests and macroscopic self-healing experiments. Methylene blue was used to stain one hydrogel disc, while rhodamine B was used for the other one. Both stained hydrogels were cut into two pieces using a surgical blade. Then, two hydrogel pieces of opposite colors were placed adjacent next to one another at 37°C for 3 h, and healing was assessed from microscopic images. Afterward, the healed discs were immersed in PBS (at pH 7.4) for 24 h to verify stability post-healing.

1.1.8.9 Rheological behavior of hydrogels

The rheological behavior of the hydrogels was studied using the cone and plate geometry using rheometer (DHR-3 model, TA Instruments). Several experiments were carried out as follows. Several tests were performed as follows.

(i) The amplitude sweep from 1 to 800 % strain at a constant angular frequency of 10 rad s⁻¹ was initially conducted to find the linear viscoelastic region (LVR) where the storage modulus (G') is not dependent on the strain amplitude.

(ii) The hydrogel was tested at 25 °C at a fixed angular frequency of 10 rad/s. The dynamic strain was swept from 1 to 800 % to identify gel to sol transition point. From this experiment, 1% strain was chosen for the oscillation test to perform in the LVR.

Loss modulus (G'') and storage modulus (G') of the hydrogel were assessed as functions of angular frequency (ω) in the range of 0.01 to 100 rad s⁻¹ at a fixed strain of 1 % at 25° C. The damping factor ($\tan\delta = G''/G'$) was calculated and plotted as a function of angular frequency.

(iii) The alternate step strain sweep of the hydrogel was assessed at a fixed angular frequency (10 rad s⁻¹). In this case, strains were switched from a small strain ($\gamma = 5.0\%$) to a large strain ($\gamma = 500\%$) with 150 s holding time for each strain interval.

(iv) A flow sweep of the hydrogel was conducted by changing the shear rate from 0.01 to 100 s⁻¹ at 25 °C.

(iv) A three interval-time-thixotropy (3ITT) recovery test of the hydrogel was conducted under three shearing intervals (low shear rate 1 s⁻¹ for 60 s to higher shear rate 100⁻¹ for 60 s and again at the lower shear rate) as a function of time.

(v) The thixotropic loop was measured with an increasing shear rate from 0.01 to 100 s⁻¹ in the up step and similarly decreasing back to 0.01 s⁻¹ shear rate in the down step at 25 °C.

(vi) To test the temperature stability of the hydrogel, G' and G'' were measured by heating steadily at $5^{\circ}\text{C} / \text{min}$ from 25°C to 60°C at a fixed angular frequency of 10 rad s^{-1} and fixed strain of 1%.

1.1.9 *In vitro* cytocompatibility of hydrogels

NIH/3T3 mouse fibroblasts and MDA-MB-231 human breast cancer epithelial cells, SVEC4-10 endothelial cells, and L929 mouse fibroblast cells were cultured in high glucose DMEM (HG-DMEM) containing 10% (v/v) FBS. HaCaT human keratinocyte cells were cultured in 10% (v/v) FBS containing low glucose DMEM (LG-DMEM) media. Antibiotic Penicillin–Streptomycin (Sigma) was added at 1% (v/v). Cells were passaged with trypsin–EDTA (Sigma). The cytocompatibility of the hydrogels was assessed with the Alamar blue assay and Live-dead stain. The cells were seeded into 48 well plates at 4×10^3 cells / well containing the complete culture medium and incubated for 24 h at 37°C with 5% CO_2 . To prepare the conditioned medium, the freshly prepared hydrogel in the complete culture medium at 100 mg /mL was allowed to degrade for 24 h in the cell culture incubator. Cells in the fresh medium were used as the control.

The methodology details of the cytocompatibility study for the hydrogels of chapters 5 and 6 are described in their respective chapters.

1.1.9.1 Alamar blue assay

Cell viability was evaluated via Alamar blue assay on days 1 and 3. Treated cells were incubated for 3 h in the culture medium containing 0.0015mg/mL dye. The fluorescence intensity was measured at 530/590 nm with a spectrophotometer (Biotek). All measurements were performed in triplicates.

$$\% \text{ of cell viability} = \frac{\text{Fluorescence intensity of the sample}}{\text{Fluorescence intensity of the control}} \times 100$$

1.1.9.2 Live-dead assay (LDA)

LDA was executed to qualitatively assess cell viability after exposure to the conditioned medium. The cells were cultured in the conditioned medium, as above. On days 1 and 3, the cells were incubated with Calcein-AM and ethidium homodimer-1 (live-dead cell staining kit) and followed the guidelines from the manufacturer. The samples were imaged using an epi-fluorescence microscope (IX-53, Olympus).

1.1.9.3 F-actin and nucleus staining

To characterize the F-actin arrangement, the cells were first fixed for 15 min with 3.7% formaldehyde. After that, Cells were treated for 10 min with 0.1% Triton X-100 to permeabilize the cell membrane. Then, cells were stained with 10 µg/mL fluorescein isothiocyanate (FITC)-conjugated phalloidin dye for 25 min and followed by 1 µg/mL of 4,6-diamidino-2-phenylindole (DAPI) dye for 5 min. The stained cells were imaged using an epi-fluorescence microscope.

1.1.10 Bacteria culture

The Gram-negative *Pseudomonas aeruginosa* (ATCC 27853) and *E. coli* (ATCC 25922) and Gram-positive *Staphylococcus aureus* (ATCC 25923) were chosen as model pathogens, representative of differences in cell wall structure of bacteria. Both strains are opportunistic human pathogens capable of causing a wide array of life-threatening acute and chronic infections, particularly in patients with compromised immune system[15, 16].

1.1.11 Bacteria strains and growth conditions

The bacterial stock solutions were prepared in 20% glycerol nutrient broth and stored at –80 °C until use. Stock suspensions were revived on nutrient agar at 37 °C for 24 h and sub-cultured on fresh nutrient agar plates prior to use. Then, bacterial cell suspensions were prepared by suspending a single bacterial colony in 10 mL nutrient broth and incubating overnight. Prior to

experiments, a secondary culture was prepared using bacteria from the primary culture at a 1:50 ratio. The cells were collected in the logarithmic stage of growth, and absorbance at 600 (OD₆₀₀) was adjusted for further experiments (details are available in the corresponding chapter).

1.1.12 Statistics

All quantitative measurements were performed in triplicates as mean \pm standard deviation. Each experiment was performed at least thrice. Statistical differences were analyzed using 2-way ANOVA with Sidak's and one-way ANOVA with Tukey's, post-test wherever applicable. **** indicates $p < 0.0001$, *** indicates $p < 0.001$, ** indicates $p < 0.01$, * indicates $p < 0.05$ and ns indicates statistically non-significant.

1.2 Reference:

1. Jiang, H., et al., *Biodegradable hyaluronic acid/N-carboxyethyl chitosan/protein ternary complexes as implantable carriers for controlled protein release*. Macromolecular bioscience, 2005. **5**(12): p. 1226-1233.
2. Sashiwa, H., et al., *Chemical modification of chitosan*, 17. Macromolecular Bioscience, 2003. **3**(5): p. 231-233.
3. Sashiwa, H., et al., *Michael reaction of chitosan with various acryl reagents in water*. Biomacromolecules, 2003. **4**(5): p. 1250-1254.
4. Blemur, L., et al., *Carboxymethyl starch/alginate microspheres containing diamine oxidase for intestinal targeting*. Biotechnology Applied Biochemistry, 2016. **63**(3): p. 344-353.
5. Wei, Z., et al., *Novel biocompatible polysaccharide-based self-healing hydrogel*. Advanced Functional Materials, 2015. **25**(9): p. 1352-1359.
6. Balakrishnan, B. and A. Jayakrishnan, *Self-cross-linking biopolymers as injectable in situ forming biodegradable scaffolds*. Biomaterials, 2005. **26**(18): p. 3941-3951.
7. Qu, J., et al., *Antibacterial adhesive injectable hydrogels with rapid self-healing, extensibility and compressibility as wound dressing for joints skin wound healing*. Biomaterials, 2018. **183**: p. 185-199.
8. Qin, C., et al., *Calorimetric studies of the action of chitosan-N-2-hydroxypropyl trimethyl ammonium chloride on the growth of microorganisms*. International journal of biological macromolecules, 2004. **34**(1-2): p. 121-126.
9. Mondal, P. and K. Chatterjee, *Injectable and self-healing double network polysaccharide hydrogel as a minimally-invasive delivery platform*. Carbohydrate Polymers, 2022. **291**: p. 119585.
10. Melilli, G., et al., *DLP 3D printing meets lignocellulosic biopolymers: Carboxymethyl cellulose inks for 3D biocompatible hydrogels*. Polymers, 2020. **12**(8): p. 1655.
11. Flores-Ramírez, N., et al., *Characterization and degradation of functionalized chitosan with glycidyl methacrylate*. Journal of Biomaterials Science, Polymer Edition, 2005. **16**(4): p. 473-488.
12. Lin-Gibson, S., et al., *Synthesis and characterization of PEG dimethacrylates and their hydrogels*. Biomacromolecules, 2004. **5**(4): p. 1280-1287.
13. Mignon, A., et al., *Characterization of methacrylated alginate and acrylic monomers as versatile SAPs*. Carbohydrate polymers, 2017. **168**: p. 44-51.
14. Kumari, S., P. Mondal, and K. Chatterjee, *Digital light processing-based 3D bioprinting of κ -carrageenan hydrogels for engineering cell-loaded tissue scaffolds*. Carbohydrate Polymers, 2022. **290**: p. 119508.

15. Cerioli, M., et al., *Pseudomonas aeruginosa* implant-associated bone and joint infections: experience in a regional reference center in France. *Frontiers in Medicine*, 2020. **7**: p. 513242.
16. De Bentzmann, S. and P. Plésiat, *The Pseudomonas aeruginosa opportunistic pathogen and human infections*. *Environmental microbiology*, 2011. **13**(7): p. 1655-1665.

Research 1

**Multi-biofunctional Self-healing Adhesive Injectable Nanocomposite
Polysaccharide Hydrogel**

2.1 Introduction

Injectable hydrogels offer many advantages over conventional hydrogels for numerous applications as discussed in Chapter 1. Injectable hydrogels can rapidly take the shape of any irregular cavities when dispensed via a minimally invasive delivery module[1, 2]. They can be placed precisely in specific and deep locations via syringe/catheter without complex surgeries. A widely adopted approach to engineer an injectable hydrogel is designing precursor prepolymer solutions that can undergo rapid chemical crosslinking to yield gels such that various therapeutic agents (drugs, proteins, cells, nanoparticles, etc.) can be homogeneously mixed into the precursor polymer solution in a potentially cargo-protective manner before administration[3, 4]. However, sol-to-gel transition time is a critical parameter for clinical administration because rapid crosslinking may lead to syringe/catheter obstruction before the hydrogel is dispensed. In contrast, a delayed crosslinking process may result in material dissipation upon injection and the undesired release of unreacted precursors out of the target zone, leading to off-site cytotoxicity[3, 4]. To overcome these challenges, the innovation of new hydrogels that can flow upon introducing shear stress (i.e., shear-thinning) and reform after stress removal (i.e., self-healing) has grown in popularity[5]. Apart from this, the placed hydrogels would continuously sustain external force in daily life once concerned for tissue engineering, which usually causes the traditional hydrogels to break, followed by function loss as discussed in chapter 1.

Furthermore, the damage to the hydrogel can also be accessible as a gateway for microbial invasion, resulting in a high chance of infection. In these circumstances, a self-healing hydrogel exhibiting antibacterial properties would be highly beneficial to inhibit bacterial infection at the wound site. However, a multi-functionalized injectable hydrogel that synchronously performs on self-healing ability, and on-demand antibiosis still has not been realized, which would have extensive potential in numerous bioengineering applications.

Recent research has concentrated on developing additional materials systems originating from natural polymer to form injectable self-healing hydrogel via dynamic Schiff base reaction as a delivery platform in a minimally invasive manner. Chitosan and alginate are abundant polysaccharides, which are biocompatible and biodegradable polymers. As a polycation at acidic media ($\text{pH} < 6$), chitosan interacts with negatively charged molecules, such as anionic polysaccharides, phospholipids, fatty acids, and proteins[6]. Moreover, chitosan can control inflammatory mediators, regenerate the wound via fibroblast proliferation, and improve hyaluronic acid synthesis to accelerate the healing process with minimal scarring[7, 8]. Chitosan promotes revascularization and protects against atherosclerosis[7]. On the other hand, alginate can impart the desired rheological properties[9, 10] to the crosslinked hydrogel system for injectability along with its water-retaining capacity[11] and the ability to carry pro-inflammatory signals for accelerated healing of chronic wounds[12]. Although various formulations of injectable hydrogels have been reported in the literature, few achieved multi-biofunctionality. In a previous study, we reported a polysaccharide-based injectable self-healing hydrogel system prepared from modified chitosan and alginate as a minimally-invasive delivery platform but was limited by the lack of bioactivity to augment wound healing[13].

The incorporation of a nanofiller in an injectable hydrogel network is a potential strategy to endow bioactivity. However, it is essential to design and tailor the nanocomposite formulation to maintain injectability, rapid self-healing, controlled degradability, and cytocompatibility while imparting key bioactive attributes such as antibacterial activity and ability to scavenge reactive oxygen species. Among various nanoparticles, metallic copper/ copper oxide nanoparticles provide many benefits. Copper is an essential element that aids multiple enzymes and supports wound healing, angiogenesis, and skin regeneration[14, 15]. Higher dosage of copper is reported to be toxic[16, 17]. However, the chemical reduction method for nanoparticle synthesis and their modification with bioligands can improve cytocompatibility while

imparting substantial bacteriostatic/bactericidal properties[18, 19]. Thus, copper oxide nanomaterial surfaces modified with folic acid could endow multi-biofunctional properties to a self-healing injectable hydrogel.

We hypothesized that a reaction of quaternized chitosan (QTS) with oxidized alginate (Ox-Alg) in the presence of adipic acid dihydrazide (ADH) and folic acid- functionalized CuO (F-CuO) nanosheets will yield a polysaccharide-based injectable, shear-thinning hydrogel with self-healing and antibacterial ability. In this study, different formulations were systematically characterized to obtain the best combination for gelling, injectability, self-healing behavior, cytocompatibility, ROS scavenging ability, and antibacterial activity. This work aimed to establish this nanocomposite hydrogel as a promising candidate material for various biological and medical applications.

2.1 Methods

2.1.1 Synthesis of CuO nanosheets (CuO) and surface modification of CuO nanosheets (F-CuO) and characterization of nanomaterials

CuO nanosheets were synthesized using the precipitation method as described in section 1.1.4.1 of methodology section. Then, the surfaces of synthesized CuO nanosheets were modified with folate ligands as described in section 1.1.4.3 of methodology section. Then, the CuO nanosheets were visualized in an SEM (Ultra55 FE-SEM, Carl Zeiss Mono) and TEM (Tenai G2 ST200 TEM). The synthesized CuO and F-CuO were analyzed through powder X-ray diffraction (XRD, D8 Advance, Bruker, Germany, using a Cu K α source ($\lambda = 0.15406$ nm)). The patterns were recorded in the 2θ range of 5 to 80° at room temperature. Raman spectra (Raman Spectrometer, WITEC) of CuO and F-CuO were recorded at room temperature using a 514 nm excitation source. UV spectra of CuO and F-CuO were recorded using Perkin Elmer LAMBDA 950 UV-VIS-NIR Spectrophotometer. Similarly, ZnO nanoflowers was synthesized

and surface modified with folic acid as described in sections 1.1.4.2 and characterized as mentioned above.

2.1.2 Hydrogel preparation

QCS and Ox-Alg were synthesized as described in sections 1.1.1 and 1.1.2 of methodology section. The basic formulation of the prepolymer concentration to prepare the hydrogel was chosen according to our developed protocol with some modifications. In detail, Ox-Alg solution at 0.2 g/mL concentration in 0.01 M phosphate-buffered saline (PBS) was mixed with the solution of QCS solution (0.03 g/mL), $0.7 \mu\text{molL}^{-1}$ ADH, and 0.1 mg/mL F-CuO in PBS to prepare nanomaterials linked network hydrogel (hereafter designated as F-CuO/Ox-Alg/QCS NH). Hydrogels without F-CuO were also prepared for comparison by mixing Ox-Alg solution with QCS and ADH solution (hereafter designated as Ox-Alg/QCS NH). Initially, hydrogels without F-CuO were formulated at several weight ratios ($R = W_{\text{tQCS}} : W_{\text{tOx-Alg}}$) of 0.05, 0.10, 0.25, 0.50, 0.80, and 1.00 to identify the optimized gelation time. The vortex mixer was used to mix the solution for homogenous mixing to form the hydrogel. The gelation time was determined using the vial inversion method. Every gelling time was evaluated in three separate runs.

2.1.3 Characterization of prepolymer and hydrogels

Chemical characterizations of QCS, Ox-Alg, and hydrogel were done by FTIR and ^1H NMR spectroscopy as described in sections 1.1.8.1 and 1.1.8.2. SEM micrographs were captured as described in section 1.1.8.3. Additional properties relevant to biomedical applications, such as swelling behavior, degradation studies, and water retention were also performed as described in sections 1.1.8.4, 1.1.8.5, and 1.1.8.6 respectively, of Methodology section. Self-healing ability, and rheological properties were evaluated as described in sections 1.1.8.8, and 1.1.8.9, respectively, of methodology section.

2.1.4 Adhesion test of hydrogel

Chicken organs were collected from a local butcher shop. Organs were cut into two pieces, and F-CuO/Ox-Alg/QCS NH was placed in between them to evaluate the ability to adhere to different organs, such as the heart, skin, liver, and spleen. All organs were first immersed in PBS (pH = 7.4), and then the organs were removed from the PBS solution and used directly without drying to simulate the moist environment of in vivo injury.

Lap-shear tests were used to evaluate the lap-shear strength. A universal testing machine (Multitest – 10i, Mechmesin) equipped with a 25 N load cell was used to measure the lap-shear strength. Tests were conducted at a constant displacement rate of 2 mm min⁻¹. For the lap-shear test, F-CuO/Ox-Alg/QCS NH was placed into the adhesion region of the two cut pieces of the chicken skin, and the adhesion area was fixed to 15 mm width × 7 mm length. The lap-shear strength was calculated according to the following equation.

$$Lap - shear\ strength = \frac{F_l}{w_h \times l_h}$$

Where F_l is the maximum force during shearing, and w_h and l_h are the width and length of the applied hydrogel area, respectively.

2.1.5 In vitro cytocompatibility of CuO, F-CuO and hydrogels

HaCaT human keratinocyte cells, L929 fibroblast cells and SVEC4-10 endothelial cells were used in this study and cultured as discussed in section 1.1.9. The cytocompatibility of the CuO and F-CuO nanosheet were evaluated with the MTT assay using L929 and HaCaT cells and HaCat cells was used to evaluate the cytocompatibility of the hydrogels. To evaluate the cytocompatibility of the Ox-Alg/QCS NH and F-CuO/Ox-Alg/QCS NH, alamar blue assay, Live dead assay (LDA), and F-actin and Nucleus staining assay were performed as described in sections 1.1.9.1, 1.1.19.2 and 1.1.9.3 respectively, of the methodology section.

2.1.6 Hemolytic activity

Goat blood was collected from a local butcher shop. Red blood cells (RBCs) were separated from the blood by centrifugation at 7000 rpm for 10 min at 25 °C. RBCs were diluted 5 times with PBS (pH = 7.4). The dispersion of RBCs was treated with the hydrogel samples (50 mg or 100 mg as prepared hydrogel per mL) for 2 h at 37°C where the dispersion of RBCs treated with PBS was selected as a negative control and treated with Triton-100 was used as a positive control. After 2 h, the RBC dispersion was centrifuged at 5000 rpm for 10 min, and the supernatant was collected. The absorbance of the supernatant was measured at 540 nm using a microplate reader (Biotek). Measurements were performed in triplicates. The percentage hemolysis was calculated by following the equation.

$$\text{Hemolysis (\%)} = \left(\frac{\text{Absorbance of sample} - \text{Absorbance of negative control}}{\text{Absorbance of positive control} - \text{Absorbance of negative control}} \right) \times 100$$

2.1.7 Antioxidant efficiency of hydrogels and cellular protection against ROS

The antioxidant efficiency of hydrogels was assessed by quantifying their capacity to scavenge the stable 1,1-diphenyl-2-picrylhydrazyl (DPPH) free radical. The hydrogels were cut into homogenate. Next, 100 µM DPPH and hydrogel samples (50 mg or 100 mg per mL) were dispersed in methanol, stirred, and incubated in the dark for 45 min. Then, the absorbance at 517 nm was measured using a microplate reader (Biotek). DPPH scavenging efficiency was calculated using the following equation.

$$\text{DPPH scavenging (\%)} = \left(\frac{A_C - A_H}{A_C} \right) \times 100$$

Where A_C is the absorbance of the control (DPPH + methanol), and A_H is the absorbance of the hydrogel samples (DPPH + methanol + hydrogel).

To evaluate the cellular protection against ROS, 5×10^3 L929 cells were seeded into 48 well plates and incubated with complete culture medium for 1 day with 5% CO₂ at 37°C. After that,

cells were treated with condition media for 1 day. After 24 h incubation, cells were treated with 500 μM of H_2O_2 for 45 min to induce ROS in seeded cells in the presence of the additional hydrogel scaffold in each well (10 mg/ mL). Subsequently, cells were incubated for 12 h. Cells treated with the complete fresh culture medium and not treated with H_2O_2 served as a positive control. Cells treated with the complete fresh culture medium and then treated with H_2O_2 served as a negative control. The MTT assay was performed at 0 and 12 h after induction of ROS. The absorbance was measured at 570 nm with a spectrophotometer (Biotek).

2.1.8 *In vitro* scratch-assay test

SVEC mouse endothelial cells were seeded in 24-well plates (75×10^3 cells per well) and cultured to 90% confluency. After starvation with an FBS-free medium for 8 h, the cell layer was scratched in a straight line using a 200 μL pipette tip to mimic an incisional wound. Cells were washed with PBS to remove debris and incubated at 37 $^\circ\text{C}$ in conditioned medium of F-CuO/Ox-Alg/QCS NH (100 mg /mL of medium containing degradation products of 24 h degradation), containing 2.5 % FBS. Cells in the corresponding fresh medium with 2.5% FBS were used as the control. The cell layer was observed and imaged at 0, 8, 12, 16, and 20 h using phase contrast microscopy (IX-53, Olympus). The cell migration rate was calculated using the following equation.

$$\text{Cell migration (\%)} = \left(\frac{A_0 - A_t}{A_0} \right) \times 100$$

Where A_0 is the scratch area at 0 h, and A_t is the scratch area without cell coverage at a given time.

2.1.9 Antibacterial activity

Gram-positive *S. aureus* and Gram-negative *E. coli* were used in this study and cultured as described in section 1.1.10 to evaluate the antibacterial activity of hydrogels. F-CuO/Ox-Alg/QCS NH (100 mg/mL) and Ox-Alg/QCS NH (100mg/mL) were utilized as experimental

groups. The control group was cultured with fresh medium without samples. The bacterial suspensions in nutrient broth (100 µl of 0.2 OD₆₀₀) were treated with the hydrogel (100 mg/mL) and incubated at 37°C for 5 h. At the end of that time, 1 mL of sterilized PBS was added to each well to resuspend the bacterial cells. After 12-20 h incubation at 37 °C, the colony-forming units (CFU) on the agar plate were counted. Tests were repeated three times for each group. The log reduction was calculated with the following equation.

$$\text{log reduction} = \log\left(\frac{\text{CFU/mL of control}}{\text{CFU /mL of sample}}\right)$$

2.1.10 Statistics

Each measurement was performed in triplicates and presented as mean ± standard deviation. Statistical differences were analyzed as described in section 1.1.12.

2.2 Results and discussion

2.2.1 Preparation and characterization of F-CuO nanosheets

The shape of engineered nanomaterials can influence the physicochemical properties. Literature suggests that CuO nanosheets have higher surface reactivity, electrochemical behavior, and antimicrobial activity compared to CuO nanospheres[20]. Here, we have synthesized CuO nanosheets by the simplified precipitation method and the yield is 93 to 97%. The morphology of the synthesized CuO products was revealed with FESEM, as presented in Figure 2- 1a. The FESEM image reveals that the obtained nanomaterial exhibits sheet-like morphology (Figure 2- 1a). The nanosheets are randomly aligned, exhibiting smooth and clean surfaces with a mean width (\pm S.D.) of 151 ± 49 nm and length of 863 ± 131 nm (Figure 2- 1a). The TEM micrograph also reveals the same as FESEM in that the obtained nanomaterial exhibits sheet-like morphology, and the dimensions of the nanosheets also match the FESEM analysis, and the thickness of the CuO nanosheets are 15 ± 4 nm. (Figure 2- 1b). XRD pattern matches well with the base-centered monoclinic form of CuO (Figure 2- 1c). The characteristic peaks of copper oxide (PDF#48-1548) were obtained[21, 22]. The high intensity of peaks in the spectra and the absence of other peaks confirmed that the synthesized CuO nanosheets are crystalline and pure (Figure 2- 1c). Raman spectroscopy further corroborated the monoclinic crystal phase (Figure 2- 1f) of CuO nanosheets. The Raman spectra of CuO revealed three strong peaks at 267, 315, and 518 cm^{-1} , corresponding to the monoclinic orientation of A_{1g} , B_{1g} , and B_g vibrational modes of CuO nanosheets, respectively[23]. Further, the chemical composition of the synthesized CuO nanosheets was examined by FTIR spectroscopy (Figure 2- 1g). The bands at 614 cm^{-1} and 1014 cm^{-1} indicate different modes of bending vibration of the Cu-O bond. The appearance of the peak at 1642 cm^{-1} indicates the stretching vibration of the Cu-O bond of CuO nanosheets. The bands at 3449 cm^{-1} belong to the asymmetric stretching vibrational mode of the O-H bond of absorbed water. Additionally, the optical property of

synthesized CuO nanosheets was examined by UV–vis spectrophotometer (Figure 2- 1h). The typical UV–vis spectrum of CuO nanosheet demonstrates an excitation band at ≈ 365 nm and ≈ 297 nm[24].

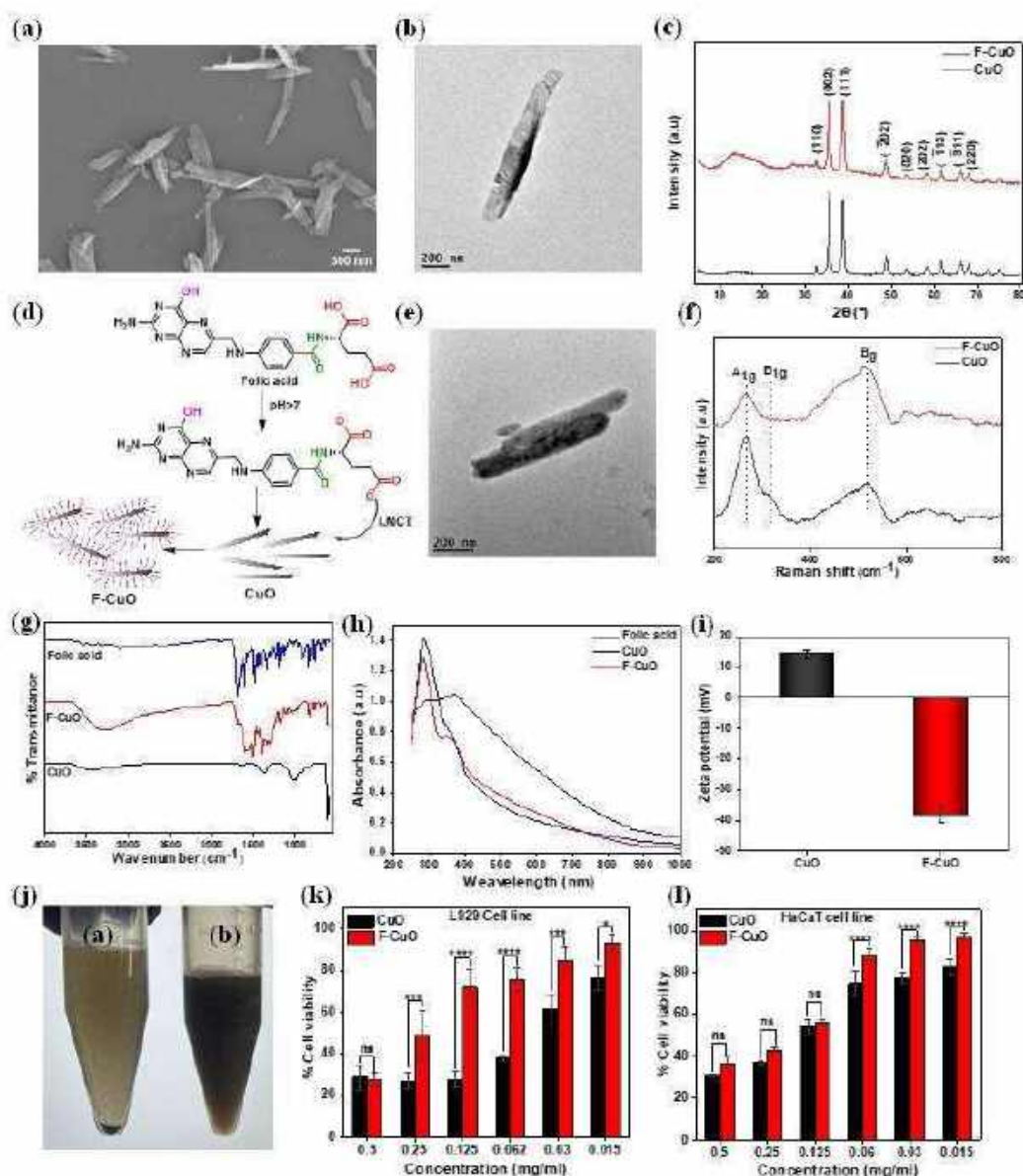


Figure 2- 1: Nanomaterial characterization (a) SEM image of synthesized CuO nanomaterial. (b) TEM micrograph of CuO (c) Powder X-ray diffraction of CuO and F-CuO. (d) Schematic representation of surface modification of CuO with folic acid as a bioligand. (e) TEM micrograph of F-CuO nanosheet. (f-i) (f) Raman spectra, (g) FTIR spectra, (h) UV vis spectra and (h) zeta potential of CuO and F-CuO (j) Digital image of aqueous dispersion of (a) CuO

and (b) F-CuO. (k, l) MTT assay to evaluate the cytocompatibility of CuO and F-CuO nanomaterials against (k) L929 fibroblasts (l) HaCaT keratinocytes. Ordinary 2-way ANOVA with Sidak's multiple comparisons test was performed. **** indicates $p < 0.0001$, *** indicates $p < 0.001$, * indicates $p < 0.05$ and ns indicates statistically non-significant

After successfully synthesizing CuO nanosheets, they were modified with folic acid ligands via ligand-to-metal charge transfer at basic pH (Figure 2- 1d). The motivation for the modification was multifold, as follows: (1) enhance the dispersion of CuO nanosheets in an aqueous medium (Figure 2- 1j), (2) decrease the cytotoxicity of CuO nanosheets, (3) enable uniform distribution of CuO nanosheets within the hydrogel with crosslinking chemistry, and (4) facilitate interactions with folic receptors of cancer cells in case of use nanomaterials for anticancer activity for drug delivery and/or photothermal effect. After the modification of CuO with folic acid, no alteration in the morphology of F-CuO was observed (Figure 2- 1e). The XRD pattern of the F-CuO is similar to the CuO phase but has a broad peak in the range of 11° to 17° , indicating the conjugation of folic acid to CuO nanosheets (Figure 2- 1c). Raman signal of F-CuO does not significantly differ from CuO (Figure 2- 1f). The FTIR study further confirmed folic acid interaction with CuO nanosheet. FTIR spectra of F-CuO showed that there was no covalent conjugation of folic acid with CuO nanosheets but rather ionic interactions between them. The absorbance at 1681 cm^{-1} , 1505 cm^{-1} , 1180 cm^{-1} , and 769 cm^{-1} indicated the successful modification of folic acid molecules onto CuO nanosheets' surface (Figure 2- 1g). This conjugation was further confirmed by UV vis spectroscopy and Zeta potential measurements. The characteristic absorbance of the F-CuO nanosheet shifted to $\approx 352\text{ nm}$, indicating the interaction between folic acid and CuO (Figure 2- 1h). Zeta potential measurements showed that the surface zeta potential value of CuO and F-CuO is 14.1 mV and -38.2 mV , respectively (Figure 2- 1i). The increased negative value in zeta potential value indicates the interaction of Folic acid on the surface of CuO nanosheets. The negatively charged

carboxyl group in the folic acid at basic pH is easily conjugated with positively charged Cu in CuO nanosheets through ligand-to-metal charge transfer. These measurements confirmed the successful modification of the surface of CuO nanosheets by the attraction of the carboxyl group of Folic acid.

Cytotoxicity of the CuO nanosheets was evaluated by MTT assay against L929 fibroblast and HaCaT keratinocyte cells exposed to systematically varied concentrations of the nanomaterials. Cytotoxicity decreased markedly when the CuO nanosheet was modified with folic acid (Figure 2- 1 (k, l)). Since more than 50% of cells are viable when directly exposed to 0.125 mg / mL of F-CuO nanosheets, we used 0.1 mg /mL F-CuO nanosheet concentration in hydrogel for further studies.

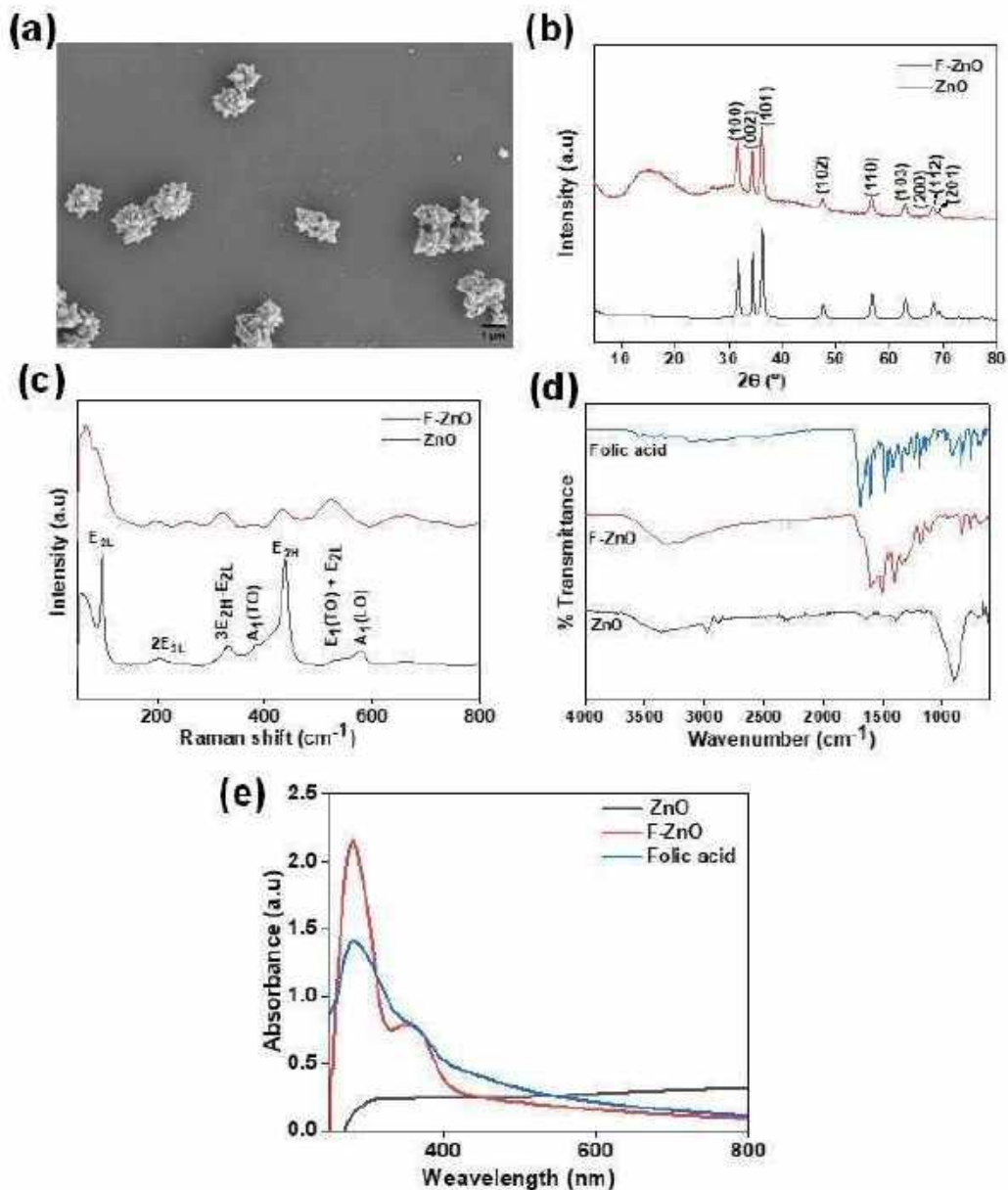


Figure 2- 2: Characterization of ZnO nanomaterials. (a) SEM micrographs of synthesized ZnO, (b) Powder X-ray diffraction of ZnO and F-ZnO, (c, d) Raman spectra (c) and FTIR spectra (d) of ZnO and F-ZnO.(e) UV vis spectroscopy of ZnO and F-ZnO nanomaterials.

Notably, this approach to surface functionalize of nanomaterials with folic acid as a bioligand is generic and can be implemented for other metallic nanomaterials. We synthesized ZnO nanoflowers, functionalized them with folic acid, and characterized the modification to further demonstrate the broad application of this approach to other nanomaterials (Figures 2- 2).

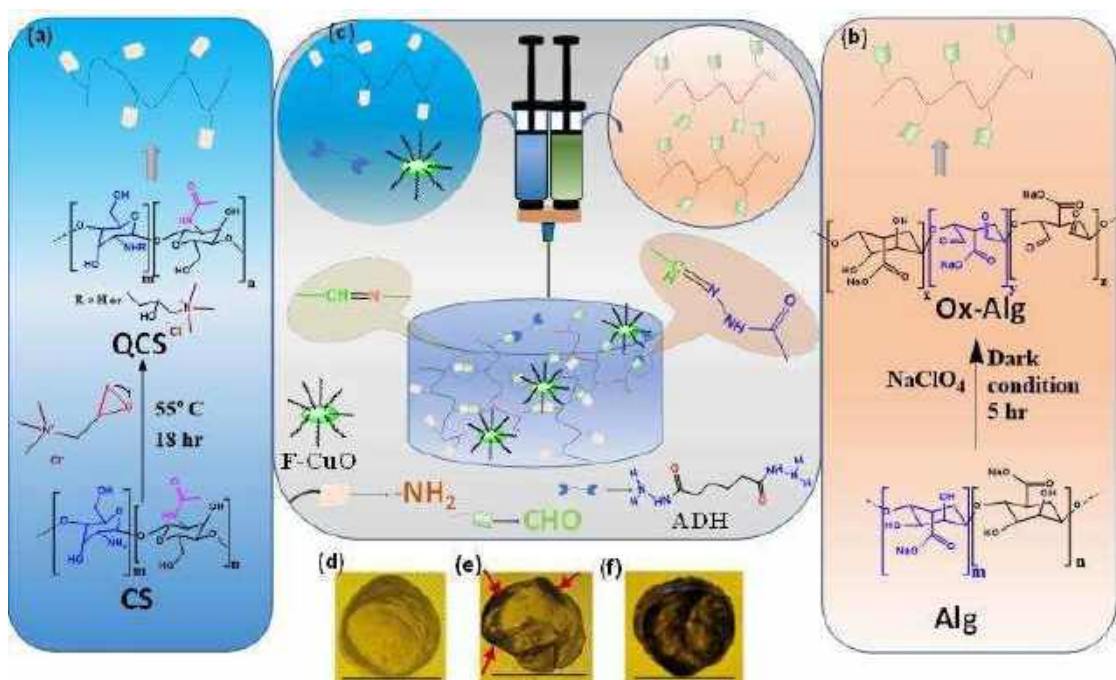
The yield of ZnO nanoflowers synthesis is 91 to 95%. The FESEM images reveal that the obtained products possess flower-like morphology (Figure 2- 2a). The nanoflowers are randomly arranged with a dimension of $1 \pm 0.3 \mu\text{M}$ (Figure 2- 2a). The XRD pattern of ZnO nanoflowers shows the typical peaks at $2\theta = 31.7^\circ, 34.4^\circ, 36.2^\circ, 47.4^\circ, 56.6^\circ, 63.0^\circ$ and 68.0° corresponding to the planes (1 0 0), (0 0 2), (1 0 1), (1 0 2), (1 1 0), (103), (112) respectively, which are indexed to a Wurtzite hexagonal ZnO structure, and it was matched with the JCPDS files (JCPDS card no. 36-1451)[25, 26] (Figure 2- 2b). The XRD pattern of the F-ZnO nanoflowers is similar to the ZnO phase but has a broad peak in the range of 10° to 20° , which indicates the conjugation of folic acid at the surface of the ZnO nanoflowers (Figure 2- 2b). The Raman spectrum consists of four peaks at about 98, 380, 438, and 580 cm^{-1} , corresponding to the E_{2L} , $A_1(\text{TO})$, E_{2H} , and $A_1(\text{LO})$ fundamental phonon modes of hexagonal ZnO, respectively (Figure 2- 2c). The Raman peak at about 205 cm^{-1} was assigned to the $2E_{2L}$ second-order phonon mode[27]. The Raman signal of F-ZnO does not significantly differ from pure ZnO nanoflowers (Figure 2- 2c), but the Raman signal is decreased considerably due to surface modification by ligand. The FTIR study further confirmed folic acid interaction with ZnO nanoflowers. FTIR spectra of F-ZnO showed no covalently conjugated folic acid with ZnO nanosheet but rather ionically interaction between them. The absorbance at 1680 cm^{-1} , 1506 cm^{-1} , 1181 cm^{-1} , and 759 cm^{-1} indicated that the successful modification of folic acid molecules onto the ZnO nanoflower surface was mainly due to charge transfer interaction (Figure 2- 2d). This conjugation was further confirmed by UV vis spectroscopy. The characteristic absorbance of the F-CuO nanosheet shifted to $\approx 352 \text{ nm}$, indicating the interaction between folic acid and ZnO (Figure 2- 2e).

However, further studies were conducted with CuO and F-CuO nanosheets to develop multi-biofunctional injectable hydrogel.

2.2.2 Preparation and characterizations of hydrogels

Positively-charged quaternized chitosan (QCS) was synthesized using glycidyl trimethyl ammonium chloride (GTMAC) as an etherifying agent in deionized water under acidic conditions. In an acidic aqueous medium, the epoxy rings of GTMAC conjugations mostly predominantly occur with the amine group of the chitosan backbone[28, 29] (Schematic 2- 1a). This functionalization of the chitosan was confirmed by ^1H NMR and FTIR. A strong peak at $\approx \delta$ 3.17 ppm was observed, demonstrating the presence of methyl groups in the quaternary ammonium side chains ($-\text{N}^+(\text{CH}_3)_3$) (Figure 2- 3b). The remaining characteristic resonances are assigned to protons in quaternized side chains and chitosan main chains, confirming the functionalization of chitosan.

The FTIR spectra of CS revealed the broad peak at around 3405 cm^{-1} is ascribed to $-\text{OH}$ and $-\text{NH}$ stretching vibrations. The characteristic peaks at 1657 and 1562 cm^{-1} correspond to the $\text{C}=\text{O}$ stretch of the amide I and $-\text{NH}_2$ bands of chitosan, respectively (Figure 2- 3a). The peaks at 1151 cm^{-1} and $1075\text{--}1002\text{ cm}^{-1}$ are ascribed to anti-symmetric stretching of the $\text{C}-\text{O}-\text{C}$ of the saccharide backbone and the $\text{C}-\text{O}$ stretching skeletal vibrations, respectively. In comparison with CS, several noticeable changes occur in the FTIR spectra of QCS. A strong peak at 1475 cm^{-1} of QCS is attributed to the $\text{C}-\text{H}$ bending of the trimethylammonium group, confirming the existence of the quaternary ammonium salt, which confirms the functionalization of chitosan[30] (Figure 2- 3a). The degree of quaternization (DQ) of QCS was determined from ^1H NMR analysis, which is $\approx 31\%$.



Scheme 2- 1: (a) Synthesis scheme of QCS from chitosan (CS), (b) Synthesis scheme of Ox-Alg from Alginate (Alg), (c) Schematic demonstration for fabrication of the F-CuO/Ox-Alg/QCS injectable hydrogel. Digital image of (d) Ox-Alg/QCS NH, (e) CuO/Ox-Alg/QCS NH (red arrows indicate the non-homogeneous distribution of CuO nanosheet in the hydrogel), (f) F-CuO/Ox-Alg/QCS NH. Scale bar = 1 cm.

Similarly, Ox-Alg was synthesized by cleavage of vicinal hydroxyl groups access on the Alg (Scheme 2- 1 b). The characteristic peak of Alg at 1024 cm^{-1} is ascribed to the glycosidic linkage of Alg, and the peaks at 1088 cm^{-1} and 2911 cm^{-1} are associated with C-O, C-H, stretching, and vibrations, respectively[31]. Also, the FTIR spectrum of Ox-Alg confirmed the characteristic peaks at 1740 cm^{-1} and 878 cm^{-1} , which are attributed to the aldehyde symmetrical vibration and the hemiacetal bond formation, respectively[32] (Figure 2- 3a).

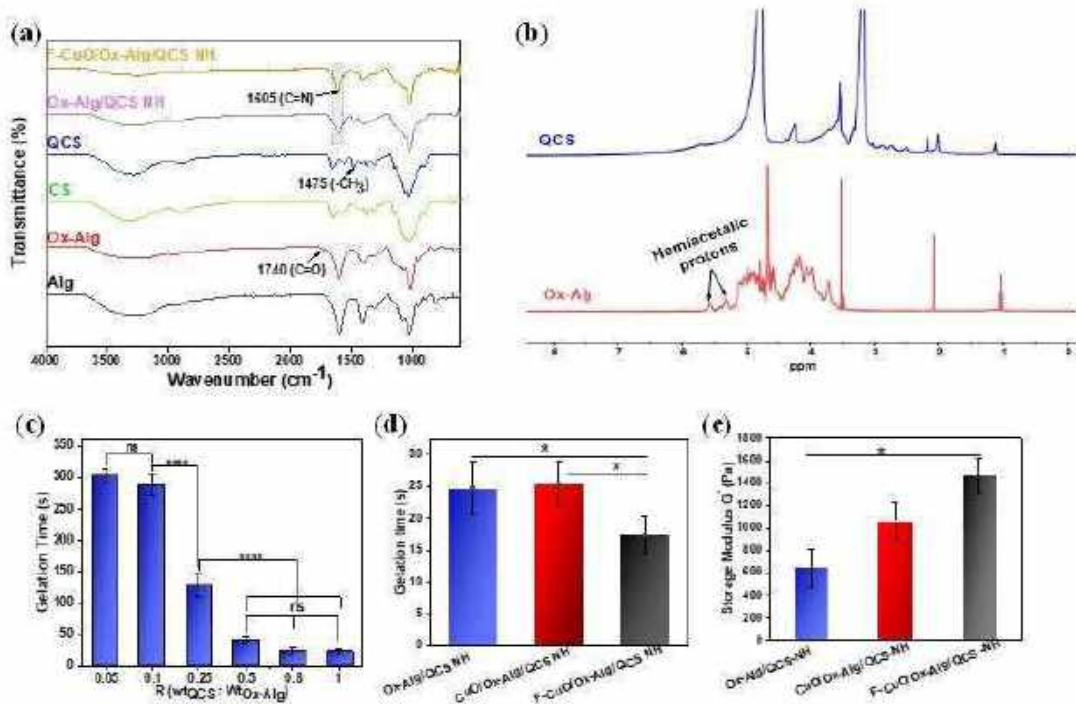


Figure 2- 3: (a) FTIR spectra of CS, QCS, Alg, Ox-Alg, F-CuO/Ox-Alg/QCS NH, Ox-Alg/QCS NH. (b) ¹H NMR spectra of QCS and Ox-Alg (c) Gelation time Ox-Alg/QCS hydrogel with different R (R = Wt_{QCS}: Wt_{Ox-Alg}) (d, e) Gelation time (d) and storage modulus (e) of F-CuO/Ox-Alg/QCS NH and Ox-Alg/QCS NH with R = 0.8. Ordinary one-way ANOVA with Tukey's multiple comparisons test was performed. **** indicates $p < 0.0001$, * indicates $p < 0.05$ and ns indicates statistically non-significant

The ¹H NMR spectrum of Ox-Alg also confirmed the formation of the aldehyde group. The two characteristic signals at δ 5.5 and δ 5.3 ppm proved the formation of the hemiacetalic proton due to the aldehyde groups of the monomeric saccharide units and the neighboring hydroxyl groups of the unoxidized ring residue (Figure 2- 3b), thereby confirming the formation of the Ox-Alg. The literature also indicates the same observation, which is likely the cause of the discreet nature of the actual aldehyde protons peaks in the ¹H NMR spectrum[13, 33]. Consequently, using NMR spectroscopy, quantitative determination of the DO was not viable due to the discrete and uncertain characteristics of the aldehyde signal. Therefore, the

average DO of the Ox-Alg, as assessed via iodometric titration (conducted in triplicate), was 71%.

After successfully synthesizing F-CuO, QCS, and Ox-Alg, hydrogels were formed by rapid Schiff base crosslinking chemistry at room temperature in PBS (Scheme 2-1(c, d, e f)). The digital image shows that F-CuO nanosheets are more homogeneously distributed in the hydrogel upon modification with folic acid (scheme 2- 1e) rather than unmodified CuO sheets, which show localized agglomeration (red arrows, Scheme 2- 1f). This work introduces two dynamic covalent bonds, namely, imine and acylhydrazone bonds, to engineer the hydrogel. The aldehyde groups of Ox-Alg formed imine bonds when they reacted with the amino groups of QCS, while the aldehyde groups of Ox-Alg reacted with the amino groups of ADH to form acylhydrazone bonds (Scheme 2- 1c). This small amount of ADH is used in the hydrogel system to introduce dynamic imine bonds in the crosslinking mechanism, which impart better self-healing efficiency to the hydrogel. The optimization and benefit of using ADH in this hydrogel formulation were noted in our previous study[13]. The FTIR spectra of Ox-Alg/QCS NH and F-CuO/Ox-Alg/QCS NH verified this dynamic Schiff base crosslinking (Figure 2- 3a). The peak of both hydrogels at 1605 cm^{-1} corroborates the successful formation of the -C=N bonds between the QCS, ADH, and F-CuO amino group with the aldehyde groups of Ox-Alg. However, the reduction of the aldehyde peak in both hydrogel spectra demonstrates the formation of the Schiff base linkage[34, 35]. Regardless of the crosslinker type, no reaction ever proceeds with 100% yield. The gel (%) of Ox-Alg/QCS NH and CuO/Ox-Alg/QCS NH is $93 \pm 4\%$ and 92 ± 4 , whereas F-CuO/Ox-Alg/QCS NH is $96 \pm 3\%$, which significantly provides a good indication for the successful hydrogel formation and an efficient crosslinking process.

Gelation time is an important consideration for determining the injectability of a hydrogel. Therefore, optimization of the gelation time is essential since a very fast gelation rate can

induce gelling before the solution is injected at the target site. In contrast, a prolonged gelation rate may result in undesired diffusion of the uncrosslinked precursors from the targeted site. The gelation time was determined at different weight ratios ($R = 0.05$ to 1) of the hydrogels through the vial tilting method (Figure 2- 3c). The desired gelation time (24 ± 4 s) was obtained for Ox-Alg /QCS NH at $R = 0.80$. Thus, this gel formulation was used for further experiments and characterization. The gelation time decreased to 17 ± 3 s when F-CuO was added to the F-CuO/Ox-Alg/QCS NH system (Figure 2- 3d). In contrast, there is no significant difference ($p < 0.05$, one-way ANOVA) in gelation time when unmodified CuO was added instead of F-CuO to the CuO/Ox-Alg/QCS NH system with the same formulation (Figure 2- 3d).

We also measured the storage modulus from rheological studies to analyze the impact of nanomaterials on the mechanical properties of the gel (Figure 2- 3e). The storage modulus of F-CuO/Ox-Alg/QCS NH system enhanced from 640 ± 177 Pa to 1463 ± 150 Pa with the addition of F-Cuo, whereas the storage modulus of CuO/Ox-Alg/QCS NH system increased to 1060 ± 173 Pa with the incorporation of CuO.

These trends in gelation time and mechanical properties are a consequence of the synergy of the following two effects: (i) F-CuO induces more crosslinking points in the F-CuO/Ox-Alg/QCS NH via imine bonds associated with acylhydrazone bonds and the additional hydrogen bonds with the folic ligand on the nanomaterial surface; (ii) the presence of hard F-CuO nanoparticles in a soft hydrogel matrix of the composite. Notably, as a consequence of folic ligand modification, F-CuO is more homogeneously distributed in the F-CuO/Ox-Alg/QCS NH system than the unmodified CuO in the CuO/Ox-Alg/QCS NH (Scheme 2- 1 (e, f)) composite, which further augments the modulus of the former over the latter.

2.2.3 Pore morphology

The pore morphology of the hydrogels was visualized by scanning electron microscopy (Figure 2- 4 (a, b)). Pore size and morphology reveal a trend between the crosslinking density and the structure of hydrogels. F-CuO/Ox-Alg/ QCS NH demonstrates a smaller pore size and a dense network structure (Figure 2- 4b) than the Ox-Alg /QCS NH (Figure 2- 4a) hydrogel. The SEM micrograph of F-CuO/Ox-Alg/ QCS NH shows an interconnected three-dimensional porous network with an average pore size of $114 \pm 24 \mu\text{m}$. The pore size of Ox-Alg /QCS NH increased to $130 \pm 28 \mu\text{m}$, which indicates a slight decrease in crosslinking density (Figure 2- 4d). The interconnected porosity of a hydrogel is crucial for the effective loading of nanoparticles, drugs, cells, proteins, or any therapeutic agents and their subsequent release. Furthermore, the porosity of the hydrogels was assessed based on Archimedes' Principle using a specific gravity bottle[36], and the porosity is $84 \pm 3.5 \%$ and $80 \pm 3.2 \%$ for Ox-Alg /QCS NH and F-CuO/Ox-Alg /QCS NH, respectively. F-CuO nanosheets were observed to disperse well and embedded effectively in the hydrogel (Figure 2- 4 (c1 to c4)) due to the chemical interaction of F-CuO nanosheet and Ox-Alg during the formation of the hydrogel and hydrogen bonding among the prepolymers, which usually differs from the traditional loading of nanomaterials in the hydrogel. The EDX spectra confirm the presence of F-CuO in the hydrogel, which was further validated by EDX mapping of the corresponding area of the F-CuO/Ox-Alg/QCS NH system (Figure 2- 4 (e, f)).

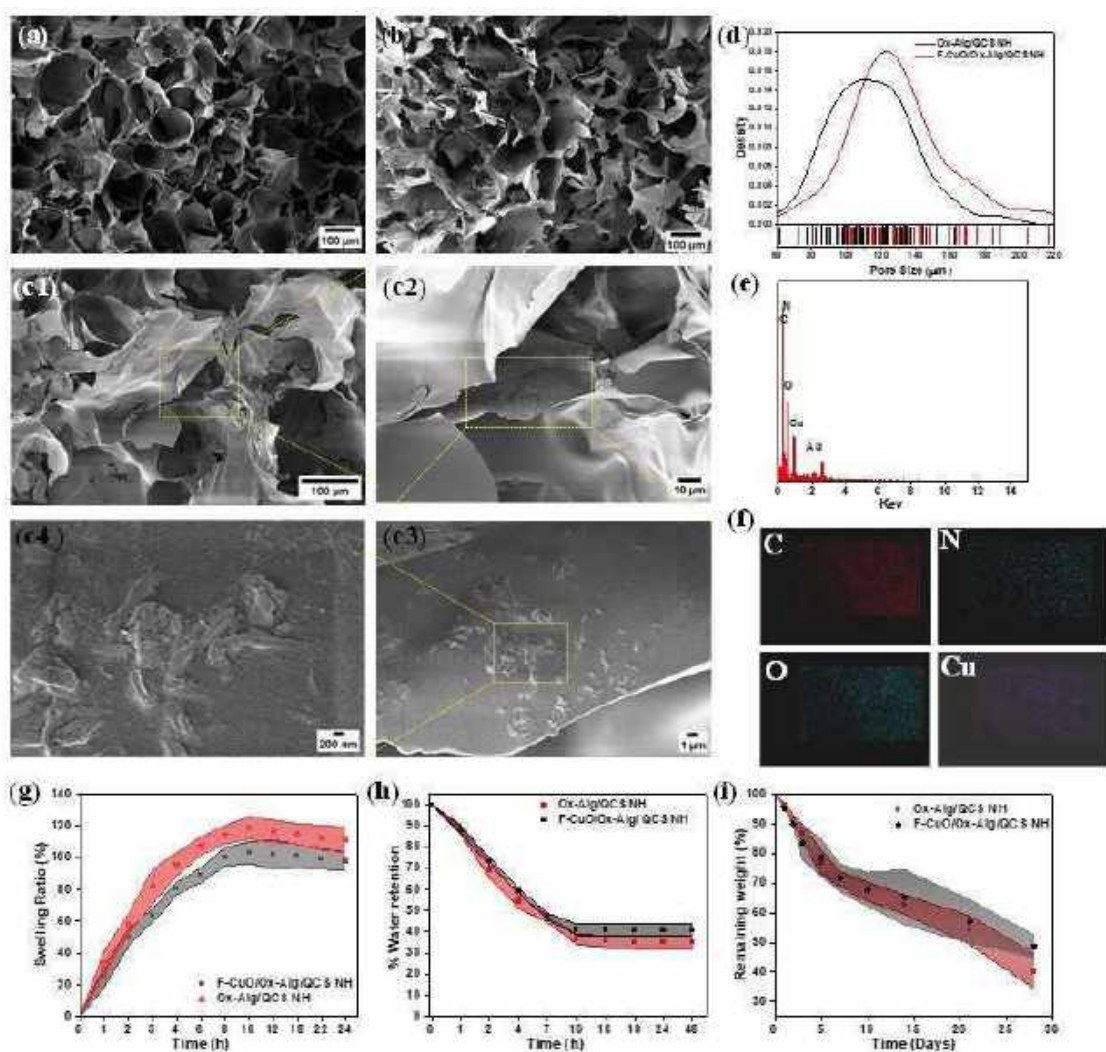


Figure 2- 4: (a, b) SEM micrographs of (a) Ox-Alg /QCS NH, (b) F-CuO/Ox-Alg/ QCS NH. (c1 - c4) SEM micrograph of F-CuO nanomaterials distribution in the F-CuO/Ox-Alg/ QCS NH with different magnification confirming the presence of the nanomaterial, (d) pore size analysis of F-CuO/Ox-Alg/ QCS NH and Ox-Alg /QCS NH, (e) EDX spectrum of the corresponding F-CuO/Ox-Alg/ QCS NH at the location marked in c4, (f) Elemental maps of F-CuO/Ox-Alg/ QCS NH, (g) Swelling profiles of F-CuO/Ox-Alg/ QCS NH and Ox-Alg /QCS NH in PBS at 37° C, (h) Water retention profiles of F-CuO/Ox-Alg/ QCS NH and Ox-Alg /QCS NH in PBS at 37° C (i) Degradation profiles of F-CuO/Ox-Alg/ QCS NH and Ox-Alg /QCS NH in PBS at 37° C.

2.2.4 Swelling behavior and water retention

F-CuO/Ox-Alg/ QCS NH displayed a swelling percentage of 103 %, whereas the swelling percentage of Ox-Alg /QCS NH hydrogel was higher at 118% (Figure 2- 4g). These results are a consequence of the differences in crosslinking density of the hydrogel system. The increased crosslinking in F-CuO/Ox-Alg/ QCS NH restricts water uptake compared to that in the Ox-Alg /QCS NH system[37].

The water retention property of a hydrogel is a measure of its ability to retain moisture for tissue engineering. The water retention capacity of the hydrogels was evaluated by assessing water loss over time in humidified conditions (55%). The water retention ability of both F-CuO/Ox-Alg/ QCS NH and Ox-Alg /QCS NH system decreased with time (Figure 2- 4h). The water retention capability of both hydrogels is ≈ 10 h, and the kinetics of the water retention is similar for both F-CuO/Ox-Alg/ QCS NH and Ox-Alg /QCS NH systems (Figure 2- 4h).

2.2.5 Biodegradability of the hydrogels

The biodegradability of the hydrogels was investigated by immersing them in PBS at 37°C and physiological pH (7.4). A gradual decrease in weight was observed with time due to the hydrolysis of Schiff base linkages, as reported in our previous study. F-CuO/Ox-Alg/ QCS NH degraded 48 ± 3 % after 28 days, whereas Ox-Alg/QCS NH showed weight loss of 40 ± 5 % (Figure 2- 4i). This decrease in the degradation rate in the F-CuO based hydrogel system is due to an increase in crosslinking density.

2.2.6 Rheological properties of the hydrogels

Viscoelastic properties and injectability of the hydrogels were elucidated through rheological measurements. The angular frequency sweep was studied to characterize the viscoelasticity of the hydrogels (Figure 2- 5a). G' (elasticity) and G'' (viscosity) were measured as a function of

ω within the angular frequency range from 0.01 to 100 rad s⁻¹. The storage modulus($G'(\omega)$) was greater than loss modulus ($G''(\omega)$), and damping factor ($\tan \delta$) was less than 1.0 for both the hydrogels, implying an entanglement of the 3D gel network structure and the controlling factor of the elastic nature of the hydrogel[38, 39], which corresponds to the typical viscoelastic material[40]. Then, the strain amplitude sweep was performed (Figure 2- 5b) to investigate the crossover point between G' and G'' of the hydrogel. It was observed that G' value started to drop upon reaching 25% strain, and a crossover with G'' happened at 164% of strain for F-CuO/Ox-Alg/ QCS NH, whereas the crossover point occurred at 299% for Ox-Alg/ QCS NH. This crossover point indicates the gel-to-sol transition of the hydrogel, indicating a conversion of the gel network to a quasi-liquid sol state.

Continuous step strain measurement was used to assess the rheological recovery behavior of the hydrogels based on the findings of the strain amplitude sweep (Figure 2- 5(c, d)). The gel-sol transition behavior of both the hydrogels was found to be reversible in nature, and interestingly, when the applied oscillatory strain was reduced from 500% to 5%, the system quickly recovered from the quasi-liquid sol to the gel state (Figure 2- 5(c, d)). Under 500% strain, hydrogel systems continued in a quasi-liquid state, and upon returning the strain to 5%, both G' and G'' recovered fully without any delay or fatigue. This procedure was similar for both gels and could be performed over many repetition cycles.

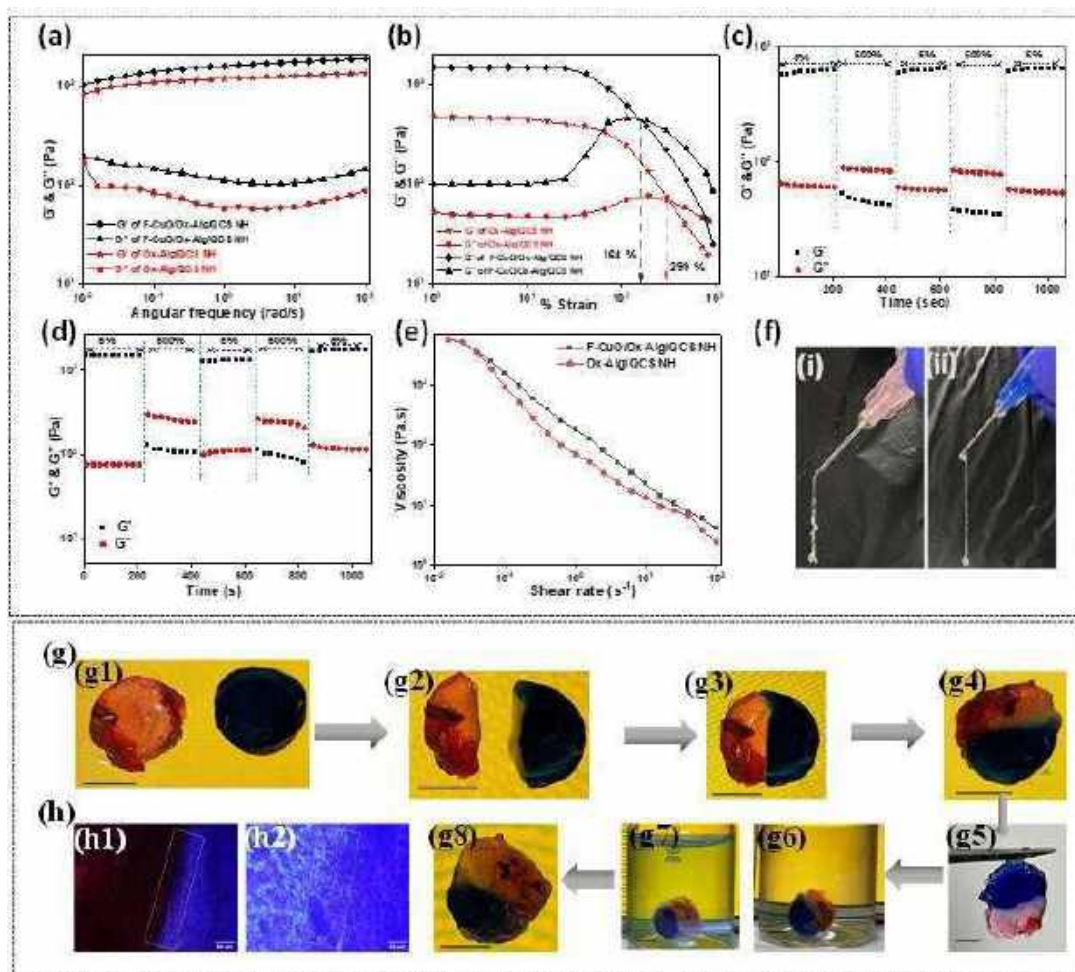


Figure 2- 5: (a-e) Rheological characterization of F-CuO/Ox-Alg/ QCS NH and Ox-Alg /QC NH. (a)) frequency sweep in 0.01 to 100 rad s^{-1} range at a constant strain of 1% at 25°C . (b) strain amplitude sweep in the range of 1 to 800% strain at a constant angular frequency of 10 rad s^{-1} at 25°C . (c, d) F-CuO/Ox-Alg/ QCS NH (c) and Ox-Alg /QC NH (d) are the time scan tests, measured G' and G'' of the hydrogel as a function of time with an alternating strain of 5% and 500% with a constant angular frequency of 10 rad s^{-1} for 200 s at 25°C . (e) Thixotropic flow sweep test with the variable shear rate from 0.1 to 100 s at 25°C . (f) Photograph of extrudability and injectability of F-CuO/Ox-Alg/ QCS NH through (i) 20- and (ii) 22-gauge needles. (g) Digital images of self-healing activity of F-CuO/Ox-Alg/ QCS NH. (g1) Two hydrogels, one stained with rhodamine b and the other one stained with methylene blue (g2)

Both hydrogels were cut into two pieces (g3) two alternate colors of hydrogel pieces placed adjacently (g4) the self-healed hydrogels after 3 h healing at 37°C (g5) the self-healed hydrogel hung from one side, (g6, g7) to check its stability, self-healed hydrogel immersed in PBS (pH = 7.4) for (g6) 6 h and (g7) 24 h, (g8) healed hydrogel retained its shape after immersion. The scale bar of all images is 1 cm. (h) microscopic evidence of healing activity, the optical image of F-CuO/Ox-Alg/ QCS NH (h1) before self-healing and (h2) after 3 h of self-healing. The scale bar of image h1 and h2 is 50 μm .

A shear rate sweep with a shear rate variation from 0.1 to 100 s^{-1} was investigated to gain more insight into the shear-thinning behavior of hydrogels (Figure 2- 5e). As the shear rate increased, the viscosity of the hydrogels rapidly decreased, and hydrogels showed non-Newtonian shear thinning behavior (Figure 2- 5e). These outcomes validate that both hydrogels have favorable shear-thinning properties for injecting through a needle and syringe for potential administration in a minimally invasive form, which was demonstrated by injecting the hydrogels through 20- and 22-gauge needles. (Figure 2- 5f). These findings suggest that the nanocomposite hydrogel possesses good thixotropic and shear-thinning characteristics and holds potential for use as an injectable soft material¹.

2.2.7 Self-healing performance of the hydrogel

The self-healing property is beneficial for hydrogel to recover the damage after its implantation. It is also beneficial for preventing the spontaneous outflow of loaded drugs or particles at nontargeted sites[41]. Any mechanical damage during use can heal to restore its barrier function. A macroscopic self-healing test was performed to assess the self-healing ability of the hydrogels. Each of the two hydrogels with red (stained with rhodamine B) or blue (stained with methylene blue) colors (Figure 2- 5 g1) were cut into two parts using a surgical blade (Figure 2- 5 g2). The two cut pieces of alternating colors hydrogels were placed adjacent to each other (Figure 2- 5 g3) at room temperature. After 3 h, the color of the gel at the edge of

the joining became indistinguishable as the two pieces of the hydrogel fused, suggesting that they supported each other without any external aid (Figure 2- 5 (g4, g5)). The proficiency of the two gel pieces to yield a single entity demonstrated the self-healing performance of the F-CuO/Ox-Alg/ QCS NH. Furthermore, the stability of the self-healed hydrogel pieces was confirmed by their integrity up to 24 h in PBS (pH 7.4) (Figure 2- 5 (g6, g7)). Additionally, the closer of the gap between the two gel fragments post-healing corroborated with the self-healing capability of the F-CuO/Ox-Alg/ QCS NH system as observed in optical micrographs (Figure 2- (5h1, 5h2)).

2.2.8 Adhesive properties of the hydrogel

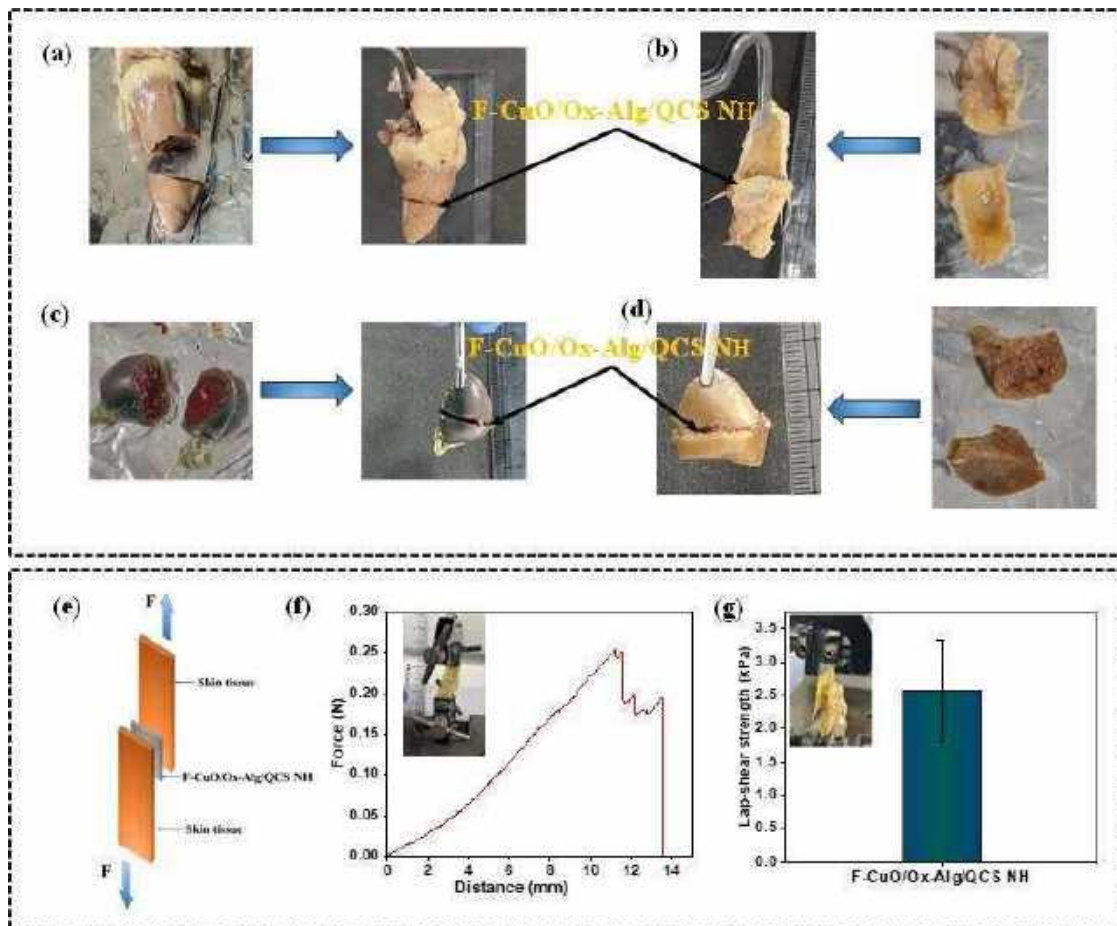


Figure 2- 6: Adhesive properties of the F-CuO/Ox-Alg/QCS NH. (a-d) Photographs of the F-CuO/Ox-Alg/QCS NH adhered to different moist biological tissues: (a) heart, (b) skin, (c) spleen, (d) liver. (e) Schematic representation of the lap-shear tests experiment. (f) Typical

force-displacement curves and (g) lap-shear strength of the F-CuO/Ox-Alg/QCS NH. Values represent the mean, and error bars represent the standard deviation ($n = 3$).

Since injuries are typically accompanied by bleeding, the adhesive properties of hydrogels in a moist environment are crucial for their application in the biomedical field[42, 43]. F-CuO/Ox-Alg/QCS NH system exhibited good potential adhesion to multiple organs, as shown in Figure 2- 6 (a-d). Herein, the adhesive strength was measured by lap-shear tests (Figure 2- 6e, 6f), and the lap-shear strength of the F-CuO/Ox-Alg/QCS NH is ≈ 2.56 kPa (Figure 2- 6g). The adhesion strength was attributed to the multi-interactions such as ionic interactions, hydrogen bonding due to the hydroxyl group of QCS and Ox-Alg, free-CHO group of Ox-Alg, and amine and quaternized ammonium group of modified chitosan with various proteins of the tissue. Therefore, this hydrogel system could be expected to be widely used as an adhesive hydrogel in wound dressing, surgical band-aid, and other biomedical fields.

2.2.9 Cytocompatibility of the hydrogels

A critical consideration for the effective functioning of a hydrogel as a delivery vehicle and for tissue engineering applications is cytocompatibility[44, 45]. The cytocompatibility of both hydrogels was studied with HaCaT keratinocytes. In the actual use of the hydrogel, it would be in direct contact with the skin keratinocytes and fibroblasts at the wound site. Hence, we rationally chose HaCaT cell lines to demonstrate the cytotoxicity of our materials. MTT assay was performed to quantitatively assess cell viability by exposing cells to conditioned media containing both degraded and leached products of the gels (Figure 2- 7a). Fresh medium served as the control. More than 80% of the cells were viable over 72 h for both hydrogels, indicating that hydrogels exhibit good cytocompatibility. These results were independently validated by Live/Dead assay, where red represents dead cells and green stained for live cells. Most of the cells were live, with their number increasing over time; however, a very small fraction of dead

cells was also observed (Figure 2- 7b). The F-actin and nuclei were stained to observe the morphology of the cells (Figure 2- 7c). Similar cell morphology was observed in conditioned medium treated cells as well as control groups, and the cells were healthy. Taken together, both hydrogels are cytocompatible.

2.2.10 Hemolysis induced by the hydrogels

In recent years, researchers have made efforts to design novel injectable hydrogels with outstanding blood compatibility, another critical consideration for their *in vivo* use. The blood compatibility of both the hydrogels at different wet weight concentrations (50 and 100 mg/mL) was assessed *in vitro* via a hemolysis assay. The noticeable color changes between the hydrogel-treated and the positive control groups are observed from the insets of Figure 2- 7d. Ox-Alg/ QCS NH and F-CuO/Ox-Alg/ QCS NH treated groups (Figure 2- 7d) show a canary yellow color, which is similar to the color of the negative control group (PBS). On the other hand, the positive control (Triton X-100) displays a bright red color due to full lysis of RBCs (inset of Figure 2- 7d (a)). The % hemolysis of Ox-Alg/ QCS NH at 50 and 100 mg/mL concentrations is about 3.5 and 3.6 %, whereas the % hemolysis of F-CuO/Ox-Alg/ QCS NH is 5.7 and 7.7%, respectively. Slightly higher % hemolysis in the case of F-CuO/Ox-Alg/ QCS NH than Ox-Alg/ QCS NH could be the reason for the presence of F-CuO np in the systems. However, statistically non-significant differences between Ox-Alg/ QCS NH and F-CuO/Ox-Alg/ QCS NH-treated groups were observed. These results suggest good blood compatibility of both hydrogels.

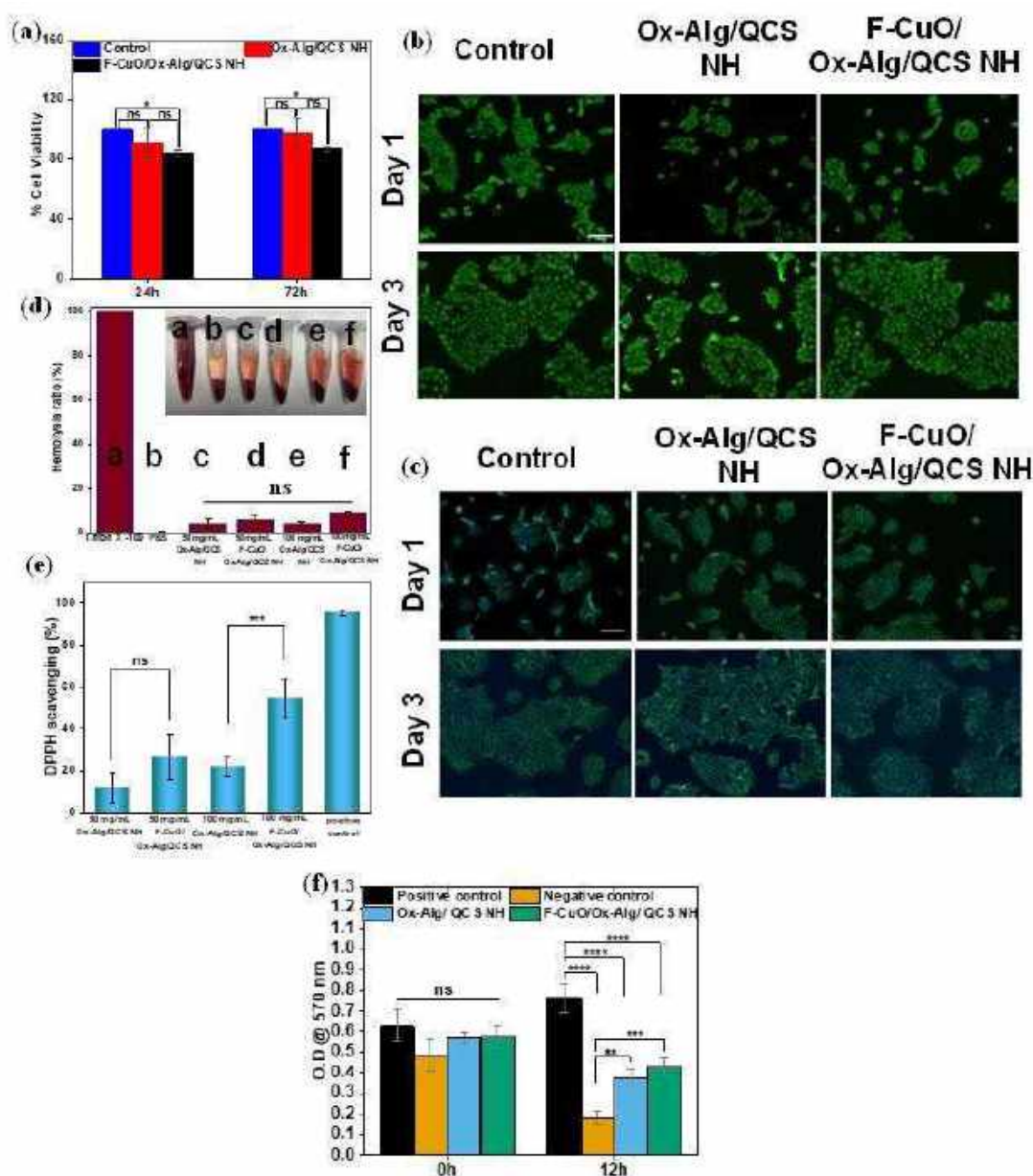


Figure 2- 7: Cytocompatibility of F-CuO/Ox-Alg/ QCS NH and Ox-Alg/ QCS NH assessed with HaCaT keratinocytes (a) Plot of MTT viability assay of cells exposed to conditioned medium. (b) Fluorescent images of live-dead assay (c) Fluorescence images revealing F-actin (red) and nuclear (blue) organization. (magnification 10 \times , scale bar = 100 μ m for all images of (b) and (c)). Control refers to fresh complete culture medium. (d) Hemolytic evaluation of F-CuO/Ox-Alg/ QCS NH and Ox-Alg/ QCS NH and representative optical photographs of the hemolysis test. (e) DPPH scavenging percentage by F-CuO/Ox-Alg/ QCS NH and Ox-Alg/ QCS NH with different concentrations and L-ascorbic acid as positive control. (f) L929 cell

viability against ROS in the treatment of Ox-Alg/ QCS NH and F-CuO/Ox-Alg/ QCS NH. Ordinary 2-way ANOVA with Sidak's multiple comparisons test was performed for (a). Ordinary one-way ANOVA with Tukey's multiple comparisons test was performed for (d) and (e). Ordinary 2-way ANOVA with Tukey's multiple comparisons test was performed for (f). * indicates $p < 0.05$, ** indicates $p < 0.01$, *** indicates $p < 0.001$, **** indicates $p < 0.0001$ and ns indicates statistically non-significant.

2.2.11 Free radical scavenging ability of the hydrogels

Abundance of free radicals in the wound site can enhance oxidative stress, leading to DNA breakage, enzyme inactivation, and lipid peroxidation. Herein, the antioxidant activities of both hydrogels were assessed by testing the scavenging efficiency for DPPH^{*}[46]. % DPPH scavenging of Ox-Alg/ QCS NH at 50 and 100 mg/mL concentrations was measured to be 12.0 ± 7 and 21.7 ± 4 %, respectively, which increased to 26.9 ± 10 and 54.6 ± 9 %, respectively, for F-CuO/Ox-Alg/ QCS NH (Figure 2- 7e). The large increase in % DPPH scavenging potential is due to F-CuO in the hydrogel. Aromatic groups in the folic acid scavenge the free radicals[47]. F-CuO/Ox-Alg/ QCS NH showed increased scavenging efficiency with the increase of hydrogel concentration. Overall, F-CuO/Ox-Alg/ QCS NH shows excellent antioxidant activity and has the potential for application in healing wounds.

The cytoprotection ability of the Ox-Alg/ QCS NH and F-CuO/Ox-Alg/ QCS NH against H₂O₂-induced ROS was analyzed by measuring the cell viability after the induction of the ROS (Figure 2- 7f). Initially (at 0 h), all the conditions showed non-significant differences in absorbance values. Significantly higher absorbance values were observed in the case of F-CuO/Ox-Alg/ QCS NH ($p < 0.001$) and Ox-Alg/ QCS NH ($p < 0.01$) treated cells than the negative control at 12 h after treatment with H₂O₂. A higher level of ROS is known to hamper cell functions and viability. However, ROS scavengers attenuate the effect of oxidative damage

on cell viability[48]. The ROS-scavenging of the F-CuO/Ox-Alg/ QCS NH imparted the cytoprotection ability.

2.2.12 *In vitro* scratch assay

Cell migration is a key hallmark of wound healing. Hence, the scratch assay was studied to evaluate the influence of hydrogels on cellular migration. Reduced serum condition (DMEM with 2.5 % FBS) was used in the wound healing assay to minimize the effect of proliferation. A time-dependent experiment (0 -20 h) was carried out to evaluate the potential of prepared F-CuO/Ox-Alg/ QCS NH to promote the migration of endothelial cells, as shown in Figure 2- 8a. The cells treated with F-CuO/Ox-Alg/ QCS NH migrated more significantly than those treated with Ox-Alg/ QCS NH and control (untreated) cells (Figure 2- 8a). The healed area of cells treated with F-CuO/Ox-Alg/ QCS NH was $\approx 80\%$, in contrast to $\approx 65\%$ for the treated with Ox-Alg/ QCS NH and $\approx 24\%$ for the (untreated) control (Figure 2- 8b). F-CuO/Ox-Alg/ QCS NH-treated cells migrated significantly faster than the treated with Ox-Alg/ QCS NH and control group because of the combined effect of F-CuO in addition to chitosan and alginate. Chitosan aids in proliferation of fibroblasts and regeneration of the wound area, and the presence of glucosamine is reported to accelerate the healing process with minimal scarring[49]. Chitosan and alginate also promote revascularization and protect against atherosclerosis[50]. Also, chitosan can modulate inflammation to accelerate the healing process[51]. On the other hand, Cu enhances the angiogenesis process and helps in the formation and stabilization of extracellular matrix tissue proteins, which are critical events of tissue formation, such as skin[52]. Cu nanoparticles also play a crucial role in cell proliferation, reepithelization, anti-inflammatory, and matrix remodeling[53, 54]. Thus, the addition of F-CuO in F-CuO/Ox-Alg/QCS NH enhanced healing capacity effectively due to the synergistic effect of chitosan and CuO.

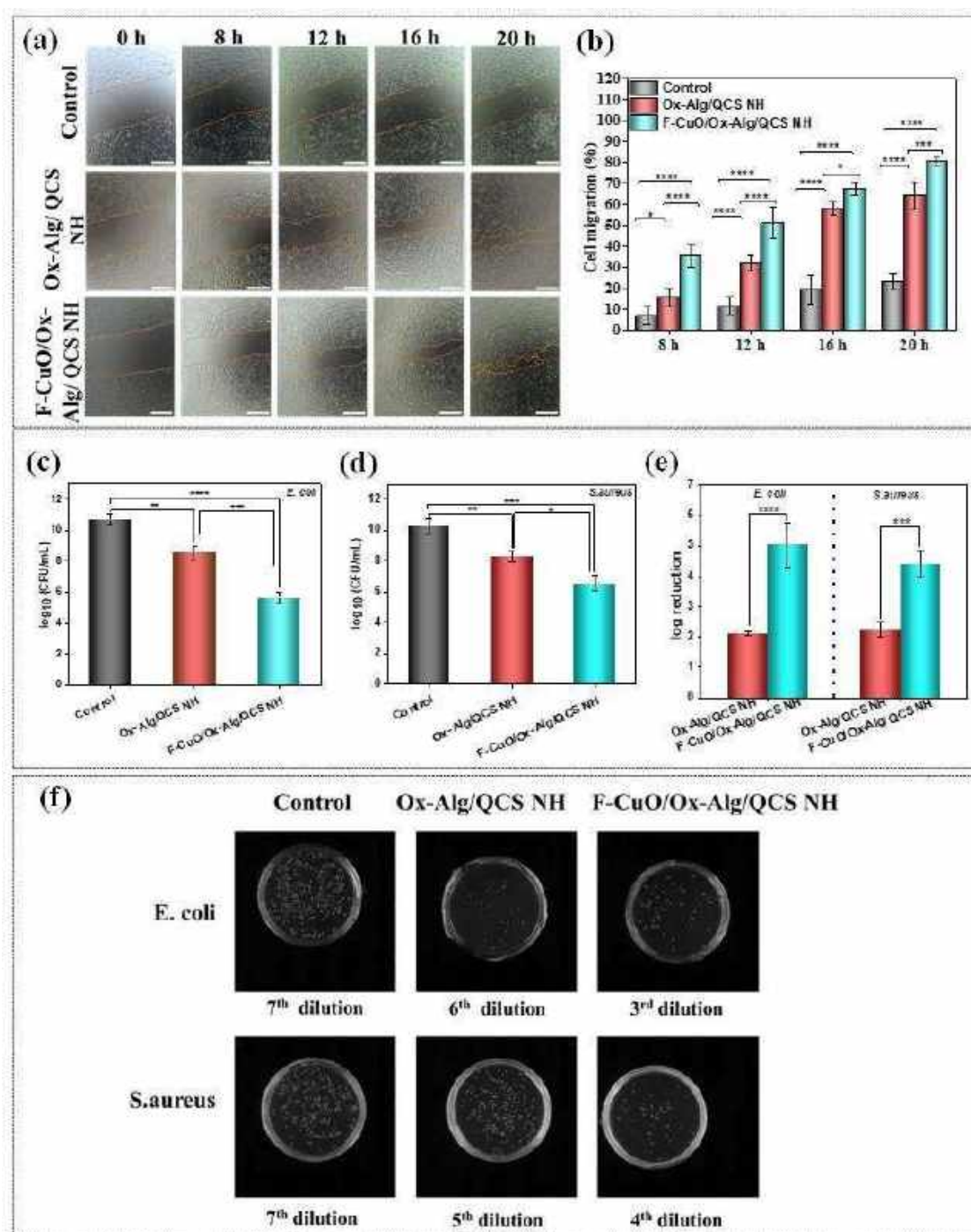


Figure 2- 8: (a) Micrographs of in vitro wound closure. The scale bar of all images is 200 μ m. (b) Wound closure rate of endothelial cells when treated with conditioned media of Ox-Alg/QCS NH and F-CuO/Ox-Alg/QCS NH. Control refers to fresh complete culture medium. Ordinary 2-way ANOVA with Tukey's multiple comparisons test was performed for b. (c-e) Antibacterial efficacy of F-CuO/Ox-Alg/QCS NH against (c) gram negative *E. coli* and (d)

gram positive *S. aureus*. (e) log reduction of both hydrogels compared to control against both gram positive and gram negative bacteria. (f) Photographs of agar plates of colonies of *E. coli* and *S. aureus*. Ordinary one-way ANOVA with Tukey's multiple comparisons test was performed for (c) and (d). Ordinary 2-way ANOVA with Sidak's multiple comparisons test was performed for (e). **** indicates $p < 0.0001$, *** indicates $p < 0.001$, ** indicates $p < 0.01$, * indicates $p < 0.05$ and ns indicates statistically non-significant.

2.2.13 *In vitro* antibacterial efficacy of F-CuO/Ox-Alg/ QCS NH

Antibacterial property is essential for the protection of the wound tissue from internal and external environmental bacterial infection. The antibacterial activity of both hydrogels was assessed using both *S. aureus* and *E. coli*. *E. coli* and *S. aureus* were chosen as representative strains for Gram-negative and Gram-positive bacteria, respectively, which can have different reactions against antibacterial therapies owing to significant differences in their cell wall structure[55-57]. Both these strains are well-known opportunistic pathogens responsible for several infections around the globe every year. Moreover, drug-resistant strains of both species have been identified in several parts of the world, highlighting the need for affordable, non-conventional antibacterial strategies to fight these infections. When the bacteria were treated with hydrogels for 4 h at 37 °C, both hydrogel groups showed an exceptional killing ratio (> 99%) for *E. coli* and *S. aureus* (Figure 2- 8 (c, d), & 8f). These results indicate the excellent inherent antibacterial properties of the hydrogels. After incubation of 4 h, \log_{10} CFU/mL of F-CuO/Ox-Alg/ QCS NH treated *E. coli* cells is 5.6 ± 0.3 (\approx log reduction 5 compared to the control group), whereas 8.5 ± 0.4 (\approx 2 log reduction compared to the control group) for Ox-Alg/ QCS NH treatment and 10.6 ± 0.37 for the control group (untreated group) (Figure 2- 8 (c, e)). A similar trend was also observed for *S. aureus* cells where \log_{10} CFU/mL for F-CuO/Ox-Alg/ QCS NH treated *S. aureus* cells is 6.0 ± 0.8 (\approx 4 log reduction), whereas 8.2 ± 0.3

(≈ 2 log reduction) and 10.4 ± 0.4 for Ox-Alg/ QCS NH treating and control group (untreated group), respectively (Figure 2- 8 (d, e)). There is significant statistical difference in the log reduction compared to the control group (untreated group) between the F-CuO/Ox-Alg/ QCS NH and Ox-Alg/ QCS NH for both the bacteria (for *E. coli*, $p < 0.0001$ and *S. aureus*, $p < 0.001$).

Positive-charged quaternary ammonium and amino groups of QCS could potentially damage the walls of the bacteria, leading to the release of intracellular fluids by electrostatic adherence with the cytoderm of bacteria[58]. On the other hand, the antibacterial activity of F-CuO nanomaterials can be associated with the generation of reactive oxygen species (ROS), the release of Cu^{2+} ions, copper-mediated protein activity imbalance, and the diffusion ability of the reactant molecules. According to the literature, CuO nanomaterials generate large amounts of ROS, leading to oxidative stress and death in bacterial cells[20, 54]. Therefore, F-CuO/Ox-Alg/ QCS NH has good antibacterial properties due to the combining effect of chitosan and F-CuO nanosheets.

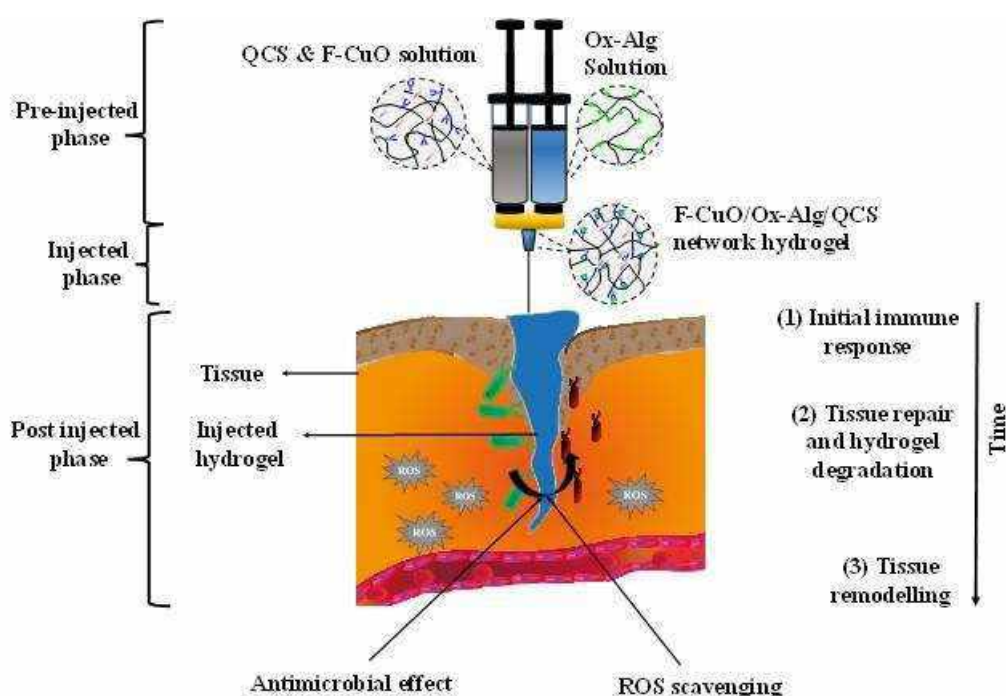
2.3 Discussion

There are several clinical needs that can benefit from self-healing hydrogels, which have thus received increasing interest in the biomaterials community. Specifically, hydrogels with multifunctional properties are in much demand to develop a multi-pronged strategy to address the needs for effective treatments. Among various needs, chronic wounds affect millions worldwide. The treatment of wounds, internal or external, is a critical clinical challenge, particularly in diabetic and immunocompromised patients. Typically, hemostasis, inflammation, proliferation, and remodeling phases are involved in wound healing[59]. Microbial infections and ROS are influential factors in the wound healing process that can delay each healing phase, resulting in functionally and structurally inadequate results[60].

Localized administration of antimicrobial agents at the exposed wound site is essential to treat chronic, infected wounds. In this study, the F-CuO embedded injectable hydrogel with quick gelation time was developed and was shown to exhibit broad spectrum antibacterial activity with pro-wound healing ability *in vitro*. F-CuO/Ox-Alg/ QCS NH showed tissue-like rheological properties and excellent self-healing properties, which can prolong the functionality of the hydrogel and support tissue remodeling. The potent antioxidant activity of F-CuO/Ox-Alg/ QCS NH can scavenge free radicals from the wound site and accelerate the healing process. Excellent cytocompatibility and blood compatibility of the developed F-CuO/Ox-Alg/ QCS NH can facilitate tissue remodeling. Scheme 2- 2 summarizes the potential application of the nanomaterial-embedded multi-biofunctional injectable hydrogel to promote wound healing.

Notably, our formulation of the injectable nanocomposite hydrogel laden with bioligand-functionalized nanomaterials offers a distinctive and attractive combination of properties compared to other hydrogels reported in the literature. We compiled key attributes of recently developed injectable hydrogels reported in the literature and key results of this investigation in Table 4- 1. In contrast to the studies reported by our group and others, the advantages of the system developed here are obvious owing to the unique combination of its properties that can be achieved by incorporating a surface-modified bioactive nanofiller. Unlike our previous study, here we have modified chitosan with GTMAC, which resulted in two benefits: (a) increased solubility of the chitosan in neutral pH or water to prepare the hydrogel, and (b) increased antibacterial activity of the hydrogel network due to the positive charge of trimethyl ammonium of the substituted GTMAC. Furthermore, while we used the double network crosslinking technique by introducing Schiff base crosslinking chemistry (covalent) and Fe^{2+} ionic crosslinking in the earlier work, here we proposed a novel surface engineering strategy of nanomaterials with a bioligand that can participate in our crosslinking system with the

prepolymer of the hydrogel system. Our results indicate that the modification of nanomaterials with the bioligand decreased the cytotoxicity. Most importantly, modifying nanomaterials with bioligands and our crosslinking engineering of hydrogel formation synergistically increase the dispersion of the nanomaterials in the prepolymer solution, and the hydrogel than unmodified nanomaterials (i.e., conventional physical loading). Consequently, the resultant nanocomposite exhibited synergistic benefits of the modified chitosan and CuO-based nanomaterials on cell response for wound healing and antibacterial activity. It is to be noted that the surface modification strategy demonstrated herein is not limited to CuO and can be adapted for other metal/metal oxide nanofillers to generate a library of nanocomposites with tailored attributes for a wide spectrum of biomedical applications. The findings of this work establish a promising multifunctional biomaterial formulation which will require further validation in animal models to establish the biomedical efficacy toward developing treatments for specific clinical needs.



Scheme 2- 2: Schematic illustration of the application of injectable F-CuO/Ox-Alg/QCS hydrogel with antibacterial and antioxidant properties to promote tissue remodeling.

Table 4- 1: Comparison of the properties of the developed F-CuO/Ox-Alg/QCS NH with other gels reported in the literature

Materials	Gelation time (sec)	Injectability ('I') & Self-healing ('S')	Storage modulus (G') (Pa/ kPa)	Blood compatibility ('B'), DPPH scavenging ('D') & Antibacterial property ('AB')	Applications	Ref
Mangiferin liposomes, Four-arm-PEG-SH and AgNO ₃	NA	^I yes ^S NA	NA	^B NA ^D NA ^{AB} Yes	Drug release, Skin flap regeneration	[61]
<i>N</i> -(2-hydroxypropyl)-3 trimethylammonium chitosan chloride (HTCC) and polydextran aldehyde	40 to 12	^I yes ^S NA	782 ± 137 Pa	^B NA ^D NA ^{AB} yes	Wound healing	[62]
Oxidized alginate & gelatine and bioactive glass	180 to 1500	^I NA ^S NA	NA	^B NA ^D NA ^{AB} NA	Bone regeneration	[63]
oxidized chondroitin sulfate (OCS) & gelatin (Gel) and bioactive glass nanoparticles	640 to 10	^I yes ^S NA	≈ 35 Pa	^B NA ^D NA ^{AB} NA	Bone regeneration	[64]
guar gum and N,Ocarboxymethyl chitosan	60 to 32	^I yes ^S yes	1611 Pa	^B Yes ^D NA ^{AB} NA	Drug delivery	[37]
oxidized hyaluronic acid (OHA), Gelatin and Fe ³⁺	≈ 54	^I yes ^S yes	535 kPa	^B yes ^D NA ^{AB} yes (Not good)	Wound healing	[65]
Oxidized chondroitin sulfate (OCS), carboxymethyl chitosan (CMC), ε-poly-L-lysine, selenium nanoparticles	38 to 250	^I yes ^S yes	≈ 300Pa	^B yes ^D yes ^{AB} yes	Diabetic Wound healing	[66]
Hyperbranched poly(β-amino ester)-tetraaniline (PBAE-TA) &	400 to 50	^I yes ^S NA	≈ 200 to 900 Pa	^B NA ^D NA ^{AB} NA	To promote diabetic wound healing	[67]

thiolated hyaluronic acid (HA-SH), vanillin-grafted gelatin (Geln-Van)							
Quaternized chitosan (QCS) and benzaldehyde-terminated Pluronic®F127 (PF127-CHO)	≈ 60 to 90	I ^{yes} S ^{yes}	22 kPa to 53 kPa	B ^{yes} D ^{yes} AB ^{yes (not good)}	Joint skin wound healing	[58]	
oxidized alginate and carboxymethyl chitosan and keratin nanoparticles	216	I ^{yes} S ^{NA}	≈ 403 Pa	B ^{NA} D ^{yes} AB ^{NA}	Wound repair	[68]	
Furan-Sodium Alginate , bis-maleimide- Polyethylene Glycol ,Copper doped Bioactive Glass	300	I ^{yes} S ^{NA}	NA	B ^{NA} D ^{NA} AB ^{NA}	Photothermal treatment for tumor related bone defects	[69]	
Acrylic acid-modified chitosan (aCS), aldehyde-alginate (aAlg), adipic acid dihydrazide and Fe ²⁺	13 to 20	I ^{yes} S ^{yes}	4486 ± 113 Pa	B ^{NA} D ^{NA} AB ^{NA}	Used as a minimally- invasive delivery platform	[13]	
F-CuO nanosheet, Oxidized Alginate, and Quarternized chitosan	≈ 15 to 20	I ^{yes} S ^{yes}	1463 ± 150 Pa	B ^{yes} D ^{yes} AB ^{yes}	Wound healing and biomedical application	Present work	

2.4 Conclusion

In this work, we proposed a generalized easy approach for surface modification of nanomaterials with a bioligand and developed a degradable polysaccharide-based injectable hydrogel that is shown to be multi-functional, including self-healing, flexible, and antibacterial for biomedical applications. Specifically, bioligand-modified CuO nanosheets were employed to modify the properties of the hydrogel. The injectable hydrogels exhibited rapid self-healing behavior owing to the dynamic Schiff base crosslinking chemistry. These F-CuO/Ox-Alg/ QCS NH or Ox-Alg/ QCS NH exhibited tunable gelation time, good self-healing ability, steady rheological property similar to soft human tissues, good degradation profile, cytocompatibility, good blood compatibility, free radical scavenging capacity, and inherent antibacterial property, which could effectively enhance the wound healing process. These results suggest that the degradable and injectable self-healing hydrogels with bioactive properties developed here are promising biomaterials for clinical applications.

2.5 References

1. Yu, L. and J. Ding, *Injectable hydrogels as unique biomedical materials*. Chemical Society Reviews, 2008. **37**(8): p. 1473-1481.
2. Marquardt, L.M. and S.C. Heilshorn, *Design of injectable materials to improve stem cell transplantation*. Current stem cell reports, 2016. **2**: p. 207-220.
3. Guvendiren, M., H.D. Lu, and J.A. Burdick, *Shear-thinning hydrogels for biomedical applications*. Soft matter, 2012. **8**(2): p. 260-272.
4. Lee, J.H., *Injectable hydrogels delivering therapeutic agents for disease treatment and tissue engineering*. Biomaterials research, 2018. **22**(1): p. 27.
5. Uman, S., A. Dhand, and J.A. Burdick, *Recent advances in shear-thinning and self-healing hydrogels for biomedical applications*. Journal of Applied Polymer Science, 2020. **137**(25): p. 48668.
6. Negm, N.A., et al., *Advancement on modification of chitosan biopolymer and its potential applications*. International journal of biological macromolecules, 2020. **152**: p. 681-702.
7. Ashkani-Esfahani, S., et al., *Glucosamine enhances tissue regeneration in the process of wound healing in rats as animal model: a stereological study*. J Cytol Histol, 2012. **3**(1): p. 150.
8. Singh, R., K. Shitiz, and A. Singh, *Chitin and chitosan: biopolymers for wound management*. International wound journal, 2017. **14**(6): p. 1276-1289.
9. Feng, L., et al., *Molecular weight distribution, rheological property and structural changes of sodium alginate induced by ultrasound*. Ultrasonics sonochemistry, 2017. **34**: p. 609-615.
10. Cofelice, M., et al., *Effect of the xanthan gum on the rheological properties of alginate hydrogels*. Food Hydrocolloids, 2023. **142**: p. 108768.
11. Li, Y., et al., *Multifunctional hydrogels prepared by dual ion cross-linking for chronic wound healing*. ACS Applied Materials Interfaces, 2017. **9**(19): p. 16054-16062.
12. Thomas, A., K. Harding, and K. Moore, *Alginates from wound dressings activate human macrophages to secrete tumour necrosis factor- α* . Biomaterials, 2000. **21**(17): p. 1797-1802.
13. Mondal, P. and K. Chatterjee, *Injectable and self-healing double network polysaccharide hydrogel as a minimally-invasive delivery platform*. Carbohydrate Polymers, 2022. **291**: p. 119585.
14. Gopal, A., et al., *Chitosan-based copper nanocomposite accelerates healing in excision wound model in rats*. European journal of pharmacology, 2014. **731**: p. 8-19.
15. Borkow, G., et al., *Molecular mechanisms of enhanced wound healing by copper oxide-impregnated dressings*. Wound repair regeneration, 2010. **18**(2): p. 266-275.

16. Li, F., et al., *Analysis of copper nanoparticles toxicity based on a stress-responsive bacterial biosensor array*. Nanoscale, 2013. **5**(2): p. 653-662.
17. Mohandas, A., et al., *Chitosan–hyaluronic acid/VEGF loaded fibrin nanoparticles composite sponges for enhancing angiogenesis in wounds*. Colloids Surfaces B: Biointerfaces, 2015. **127**: p. 105-113.
18. Meng, Y., et al., *Polarity control of DNA adsorption enabling the surface functionalization of CuO nanozymes for targeted tumor therapy*. Materials Horizons, 2021. **8**(3): p. 972-986.
19. Sathiyavimal, S., et al., *Bio-functionalized copper oxide/chitosan nanocomposite using Sida cordifolia and their efficient properties of antibacterial, anticancer activity against on breast and lung cancer cell lines*. Environmental Research, 2023. **218**: p. 114986.
20. Gilbertson, L.M., et al., *Shape-dependent surface reactivity and antimicrobial activity of nano-cupric oxide*. Environmental science technology, 2016. **50**(7): p. 3975-3984.
21. Zhu, D., et al., *Intriguingly high thermal conductivity increment for CuO nanowires contained nanofluids with low viscosity*. scientific reports, 2018. **8**(1): p. 5282.
22. Ajamein, H. and M. Haghighi, *On the microwave enhanced combustion synthesis of CuO–ZnO–Al₂O₃ nanocatalyst used in methanol steam reforming for fuel cell grade hydrogen production: Effect of microwave irradiation and fuel ratio*. Energy Conversion Management, 2016. **118**: p. 231-242.
23. Fang, J. and Y. Xuan, *Investigation of optical absorption and photothermal conversion characteristics of binary CuO/ZnO nanofluids*. RSC advances, 2017. **7**(88): p. 56023-56033.
24. Faisal, M., et al., *Ethanol chemi-sensor: Evaluation of structural, optical and sensing properties of CuO nanosheets*. Materials Letters, 2011. **65**(9): p. 1400-1403.
25. Kahouli, M., et al., *Structural and optical properties of ZnO nanoparticles prepared by direct precipitation method*. Superlattices Microstructures, 2015. **85**: p. 7-23.
26. Srivastava, V., D. Gusain, and Y.C. Sharma, *Synthesis, characterization and application of zinc oxide nanoparticles (n-ZnO)*. Ceramics International, 2013. **39**(8): p. 9803-9808.
27. Jaramillo, A., et al., *Estimation of the surface interaction mechanism of ZnO nanoparticles modified with organosilane groups by Raman Spectroscopy*. Ceramics International, 2017. **43**(15): p. 11838-11847.
28. Cho, J., et al., *Synthesis and physicochemical and dynamic mechanical properties of a water-soluble chitosan derivative as a biomaterial*. Biomacromolecules, 2006. **7**(10): p. 2845-2855.
29. Lim, S.-H. and S.M. Hudson, *Synthesis and antimicrobial activity of a water-soluble chitosan derivative with a fiber-reactive group*. Carbohydrate research, 2004. **339**(2): p. 313-319.

30. Xiao, B., et al., *Synthesis and characterization of N-(2-hydroxy) propyl-3-trimethyl ammonium chitosan chloride for potential application in gene delivery*. Colloids Surfaces B: Biointerfaces, 2012. **91**: p. 168-174.
31. Emami, Z., et al., *Controlling alginate oxidation conditions for making alginate-gelatin hydrogels*. Carbohydrate polymers, 2018. **198**: p. 509-517.
32. Salem, D.M., M.A. Sallam, and T.N. Youssef, *Synthesis of compounds having antimicrobial activity from alginate*. Bioorganic chemistry, 2019. **87**: p. 103-111.
33. Li, H., et al., *Injectable, self-healing, antibacterial, and hemostatic N, O-carboxymethyl chitosan/oxidized chondroitin sulfate composite hydrogel for wound dressing*. Materials Science Engineering: C, 2021. **118**: p. 111324.
34. Shi, J., et al., *Schiff based injectable hydrogel for in situ pH-triggered delivery of doxorubicin for breast tumor treatment*. Polymer Chemistry, 2014. **5**(21): p. 6180-6189.
35. Lu, X.-W., et al., *Substrate-independent, Schiff base interactions to fabricate lysine-functionalized surfaces with fibrinolytic activity*. Journal of materials chemistry B, 2016. **4**(8): p. 1458-1465.
36. Oh, S.H., et al., *In vitro and in vivo characteristics of PCL scaffolds with pore size gradient fabricated by a centrifugation method*. Biomaterials, 2007. **28**(9): p. 1664-1671.
37. Pandit, A.H., et al., *Injectable, self-healing, and biocompatible N, O-carboxymethyl chitosan/multialdehyde guar gum hydrogels for sustained anticancer drug delivery*. Biomacromolecules, 2021. **22**(9): p. 3731-3745.
38. Han, J., T. Lei, and Q. Wu, *High-water-content mouldable polyvinyl alcohol-borax hydrogels reinforced by well-dispersed cellulose nanoparticles: Dynamic rheological properties and hydrogel formation mechanism*. Carbohydrate polymers, 2014. **102**: p. 306-316.
39. Wang, Y. and L. Chen, *Impacts of nanowhisker on formation kinetics and properties of all-cellulose composite gels*. Carbohydrate polymers, 2011. **83**(4): p. 1937-1946.
40. Inoue, T. and K. Osaki, *Rheological properties of poly (vinyl alcohol)/sodium borate aqueous solutions*. Rheologica acta, 1993. **32**(6): p. 550-555.
41. Wu, M., et al., *Injectable and self-healing nanocomposite hydrogels with ultrasensitive pH-responsiveness and tunable mechanical properties: implications for controlled drug delivery*. Biomacromolecules, 2020. **21**(6): p. 2409-2420.
42. Zhao, X., et al., *Injectable antistiffening and high-Strength bioactive hydrogels with a wet adhesion and rapid gelling process to promote sutureless wound closure and scar-free repair of infectious wounds*. ACS nano, 2023. **17**(21): p. 22015-22034.
43. Mondal, P., I. Chakraborty, and K. Chatterjee, *Injectable adhesive hydrogels for soft tissue reconstruction: a materials chemistry perspective*. The Chemical Record, 2022. **22**(11): p. e202200155.

44. Sharma, P.K., S. Taneja, and Y. Singh, *Hydrazone-linkage-based self-healing and injectable xanthan–poly (ethylene glycol) hydrogels for controlled drug release and 3D cell culture*. ACS applied materials interfaces, 2018. **10**(37): p. 30936-30945.
45. Rajput, M., et al., *Light-based 3D bioprinting of bone tissue scaffolds with tunable mechanical properties and architecture from photocurable silk fibroin*. International Journal of Biological Macromolecules, 2022. **202**: p. 644-656.
46. Kilmartin, P., et al., *Free radical scavenging and antioxidant properties of conducting polymers examined using EPR and NMR spectroscopies*. Synthetic metals, 2005. **153**(1-3): p. 153-156.
47. Joshi, R., et al., *Free radical scavenging behavior of folic acid: evidence for possible antioxidant activity*. Free Radical Biology Medicine, 2001. **30**(12): p. 1390-1399.
48. Nilawar, S., M. Bs, and K. Chatterjee, *Nanoceria-decorated graphene nanosheets enhance mechanical properties and bioactivity of a degradable polyurethane for biomedical applications*. Journal of Polymers the Environment, 2023. **31**(7): p. 2941-2955.
49. Muzzarelli, R.A., *Chitins and chitosans for the repair of wounded skin, nerve, cartilage and bone*. Carbohydrate polymers, 2009. **76**(2): p. 167-182.
50. Gonçalves, R.C., et al., *Strategies for re-vascularization and promotion of angiogenesis in trauma and disease*. Biomaterials, 2021. **269**: p. 120628.
51. Shanmugapriya, K., et al., *Fabrication of multifunctional chitosan-based nanocomposite film with rapid healing and antibacterial effect for wound management*. International journal of biological macromolecules, 2018. **118**: p. 1713-1725.
52. Kornblatt, A.P., V.G. Nicoletti, and A. Travaglia, *The neglected role of copper ions in wound healing*. Journal of inorganic biochemistry, 2016. **161**: p. 1-8.
53. Ahmed, S.B., et al., *Investigation of the antimicrobial activity and hematological pattern of nano-chitosan and its nano-copper composite*. Scientific Reports, 2021. **11**(1): p. 9540.
54. Karthikeyan, C., et al., *Biocidal (bacterial and cancer cells) activities of chitosan/CuO nanomaterial, synthesized via a green process*. Carbohydrate Polymers, 2021. **259**: p. 117762.
55. Salton, M., *Studies of the bacterial cell wall: IV. The composition of the cell walls of some gram-positive and gram-negative bacteria*. Biochimica et biophysica acta, 1953. **10**: p. 512-523.
56. Huang, K.C., et al., *Cell shape and cell-wall organization in Gram-negative bacteria*. Proceedings of the National Academy of Sciences, 2008. **105**(49): p. 19282-19287.
57. Pasquina-Lemonche, L., et al., *The architecture of the Gram-positive bacterial cell wall*. Nature, 2020. **582**(7811): p. 294-297.

58. Qu, J., et al., *Antibacterial adhesive injectable hydrogels with rapid self-healing, extensibility and compressibility as wound dressing for joints skin wound healing*. Biomaterials, 2018. **183**: p. 185-199.
59. Shariati, A., et al., *Wound healing properties and antimicrobial activity of platelet-derived biomaterials*. Scientific Reports, 2020. **10**(1): p. 1032.
60. Dev, S.K., et al., *Antimicrobial, anti-inflammatory and wound healing activity of polyherbal formulation*. Biomedicine Pharmacotherapy, 2019. **111**: p. 555-567.
61. Mao, X., et al., *Self-healing and injectable hydrogel for matching skin flap regeneration*. Advanced science, 2019. **6**(3): p. 1801555.
62. Hoque, J., et al., *Biocompatible injectable hydrogel with potent wound healing and antibacterial properties*. Molecular pharmaceutics, 2017. **14**(4): p. 1218-1230.
63. Sarker, B., et al., *Designing porous bone tissue engineering scaffolds with enhanced mechanical properties from composite hydrogels composed of modified alginate, gelatin, and bioactive glass*. ACS Biomaterials Science Engineering, 2016. **2**(12): p. 2240-2254.
64. Zhou, L., et al., *Hybrid gelatin/oxidized chondroitin sulfate hydrogels incorporating bioactive glass nanoparticles with enhanced mechanical properties, mineralization, and osteogenic differentiation*. Bioactive materials, 2021. **6**(3): p. 890-904.
65. Yuan, Y., S. Shen, and D. Fan, *A physicochemical double cross-linked multifunctional hydrogel for dynamic burn wound healing: shape adaptability, injectable self-healing property and enhanced adhesion*. Biomaterials, 2021. **276**: p. 120838.
66. Zhao, N. and W. Yuan, *Self-healing and shape-adaptive nanocomposite hydrogels with anti-inflammatory, antioxidant, antibacterial activities and hemostasis for real-time visual regeneration of diabetic wounds*. Composites Part B: Engineering, 2023. **262**: p. 110819.
67. Jin, X., et al., *Injectable hypoxia-induced conductive hydrogel to promote diabetic wound healing*. ACS Applied Materials Interfaces, 2020. **12**(51): p. 56681-56691.
68. Ma, L., et al., *Injectable oxidized alginate/carboxymethyl chitosan hydrogels functionalized with nanoparticles for wound repair*. Carbohydrate Polymers, 2022. **293**: p. 119733.
69. Yang, Z., et al., *Degradable photothermal bioactive glass composite hydrogel for the sequential treatment of tumor-related bone defects: From anti-tumor to repairing bone defects*. Chemical Engineering Journal, 2021. **419**: p. 129520.

Research 2

Bi-directional shape morphing in 4D-bioprinted hydrogels on a single stimulation

5.1 Introduction

4D-printed, shape-morphing architectures are in great demand for advanced biomedical technologies, including but not limited to soft biohybrid robots[1, 2], tissue engineering[3, 4], drug delivery[5, 6], medical devices[7, 8], and biosensors[9]. This has spurred the development of responsive materials and design strategies that can enable exquisite shape changes on exogenous stimulation[10]. However, the limited availability of responsive materials that respond to a mild mode of stimulation and demonstrate biocompatibility presents a critical impediment to their adoption in biomedical applications. In the case of non-responsive hydrogels, various humidity-responsive mechanisms (multi-component assembly[11-13], photocrosslinking gradient[14-16], dehydration gradient[17], anisotropic fillers[18], degradation gradient[19, 20], multi-component assembly + photocrosslinking gradient[14], multi-component assembly + dehydration gradient[21], photocrosslinking gradient + dehydration gradient[22, 23]) have been proposed to guide the as-printed two-dimensional (2D)/ three-dimensional (3D) construct to a pre-defined, target shape[24]. Despite this progress, the current actuation mechanisms are only capable of predetermined uni-directional shape morphing and require distinct triggers to execute multiple shape transformations, which can be particularly challenging in a clinical setting for implantable devices.

Applications that require multiple triggerable actuations, such as hydrogel-based deployable devices (shape miniaturization for minimally invasive implantation and subsequent shape recovery at the target site) have traditionally depended on reversible changes triggered by the application and withdrawal of stimuli, such as hydration and dehydration, heating and cooling, increase and decrease in pH, or the addition and removal of ions. Alternatively, multiple stimuli, including temperature, pH, chemical, electric, and magnetic fields, may be employed to elicit the two distinct shape transformations (refer Table 3- 2). Despite their suitability for specific target applications, the aforementioned stimuli present several disadvantages that

preclude their use in numerous *in vivo* applications. For instance, exposure to temperatures exceeding the normal physiological temperature (37°C) can engender off-target repercussions on the adjacent tissue. Further, the use of magnetic stimuli necessitates bulky instrumentation and can potentially hinder standard medical imaging modalities. *In vivo* applications of pH stimuli are constrained to regions that match the hydrogel's pH-responsive interval. Chemical stimuli, on the other hand, necessitate material contact and present logistical challenges for spatial deployment and control within the body. Depending on the conditions of administration, temperature, pH, and chemical-based stimuli run the risk of inducing cytotoxic effects and could compromise cell viability within the bioprinted construct. Moreover, the application of a secondary trigger *in vivo* also poses a significant challenge in clinical settings. Hence, there is a pressing need to design smart hydrogel-based systems that are biocompatible, dynamically deliverable, and do not need any additional triggers to attain their final conformation once implanted in the body in their maximal miniaturized state. Despite a few notable examples of a single stimulation leading to multi-step shape transformations, the underlying mechanisms are material-specific, with no broad, generalizable principles proposed to explain this phenomenon[25, 26].

To address these limitations, we aimed to develop a novel 4D (bio)printing approach that employs biocompatible and versatile biomaterial ink design to encode two opposing shape transformations that proceed sequentially through the application of only a single initial mild stimulation (water uptake). To realize this, we conceived an innovative 4D shape-morphing strategy in which the activation of the second actuation mechanism occurs as a direct consequence of the conditions established upon completion of the first actuation mechanism, eliminating the need for any secondary external stimulation. We implemented this concept by 3D printing semi-IPN hydrogels, which exhibit a gradient in photocrosslinking density and undergo anisotropic water uptake when immersed in water. This differential water swelling not

only triggers the first shape transformation but also sets up an internal osmolarity gradient that drives the second shape transformation in the opposite direction. Our proposed 4D mechanism is material agnostic and can be realized through a multitude of semi-IPN compositions, thereby broadening its scope of application. Water, being ubiquitous in the human body, is well-suited for biomedical applications, does not present related cytocompatibility or toxicity issues, and hence was chosen as the stimuli for our 4D-(bio)printed hydrogels. We describe how this unique shape-morphing behavior can be leveraged to fabricate pre-programmed, deployable hydrogel devices that are not realizable via current approaches. By achieving multi-step shape transformations on a single stimulation, our shape-morphing strategy holds significant promise for automating complex functions by minimizing external interventions and can facilitate the development of smart solutions for outstanding biomedical challenges.

5.2 Methods

5.2.1 Synthesis of methacrylated derivatives of carboxymethyl cellulose (CMC-MA), chitosan (CS-MA), poly(ethylene glycol) (PEGDMA), alginate (Alg-MA), and κ -carrageenan (κ -CA-MA)

CMC-MA, CS-MA, PEGDMA, Alg-MA, and K-CA-MA were synthesized as described in section 1.1.5. Then, To confirm the chemical modification of methacrylation of the synthesized polymers, FTIR and ^1H NMR analysis were performed as described in sections 1.1.8.1 and 1.1.8.2, respectively.

5.2.2 Preparation of inks/precursor solutions of CMC-MA/MC, CS-MA/PEGDMA/MC, Alg-MA/MC, κ -CA-MA/MC

In order to prepare precursor solutions, the methacrylated polymers were solubilized in 3 mL of deionized water under continuous stirring (refer Table 3- 1). Subsequently, the temperature

was gradually increased to a maximum of 60 °C, and MC was added to the mixture and mixed thoroughly until a homogeneous solution was obtained. A fixed volume of 3% (w/v) LAP solution was then incorporated into the mixture. The resulting solution was loaded into a cartridge and maintained at 4 °C for a duration of 45 minutes, allowing for the complete hydration of MC. The cartridge was then kept at ambient temperature (~25 °C) before initiating the printing processes.

Table 3- 1: Ink compositions

Ink	Photocrosslinkable polymer(s) (w/v)	Methyl cellulose (w/v)	Volume of 3% LAP solution (μL) added in 3 ml of ink
CMC-MA/MC	4% CMC-MA	6%	100
CS- MA/PEGDMA/MC	1% CS-MA + 10 % PEGDMA	6%	300
Alg-MA/MC	2% Alg-MA	6%	100
κ-CA-MA/MC	4% κ -CA-MA	6%	150

5.2.3 Rheology measurements

The rheological properties of CMC-MA/MC and CS-MA/PEGDMA/MC inks were assessed using Anton Paar MCR 302 rheometers equipped with Peltier elements for temperature control. A parallel plate geometry (diameter: 25 mm) with a 1 mm gap size was employed for all

experiments. Four tests were conducted for each ink at 25 °C to determine the key rheological properties necessary for various stages of 3D printing.

First, the shear thinning behavior of the inks was assessed using a shear rate sweep by varying the shear rate from 0.1 to 100 s⁻¹. Second, the ability of the inks to quickly recover their solid-like behavior following extrusion was evaluated using the three interval-time-thixotropy (3ITT) recovery test. This was performed under three shearing intervals: a low shear rate of 1 s⁻¹ for 150 seconds, a high shear rate of 100 s⁻¹ for 150 seconds, and a low shear rate of 1 s⁻¹ for 150 seconds to simulate the printing process.

Third, an amplitude sweep was conducted by varying the shear strain from 0.1 to 800% while keeping the angular frequency constant at 10 rad/s to identify the linear viscoelastic region (LVR) and the shear-yielding points at which the inks exhibited fluid-like behavior. Finally, a frequency sweep was performed in the LVR, with angular frequency varying from 0.1 to 100 rad/s at 1% amplitude strain to quantify the storage (G') and loss moduli (G'') of the inks.

5.2.4 3D printing

Extrusion based 3D printing were used to print the construct as described in section 1.1.7.1. The printing parameters for all inks were described.

5.2.5 Bending angle measurements of 4D T-beam model constructs

In order to quantify the bending angle of a T-beam, we employ a vector-based approach, utilizing two distinct tangent vectors, **a** and **b**. Vector **a** is defined as a tangent vector originating from one end of the T-beam, oriented towards the direction of the beam's longitudinal axis, while vector **b** is defined as a tangent vector originating from the opposite end and directed away from the same axis (Figure 3- 1). The bending angle at a given time, t ,

is quantified as the net angle spanned by vector **a** with respect to vector **b** during the course of the beam's deformation, as illustrated in Figure 3- 1.

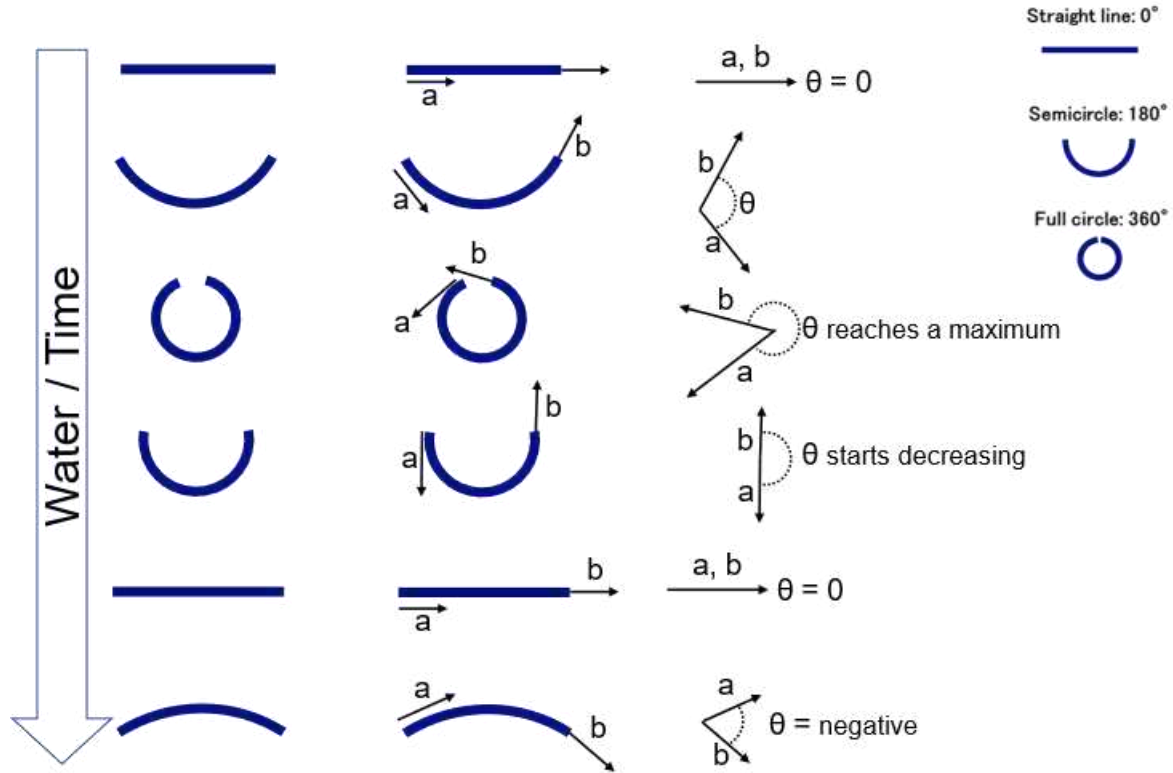


Figure 3- 1: Schematic illustration for the determination of the bending angle of the T-beams.

5.2.6 Characterizations of the printed construct

Additional properties relevant to biomedical applications, such as swelling behavior, degradation studies, and mechanical behavior, were also performed as described in sections 1.1.8.4, 1.1.18.5, and 1.1.8.7, respectively, of methodology section.

5.2.7 Water diffusion coefficient of CMC-MA/MC and CS-MA/PEGDMA/MC hydrogels

The water diffusion coefficients of CMC-MA/MC and CS-MA/PEGDMA/MC hydrogels were calculated to quantify the swelling kinetics. The fractional water swelling data (M_t/M_∞ ; M_t is the mass of water absorbed at time t , and M_∞ is the mass of water absorbed at equilibrium)

was plotted versus the square root of time to investigate the nature of transport mechanism (Fickian vs Case II diffusion). The regions ($17.3 < t^{1/2} < 24.5$ for CMC-MA/MC and $17.3 < t^{1/2} < 60$ for CS-MA/PEGDMA/MC) can be considered linear and the diffusion coefficients (D) were determined from the slope of the linear regions using the following formula[27]:

$$\frac{M_t}{M_\infty} = 4 \left(\frac{Dt}{\pi l^2} \right)^{1/2}$$

Where t is the time, and l ($= 1$ mm) is the average thickness of the cylindrical disc samples.

5.2.8 3D bioprinting

L929 mouse fibroblast cells were used in this study. Cells were cultured and expanded as described in section 1.1.9.

The CS-MA, CMC-MA, PEGDMA, and MC powders were UV sterilized in the biosafety cabinet, and the LAP solution was sterile-filtered before preparing the bioink. The CMC-MA/MC and CS-MA/PEGDMA/MC hydrogel precursor solutions were prepared in HG-DMEM and PBS solution, respectively, and stored under sterile conditions at 4°C for 30 minutes. L929 cells (3×10^6 cells/mL of solution) were then mixed with the hydrogel precursor solutions to prepare the cell-laden bioinks. The bioink was then loaded into a cartridge and extrusion printed (25-gauge needle) to produce cylindrical constructs (1 cm diameter, 1 mm height, 15% infill) for evaluating cytocompatibility. The constructs were photo-crosslinked for 3 minutes using 405 nm blue light from a distance of approximately 25 cm above the print bed. The cell-laden hydrogel constructs were cultured for up to 14 days in 24-well tissue culture plate wells containing 1 mL of medium, which was replenished every alternate day.

5.2.9 In vitro cytocompatibility of the bioprinted scaffolds

5.2.9.1 Alamar Blue assay

The metabolic activity of cells within a bioprinted scaffold was evaluated using the Alamar Blue assay (Resazurin reduction) at four time points (1, 4, 7, and 14 days) of culture. Prior to conducting the assay, the bioprinted scaffolds ($n = 3$) were transferred to new wells. Following this, the scaffolds were incubated in a culture medium containing 0.0015 mg/mL dye at 37 °C for 3 hours. Thereafter, 100 μ L of the medium for each sample was transferred into a 96-well plate, and the fluorescence intensity was measured using a microplate reader (Biotek) with 530 nm excitation and 600 nm emission filters. All measurements were performed in triplicate and presented as mean \pm standard deviation.

5.2.9.2 Live-Dead staining

The qualitative cell viability of the bioprinted scaffolds was assessed on days 1, 4, 7, and 14 after culture using the Live-Dead assay. Bioprinted scaffolds were washed with PBS and incubated in a cell culture medium containing 4 μ M Ethidium Homodimer-1 (EthD-1, Invitrogen) and 2 μ M Calcein acetoxymethylester (Calcein A/M, Invitrogen) to stain dead and live cells, respectively. After an hour of staining, hydrogels were washed twice with PBS and imaged using a confocal microscope (Leica SP8 Falcon, Leica Microsystems) in green and red excitation channels. The obtained images were processed using the LAS X software.

5.3 Results and discussion

5.3.1 Methacrylation of CMC, CS, PEG, Alg, and κ -CA

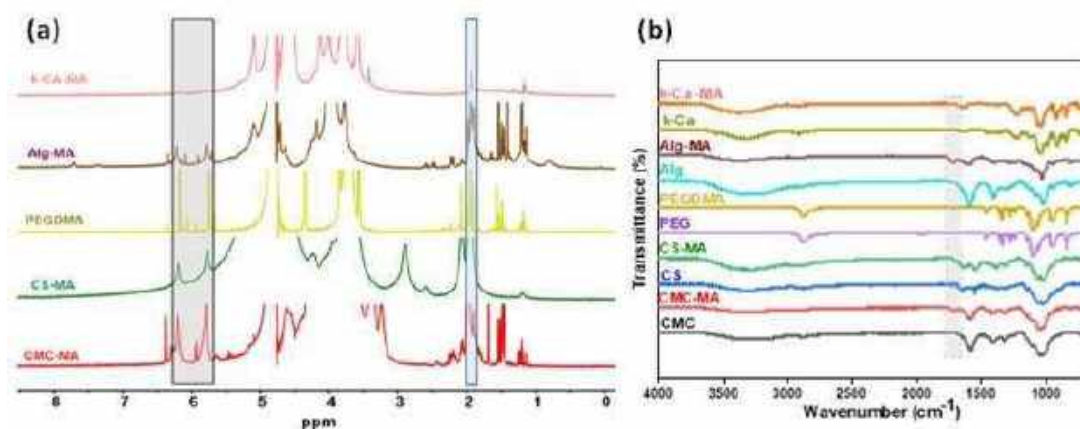


Figure 3- 2: (a) ^1H NMR spectra of methacrylated polymers (b) FTIR spectra of unmodified and methacrylated polymers.

CMC-MA, CS-MA, PEGDMA, Alg-MA, and κ -CA-MA were synthesized from precursor polymers, as illustrated in Figures 1- 1, 1- 2, 1- 3, 1- 4, and 1- 5, respectively. The successful methacrylation of CMC, CS, PEG, Alg, and κ -CA was confirmed by ^1H NMR and FTIR spectroscopy. We observed resonance peaks associated with methyl ($\delta = 1.9$ ppm) and vinyl ($\delta = 5.7$ and 6.1 ppm) groups in the ^1H NMR spectra of CMC-MA, CS-MA, PEGDMA, Alg-MA, and κ -CA-MA, which confirmed successful methacrylation (Figure 3- 2 a). Additionally, the FTIR spectra showed characteristic vibration bands for the $-(\text{C}=\text{O})\text{O}$ ester group (CMC-MA: 1716 cm^{-1} , CS-MA: 1707 cm^{-1} , PEGDMA: 1716 cm^{-1} , Alg-MA: 1716 cm^{-1} , κ -CA-MA: 1717 cm^{-1}) and the $=\text{C}-\text{H}$ bending due to alkene group (CMC-MA: 812 cm^{-1} , CS-MA: 814 cm^{-1}), which further confirmed successful methacrylation (Figure 3- 2 b).

5.3.2 Rheological behavior of CMC-MA/MC and CS-MA/PEGDMA/MC inks

5.3.2.1 Extrudability

The extrudability of an ink depends on pre-deposition parameters and is influenced by the shear rate. In order to investigate the extrudability of inks, shear rate sweep and thixotropy tests were performed. Dynamic viscosity measurements were performed by varying the shear rate from 0.1 to 100 s⁻¹. Both inks exhibit a decrease in viscosity with increasing shear rate, indicating shear-thinning properties within the tested range (Figure 3- 3 a). This behavior is attributed to the disentanglement and reorientation of polymer chains at high shear rates, which leads to a drop in viscosity. The shear-thinning properties of the inks enable them to flow easily through small nozzle diameters during extrusion-based printing.

To ensure that the ink recovers its original viscosity following a drop in viscosity during extrusion and forms a stable filament, three interval-time-thixotropy (3iTT) recovery tests were conducted to simulate the extrusion process. This test comprises three stages: a low shear rate of 1 s⁻¹ (to represent the resting stage), a high shear rate of 100 s⁻¹ (to represent the extrusion process), and a return to the original shear rate (to model the recovery process). During the resting stage, the inks maintained stable viscosity, while they experienced a sharp drop in viscosity at high shear rates. Finally, upon removal of high shear rate, the viscosity of the inks quickly recovered to values comparable to the initial stage, demonstrating excellent thixotropic properties of the inks (Figure 3- 3 b).

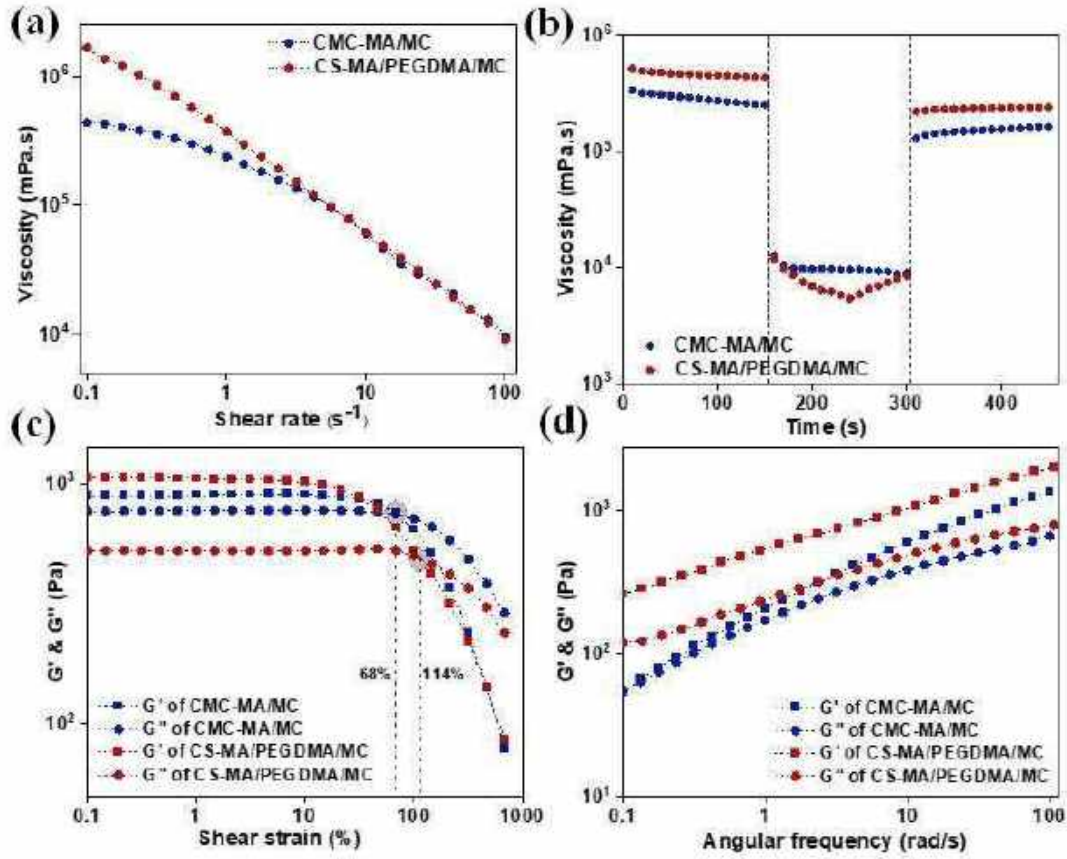


Figure 3- 3: Rheological properties of CMC-MA/MC and CS-MA/PEGDMA/MC precursor inks (a) Shear rate sweep (b) 3iTT recovery test (c) Amplitude sweep (d) Frequency sweep

5.3.2.2 Shape fidelity

To prevent the collapse or deformation of the printed layers, it is essential to optimize the viscoelastic properties of the inks. A solid-like viscoelastic ink with $\tan \delta < 1$ is desired to ensure the shape fidelity of the printed constructs. The viscoelastic nature of the inks is characterized by frequency and amplitude sweep tests. Frequency sweep tests were initially performed to investigate the dynamic viscoelasticity of the inks. Both inks exhibited gel-like behavior with $G' > G''$ and $\tan \delta < 1$ over the entire frequency range (Figure 3- 3 d). However, the modulus values had a strong positive frequency dependence, which is a characteristic of viscoelastic liquids[28].

Similarly, in the amplitude sweep test, both inks behaved like viscoelastic solids within the linear viscoelastic range (LVR), displaying a higher storage modulus (G') than loss modulus (G'') with nearly constant modulus values until 10% shear strain (Figure 3- 3 c). Due to the uncrosslinked nature of the inks, the storage and loss moduli of the inks are of the same order of magnitude. Upon exceeding a certain % strain, the inks exhibited a gel-sol transition, leading to a sharp drop in storage modulus, with G'' dominating G' . The yield stress, i.e., the stress at which the gel-sol transition occurs, for the CMC-MA/MC and CS-MA/PEGDMA/MC inks are 68% and 114% strain, respectively.

Taken together, the quasi-solid viscoelastic nature of the inks endows them with the ability to maintain their structural integrity post-printing and enables the fabrication of complex, high-resolution structures.

5.3.3 Sequential, Bi-directional Shape-Morphing Behavior in Single-Component Hydrogel

Herein, we report an innovative design strategy and actuation scheme for the 4D printing of shape-morphable and deployable hydrogels that can also be applied for bioprinting cell-laden scaffolds. Our 4D printing approach relies on the automated, sequential activation of different shape-morphing mechanisms using a single stimulus (water) to realize bi-directional shape-morphing in hydrogels. Owing to its cytocompatible nature, water uptake is well-suited as a trigger for biomedical applications and provides a simple, safe, and facile means of inducing shape changes even in the absence of an external power input or sophisticated interventions[24]. Our strategy for integrating distinct actuation mechanisms relies on graded semi-interpenetrating network (semi-IPN) hydrogels. The semi-IPN hydrogel system consists of two polymers, namely, an anisotropically photocrosslinked polymer backbone and a second physically entangled polymer network. The hydrogel precursor ink consists of an aqueous solution of methacrylated carboxymethyl cellulose (CMC-MA) (4% w/v), photoinitiator

(Lithium phenyl-2,4,6-trimethylbenzoylphosphinate or LAP) (0.1% w/v), and methyl cellulose (MC) (6% w/v). The presence of photocrosslinkable methacrylate moieties within CMC-MA (Figure 3- 2) enables the formation of chemically crosslinked hydrogels upon exposure to visible light in the presence of LAP. MC serves as a rheological aid and facilitates extrusion-based 3D printing by imparting extrudability and shape fidelity to the ink (Figure 3- 3)[29]. Various T-beam architectures are printed using this viscoelastic ink (Figure 3- 4 a, b) under ambient conditions and subsequently photocrosslinked using visible light to yield mechanically robust (Figure 3- 6 d, e), biocompatible hydrogel structures that readily swell in water.

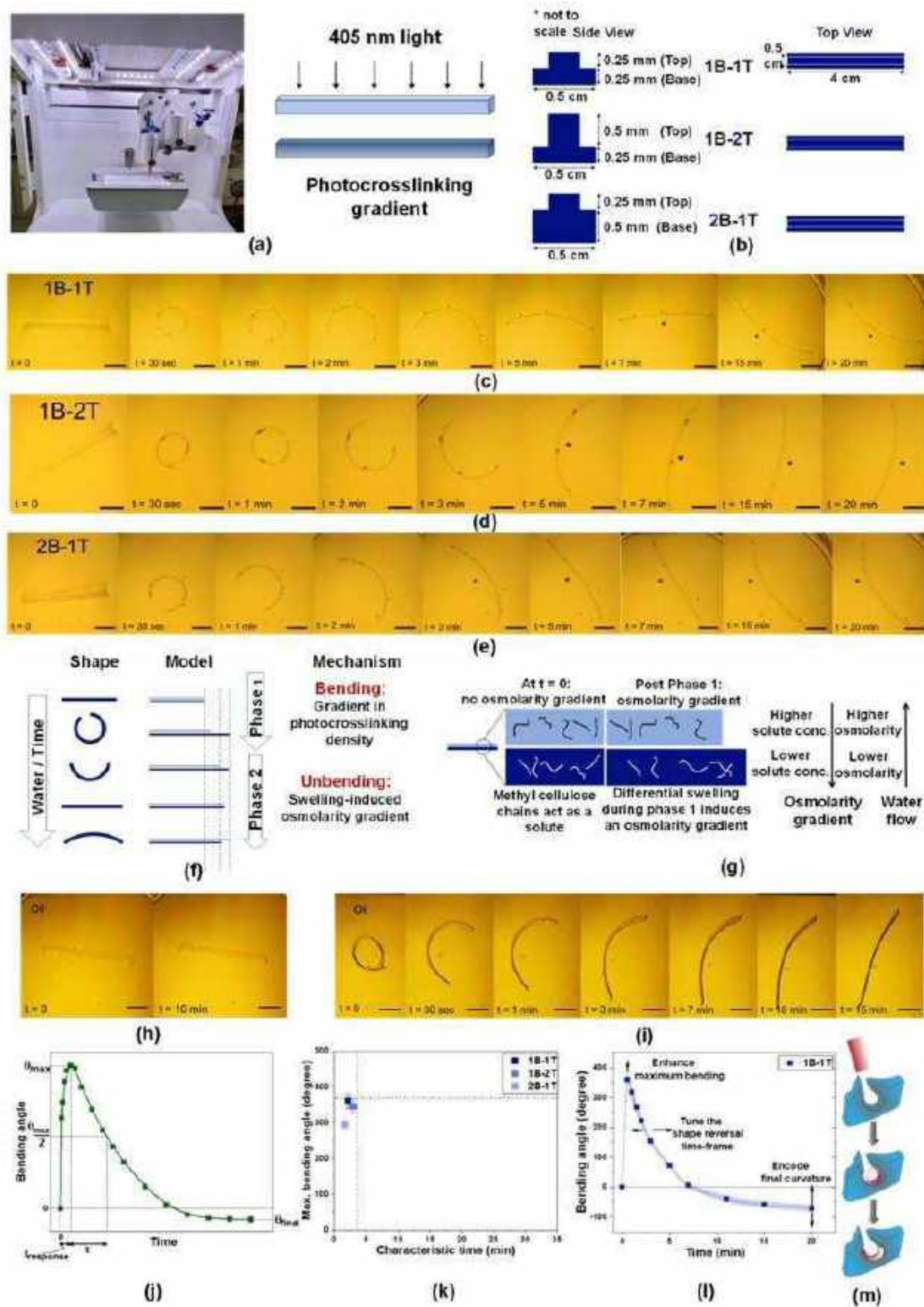


Figure 3- 4: Sequential, bi-directional shape-morphing behavior of single-component hydrogel beams (a) 3D printing setup: The precursor ink solution is extrusion 3D printed and photocrosslinked to impart shape fidelity (b) The various T-beam designs (c-e) The sequential,

bi-directional shape-morphing behavior of CMC-MA/MC hydrogel beams. (c) 1B-1T design (d) 1B-2T design (e) 2B-1T design. The asterisk is used to indicate the reversal of beam curvature. (f) A schematic illustration of the underlying shape change mechanisms guiding the shape-morphing behavior of the hydrogel beams (g) A schematic illustration of the differential swelling-induced osmolarity gradient that is responsible for the shape reversal of the beam (h) CMC-MA hydrogel beam immersed in oil. No significant bending deformation is observed. (i) As-printed CMC-MA hydrogel beam is immersed in oil to induce shape transformation from linear to ring, and subsequently transferred in oil. The ring-shaped hydrogel beam undergoes shape change in the opposite direction as a result of internal water redistribution due to differential swelling-induced osmolarity gradient. (j) Determination of the various parameters from the bending angle-time curve (k) The single-component CMC-MA/MC beams placed in the θ_{max} - τ plot (l) Desired modulations of the bending angle-time curve to suit device-specific requirements (m) Encoding the final curvature of the hydrogel device in addition to its deployability can lead to improved clinical outcomes.

During photocrosslinking, the attenuation of light with increasing depth (Figure 3- 6 f) leads to a spatial gradient in crosslinking density across the thickness of the hydrogel beam. Specifically, the top part experiences greater intensity of the incoming irradiation and exhibits higher crosslinking than the bottom[14]. When immersed in deionized water, this photocrosslinking gradient gives rise to non-uniform swelling within the hydrogel beam, generating internal stresses that drive the rapid bending of the hydrogel beam into a ring shape within a span of a few seconds (Figure 3- 4 f). As a control, we immersed the as-printed hydrogel beam in oil and observed no noticeable curvature, indicating that the initial bending deformation is mediated by anisotropic water uptake (Figure 3- 4 h). The anisotropic uptake of water also disrupts the initially homogeneous distribution of the solute polymeric chains (MC), triggering the next phase of the shape-morphing of the hydrogel beam. The highly viscous

nature of MC and its physical entanglements with the crosslinked matrix (CMC-MA) restrict its mobility and hinder its diffusion within the hydrogel network. Consequently, the differential swelling-induced changes in solute concentration between the top and bottom regions establish an internal osmotic gradient[30], resulting in the transfer of water from the bottom to the top portions of the hydrogel beam and the reversal of the bending of the hydrogel beam (Figure 3- 4 g). To verify this, we immersed the as-printed hydrogel beam in water and subsequently transferred/immersed the hydrogel in oil once it reached its maximum bending state. The hydrogel ring gradually opened in oil, confirming our hypothesis that the second shape transformation is driven by an internal water redistribution as a consequence of the differential swelling-induced osmolarity gradient (Figure 3- 4 i). This proposed actuation mechanism is material agnostic, which is demonstrated through four different hydrogel compositions, namely CMC-MA/MC, methacrylated chitosan (CS-MA)/poly(ethylene glycol) dimethacrylate (PEGDMA)/MC (refer section 1.1.5), methacrylated κ -carrageenan (k-CA-MA)/MC (Figure 3- 5 a, c), and methacrylated alginate (Alg-MA)/MC (Figure 3- 5 b, d).

Next, we delineate the temporal evolution of hydrogel beams (Figure 3- 4 (c-e)) by plotting temporal shape-morphing behavior (bending angle-time curves). This enables the quantification of shape transformations and facilitates the characterization of the deployability of the hydrogels under study (Figure 3- 4 j). The promptness of initial response on stimulation ($t_{response}$) and the maximum extent of bending deformation (θ_{max}) exhibited by the hydrogel beam serve as key performance indicators of its ability for rapid miniaturization, which is critical for realizing optimal outcomes in minimally invasive therapeutic procedures. Additionally, the characteristic time for shape reversal (τ), defined as the time taken to reach the half-maximum bending angle from the maximum bending angle state) and the final bending angle (θ_{final}) attained upon completion of the recovery process may be interpreted as informative proxies for assessing the shape reversal of the hydrogels. These parameters are

readily obtainable from the bending angle-time curve and provide a simple yet effective means to evaluate the bi-directional shape-morphing behavior exhibited by the hydrogels (Figure 3-4 j). In the case of CMC-MA/MC hydrogel beams, we observe (1) an almost instantaneous response, with $t_{response}$ less than 30 seconds across all three beam architectures, (2) the θ_{max} decreases with change in beam design (1B-1T: $360^\circ \pm 20^\circ$, 1B-2T: $346^\circ \pm 18^\circ$, 2B-1T: $294 \pm 13^\circ$) as predicted from Timoshenko theory[31], and (3) the τ of the hydrogel beams (1B-1T: 2.1 ± 0.1 min, 1B-2T: 3.0 ± 0.7 min, 2B-1T: 1.6 ± 0.5 min) are considerably higher than $t_{response}$, which hints at the different mechanisms at play. Interestingly, the beams tend to attain a final curvature in the opposite direction to their initial bending, with θ_{final} less than 0° for all three beam designs.

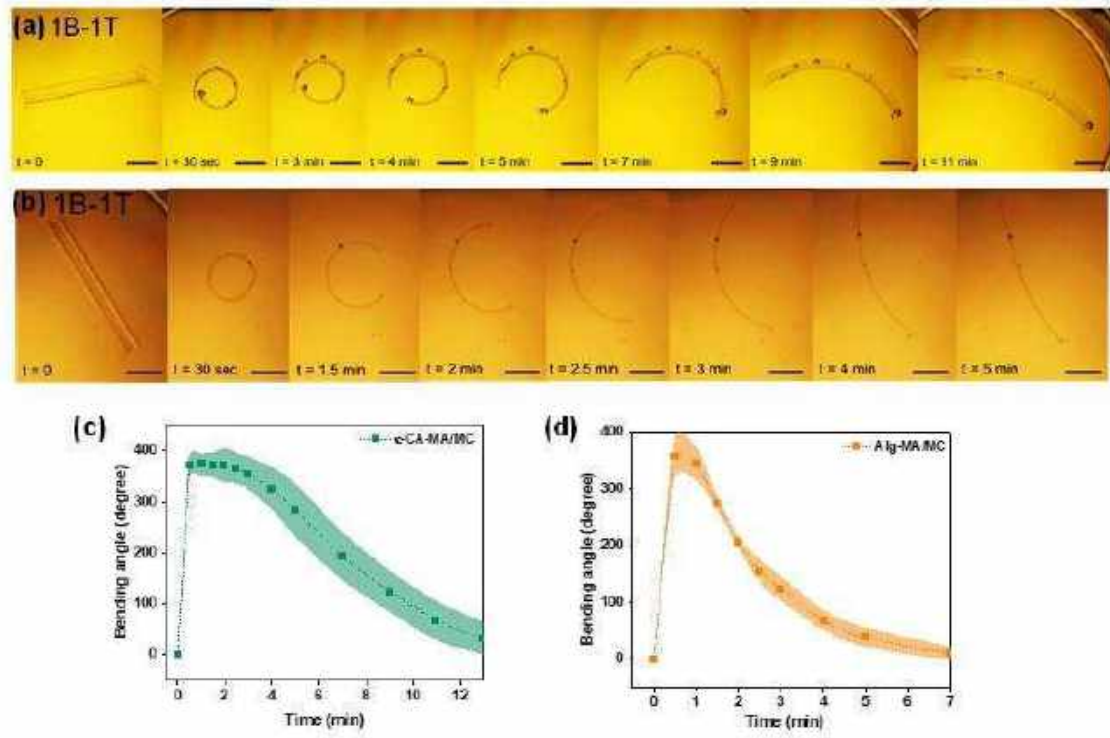


Figure 3- 5: The sequential, bi-directional shape-morphing behavior of (a) κ -CA-MA/MC hydrogel beams (b) Alg-MA/MC hydrogel beam (scale bar = 1 cm). Bending angle-time curve of (c) κ -CA-MA/MC hydrogels (1B-1T design, n = 4 samples) (d) Alg-MA/MC hydrogels (1B-1T design, n = 3 samples).

5.3.4 Need for Multi-Component Design

Efficiently programming hydrogels to exhibit deployable behavior to meet user-defined requirements necessitates precise tuning of the four fundamental parameters ($t_{response}$, θ_{max} , τ , θ_{final}). In particular, achieving orthogonal control over θ_{max} and τ is critical for independent manipulation of the hydrogel's shape miniaturization and shape reversal processes (Figure 3- 4 l). However, optimizing material concentrations to attain a desired functionality entails consequential alterations to the hydrogel properties (crosslinking density, volumetric swelling, swelling kinetics), which can potentially affect other critical parameters. Furthermore, modulating the material concentrations also risks compromising the desired rheological properties, rendering this approach unfeasible for the simultaneous tuning of these parameters.

The architectural design of the beams also impacts their bending characteristics. According to the Timoshenko equation, thicker beams display diminished bending tendency (θ_{max}), whereas ultra-thin beams are not mechanically robust and may also be limited by their ability to yield gradients in photocrosslinking. Hence, alteration of the beam design alone is inadequate to accentuate their deployable behavior (Figure 3- 4 k). In addition to deployability, we also want to encode the final shape of the hydrogel (or θ_{final} of the hydrogel beam) to make it conform better to the geometry of the implantation site, as illustrated in Figure 3- 4 m. However, the factors that determine the θ_{final} of the hydrogel beam are not well-understood, which makes it challenging to customize the final bending angle as desired. Whereas single-component hydrogels are simpler to fabricate as they are less demanding in terms of material synthesis and chemical modifications, several applications may benefit from layered multi-component formulations[32-34]. For instance, the ability to position multiple cell types in distinct hydrogel layers in a spatially controlled manner is a highly desired attribute in the field of tissue engineering.

To address these limitations, we have devised a multi-component design strategy for the fabrication of deployable hydrogels, wherein we harness the innate differences in swelling behavior (both kinetic and equilibrium) of the constituent hydrogel components to exact independent and precise control over θ_{max} , τ , θ_{final} .

5.3.5 Dual-component Programmable, Deployable Hydrogel

5.3.5.1 The Second Component

The dual-component deployable hydrogel system comprises two layered distinct semi-IPN hydrogel components, of which the first component, CMC-MA/MC, has been extensively characterized and investigated. To ensure uniform polymeric solute concentration (post photocrosslinking) in both hydrogel components, we maintain the concentration of MC at 6% w/v in the second component (same as the concentration of MC in CMC-MA/MC hydrogel). The material (photocrosslinkable polymer(s)) selection for the second component is guided by the mechanistic insights gained from the single-component model. As previously elucidated for CMC-MA/MC, the initial bending of the hydrogel beam stems from the differential swelling of the top and bottom regions, with the top region exhibiting lesser expansion. Over time, the length of the top region increases, surpassing that of the bottom region, resulting in ring opening and a slight curvature in the opposite direction. To recapitulate this effect in a dual-component system, the constituent hydrogels should mimic the dynamic changes between the top and bottom regions of the single-component model. In our dual-component design, the CMC-MA/MC hydrogel forms the bottom layer, whereas the second hydrogel component is engineered to imitate the top part of the single-component model by tuning its swelling kinetics and equilibrium swelling (Figure 3- 7 a). The second semi-IPN hydrogel is therefore tailored to exhibit a slower swelling kinetics than the first hydrogel in the initial stages and ultimately possess a higher equilibrium swelling, using methacrylated chitosan (CS-MA) and poly(ethylene glycol) dimethacrylate (PEGDMA) at 1% and 10%, respectively. The swelling

profiles of cylindrical constructs (10 mm diameter and 1 mm thickness, with 60% infill density) of CMC-MA/MC and CS-MA/PEGDMA/MC are plotted in Figure 3- 7 b, which clearly depicts the desired differences in innate swelling behavior between the two hydrogel components.

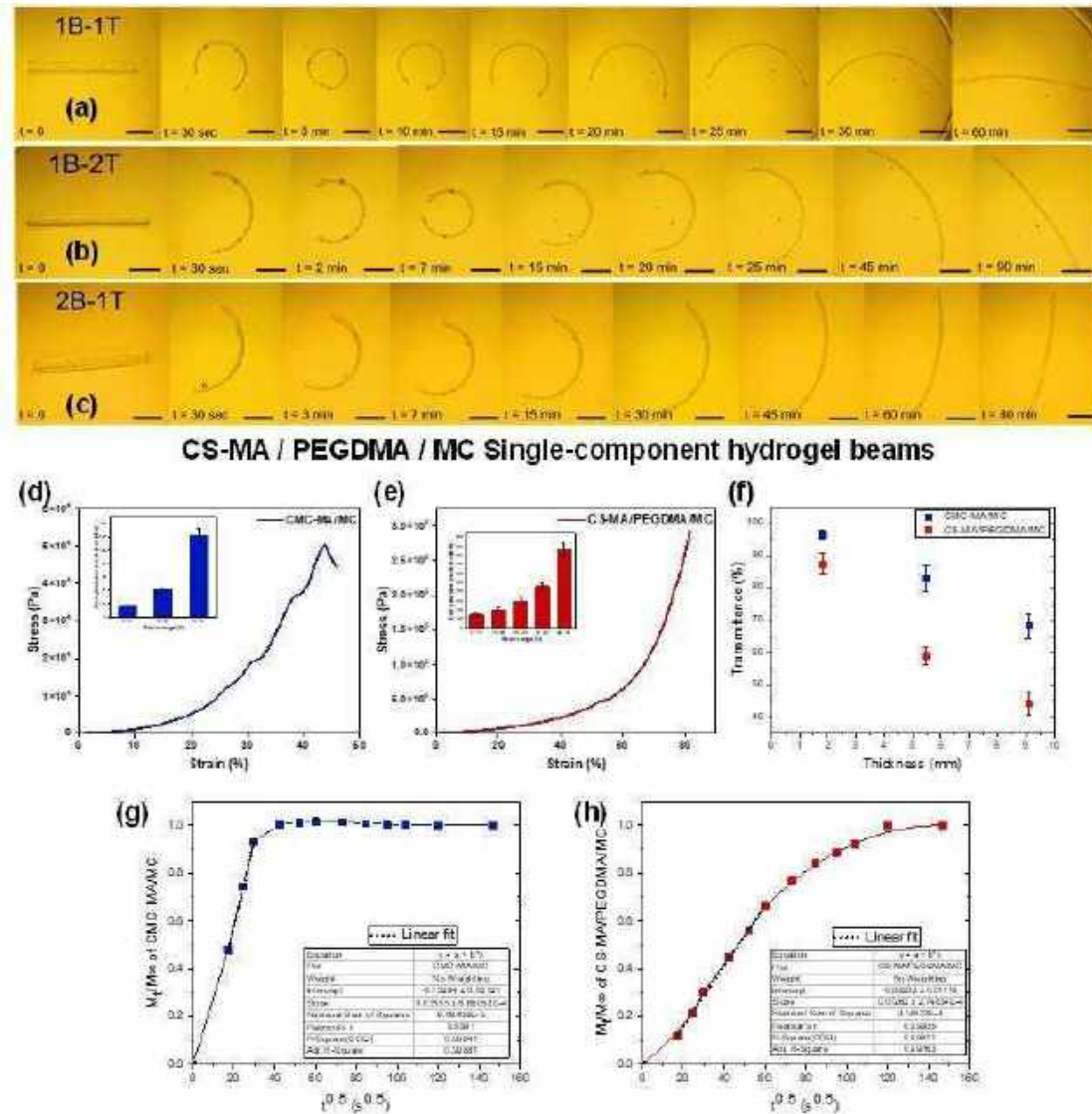


Figure 3- 6: The sequential, bi-directional shape-morphing behavior of CS-MA/PEGDMA/MC hydrogel beams. (a) 1B-1T design (b) 1B-2T design (c) 2B-1T design. Stress-strain curve of (d) CMC-MA/MC and (e) CS-MA/PEGDMA/MC hydrogels under compressive loading. The compressive modulus at different strain ranges is provided in the

inset. (f) Transmittance (at 405 nm) of CMC-MA/MC and CS-MA/PEGDMA/MC precursor gels of varying thickness. Fractional water uptake as a function of the square-root of time for (g) CMC-MA/MC, and (h) CS-MA/PEGDMA/MC hydrogels.

We then investigated the bi-directional shape-morphing behavior of the CS-MA/PEGDMA/MC hydrogels. Based on the observed swelling profiles, it is evident that CS-MA/PEGDMA/MC hydrogel exhibits slower swelling kinetics compared to CMC-MA/MC (refer [Video V5.2](#)). This manifests as a prolonged $t_{response}$ and τ for CS-MA/PEGDMA/MC hydrogel beams, as the temporal characteristics of these beams are heavily influenced by the diffusivity and transport of water molecules within the hydrogel matrix. Interestingly, the $t_{response}$ for the CS-MA/PEGDMA/MC hydrogel beams is not substantially impacted by changes in beam design (1B-1T: 5 min, 1B-2T: 7 min, 2B-1T: 7 min), but τ increases markedly (1B-1T: 17.1 ± 0.3 min, 1B-2T: 21.2 ± 1.9 min, 2B-1T: 29.8 ± 6.5 min). The θ_{max} of these beams suffers a reduction with a change in beam design (1B-1T: $320^\circ \pm 7^\circ$, 1B-2T: $282^\circ \pm 29^\circ$, 2B-1T: $164 \pm 13^\circ$), similar to CMC-MA/MC hydrogel beams. Furthermore, in the case of CS-MA/PEGDMA/MC hydrogel beams, the θ_{final} are close to 0° , and no curvature in the reverse direction is observed (refer Figure 3- 6).

5.3.5.2 Dual-component vs. Single-Component Deployable Hydrogels

The initial difference in swelling rates (Figure 3- 6 g, h) between the constituent hydrogel components synergistically reinforces the photocrosslinking gradient and produces an auxiliary driving force for enhanced bending deformation, resulting in an amplified θ_{max} across all beam designs (1B-1T: $476^\circ \pm 59^\circ$, 32% increase over CMC-MA/MC and 49% increase over CS-MA/PEGDMA/MC; 1B-2T: $383^\circ \pm 10^\circ$, 11% increase over CMC-MA/MC and 36% increase over CS-MA/PEGDMA/MC; 2B-1T: $358^\circ \pm 35^\circ$, 22% increase over CMC-MA/MC and 118% increase over CS-MA/PEGDMA/MC) (Figure 3- 7 (d-i, j, and l)).

The $t_{response}$ and τ values of the dual-component hydrogel beams both increase in comparison to CMC-MA/MC and have an intermediate value to that of their single-component beams. While CMC-MA/MC hydrogel beams of different designs possess a $t_{response}$ of ~30 seconds, the $t_{response}$ of the dual-component hydrogel beams increases one-fold for 1B-1T and 2B-1T and three-fold for 1B-2T. The dual-component hydrogel beams also display a greater τ for all three beam designs (1B-1T: 3.8 ± 0.7 min, ~81% increase over CMC-MA/MC and ~78% decrease over CS-MA/PEGDMA/MC; 1B-2T: 6.4 ± 1.3 min, ~113% increase over CMC-MA/MC and ~70% decrease over CS-MA/PEGDMA/MC; 2B-1T: 4.5 ± 1.0 min, ~181% increase over CMC-MA/MC and ~85% decrease over CS-MA/PEGDMA/MC) (Figure 3- 7 (d-i, k, and l)). These results suggest that tuning the swelling kinetics of the second component can be a viable strategy to tune the τ of the dual-component system. Specifically, combining the first hydrogel with a comparatively slower swelling hydrogel will increase the τ of the dual-component system and vice versa.

The final bending angle of the dual-component hydrogel beams is less (more negative) than their single-component counterparts, and the beams display significant curvature in the opposite direction (Figure 3- 7 d-i). This is because the difference in equilibrium swelling between the constituent hydrogel layers favors the bending of the beams in the reverse direction. This phenomenon, in conjugation with the swelling-induced osmolarity gradient, drives the opening of the hydrogel ring and causes the bending of the dual-component hydrogel beams in the reverse direction even further than that observed in CMC-MA/MC. Hence, through control of the equilibrium swelling via the targeted choice of the second component, it is possible to pre-program the final shape of a dual-component deployable hydrogel.

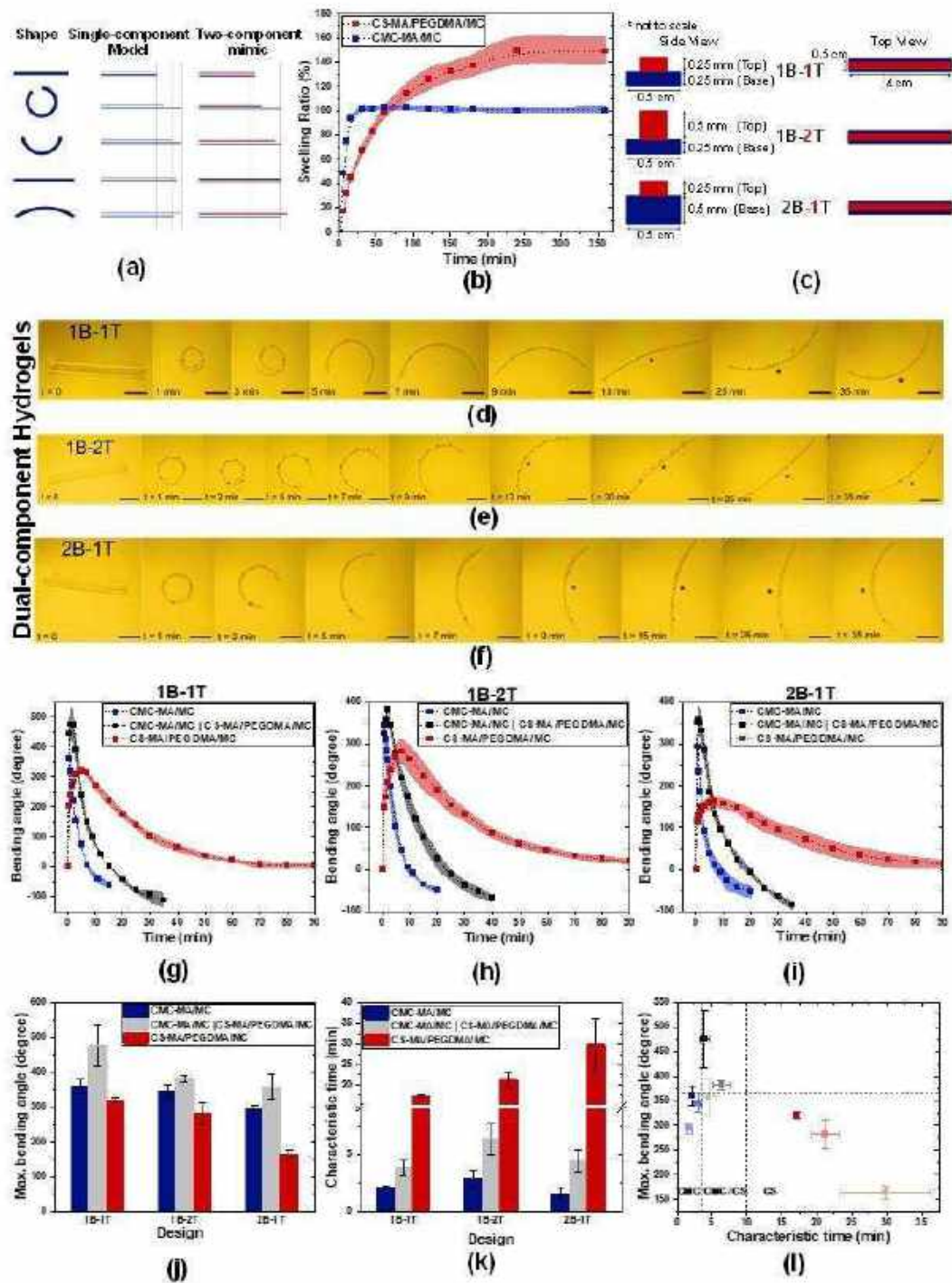


Figure 3- 7: Design and performance of dual-component hydrogel beams. (a) Dual-component hydrogel beam design based on mechanistic understanding of the single-component system (b) Swelling ratio vs. time curve of the two hydrogel components (CMC-MA/MC and CS-MA/PEGDMA/MC) (c) Dual-component hydrogel beam designs with CMC-MA/MC as the

base layer(s) and CS-MA/PEGDMA/MC as the top layer(s) (d-f) The sequential, bi-directional shape-morphing behavior of CMC-MA/MC | CS-MA/PEGDMA/MC dual-component hydrogel beams (d) 1B-1T design (e) 1B-2T design (f) 2B-1T design. The asterisk is used to indicate the reversal of beam curvature. (g-i) The bending angle-time curves of the single-component and dual-component hydrogel beams (g) 1B-1T design (h) 1B-2T design (i) 2B-1T design (j) The maximum bending angle (θ_{max}) of the hydrogel beams grouped in accordance to their design (k) The characteristic time (τ) of the hydrogel beams grouped in accordance to their design (l) The θ_{max} - τ plot of the hydrogel beams. Dual-component hydrogel beams exhibit a higher θ_{max} and an intermediate τ compared to their single-component counterparts. The shaded region accompanying the data points in plots b, g, h, and i depicts the error bands based on standard deviation of the triplicate measurements.

5.3.5.3 Deployable Cell-Laden Hydrogels

To investigate the feasibility of cell encapsulation within these hydrogel constructs, we bioprinted cell (L929 mouse fibroblasts)-laden hydrogel scaffolds for both ink formulations and cultured under standard cell culture conditions. The metabolic activity of the cells was quantified using the Alamar Blue assay, which exhibited a gradual increase over a period of 14 days for both inks, indicating excellent viability and proliferation of the cells within the hydrogel scaffolds (Figure 3- 8 (a, b)). LIVE/DEAD staining and 3D fluorescence images obtained on days 1, 4, 7, and 14 further validated the increase in cell number and viability (Figure 3- 8c). An average cell viability of more than 85% was observed on day 1 for both inks, and the bioprinted hydrogel scaffolds maintained high levels of cell viability (>90%) for up to 14 days.

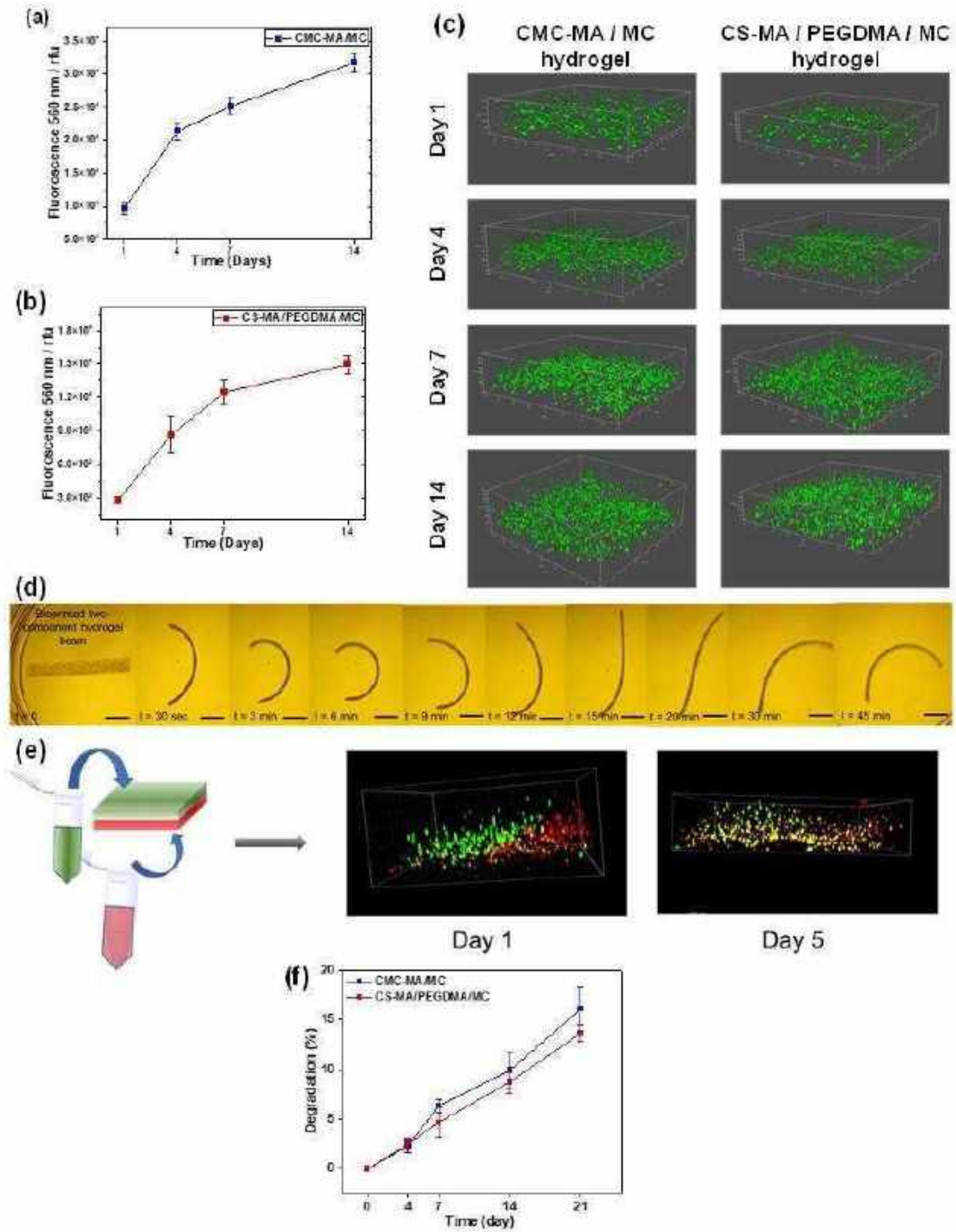


Figure 3- 8: 4D bioprinting. Alamar blue assay of cell (L929 mouse fibroblast)-laden (a) CMC-MA/MC hydrogel and (b) CS-MA/PEGDMA/MC hydrogel (c) 3D fluorescent confocal micrographs of the cells stained with the live-dead dyes taken on day 1,4,7, and 14. (d) 4D bioprinted dual-component hydrogel beam exhibiting sequential, bi-directional shape-morphing behavior. (e) Schematic representation of bi-layered two-component hydrogel

structures loaded with green and red dye-tracked cells in different layers. 3D fluorescent confocal micrographs were taken on day 1 and day 5. (f) Degradation behavior of CMC-MA/MC and CS-MA/PEGDMA/MC hydrogels.

Furthermore, we investigated the shape-morphing behavior of the bioprinted dual-component hydrogel beams and found that they exhibit sequential, bi-directional shape-morphing behavior similar to their cell-free counterparts (Figure 3- 8d). Additionally, the multi-component printing capability can be instrumental for the precise spatial arrangement of distinct cell types across multiple layers (Figure 3- 8e). These findings establish the favorable biprintability and cytocompatibility of the extrusion-printed CMC-MA/MC and CS-MA/PEGDMA/MC hydrogels, highlighting their potential as deployable, biodegradable (Figure 3- 8f) tissue engineering scaffolds.

5.3.5.4 2D/2.5D Shapes

The unique spatiotemporal transformations exhibited by these hydrogels present unprecedented opportunities for realizing complex devices that are unattainable through conventional 4D shape change strategies. A key advantage of our hydrogel devices is that they only require a single stimulation (water) to undergo the entire 4D bi-directional shape-morphing process, which makes it highly convenient and attractive for clinical applications where access to multiple stimuli (often requiring external power sources) can be challenging. For instance, the use of magnetic fields for stimulation requires the use of expensive and bulky instrumentation, such as coils and circuits, limiting its easy adoption in the clinic. This limitation is obviated in our hydrogel devices, which require no additional triggers to attain their final shape post-deployment at the desired location in their maximal miniaturized form. Additionally, it is also possible to achieve on-demand shape changes *in vivo* by harnessing the moisture within the human body. Here, we conceptually demonstrate how we can leverage the

sequential, bi-directional shape-morphing behavior of these hydrogels toward the fabrication of minimally-invasive, soft biomedical devices.

Specifically, we fabricate two different 2D geometries, namely a five-petal flower and a rectangle (length : width = 3:1) (Figure 3- 9 a,b), using the dual-component hydrogel system described previously to illustrate the size reduction and subsequent shape reversal characteristics that are critical for deployable devices. In the case of both shapes, the base layer is printed with CMC-MA/MC ink with a 100% infill density, while the top layer is printed with CS-MA/PEGDMA/MC ink with a 40% infill density for the flower geometry and a 30% infill density for the rectangle geometry. On immersing in water, the flower petals rapidly close and fold onto themselves, leading to a ~60% reduction in shape diameter. The petals gradually unfold with time, and the flower reverts to its initial open-petal configuration (Figure 3- 9 c). The rectangle, on the other hand, displays a more sophisticated folding behavior when placed in water (Figure 3- 9 d). Initially, when the bottom surface of the hydrogel comes in contact with the water, the rectangle folds along the width (short axis), forming a long, hollow tube-like structure with a diameter of ~ 4 mm (40% of the rectangle width). Subsequently, water flows through this tube, causing it to reorient itself and fold into a tube along its length (long axis). This tube then unfolds with time and returns to the initial flat rectangular geometry.

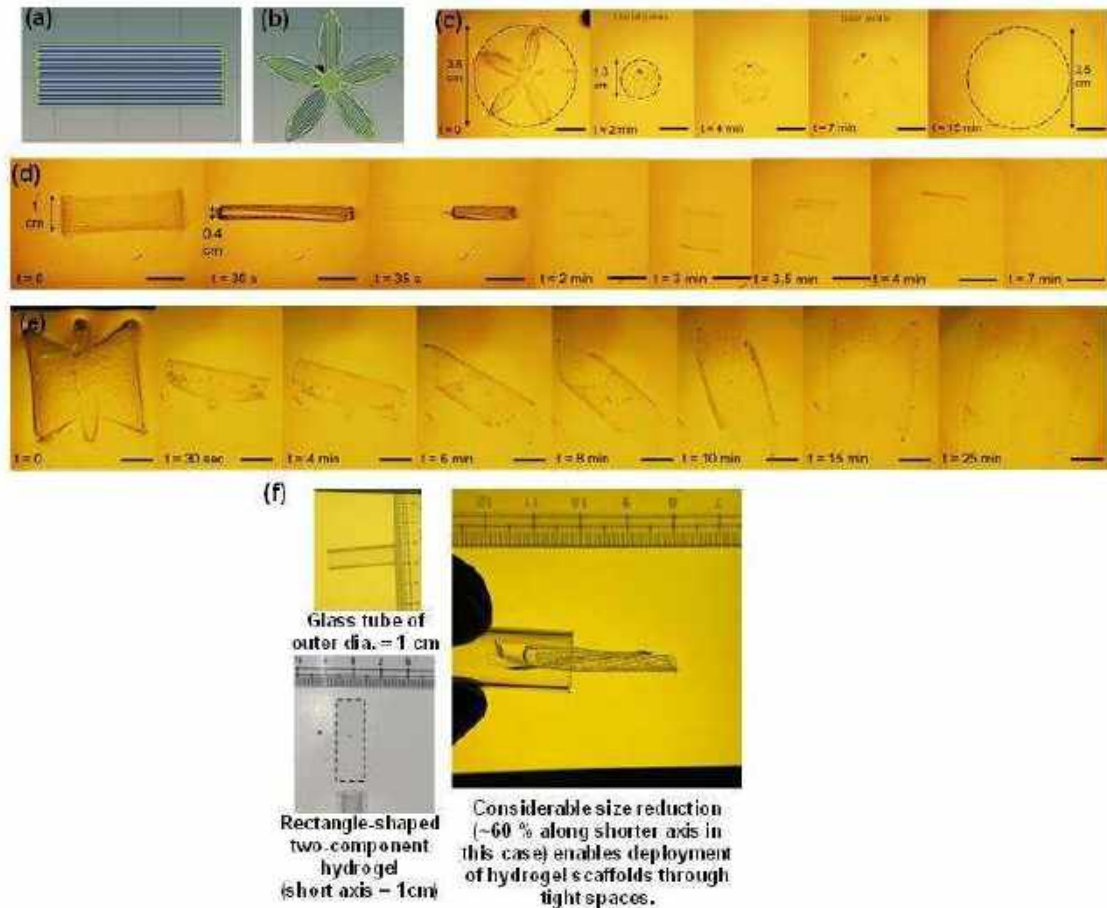


Figure 3- 9: 2D/2.5D shapes. 3D model of (a) rectangle (b) 5-petal flower (c) Opening and closing of flower petals. Temporal evolution of (d) rectangular geometry (e) butterfly-shaped 2D construct when immersed in water (f) Deployability of the rectangular hydrogel device through a narrow glass tube.

We utilize rectangular geometry to showcase the deployable nature of these hydrogel constructs (Figure 3- 9 f). The rectangular hydrogel construct measures 1 cm in width and 3 cm in length, while the inner diameter of the glass tube is just short of 1 cm, making it a tricky task to deliver the hydrogel construct through the glass tube. However, the folded tube-like configuration of the construct enables its facile delivery through the glass tube without rupture, owing to the reduced dimension along the width.

The remarkably fast (within a few seconds) folding time of our hydrogels (when immersed in water) makes them ideal for on-demand applications within clinical environments. The characteristic time of these hydrogels, typically on the order of a few minutes in our experiments, can be appropriately tuned to provide a suitable time frame for surgeons to insert/deploy the hydrogel scaffold inside the human body. Once implanted, the hydrogel scaffold can unfold and assume its final shape without the need to any additional stimulation. We believe that this novel 4D bi-directional shape morphing technique obviates the need for multiple triggers and mitigates the complexities associated with administering a stimulus in vivo, potentially leading to improved clinical outcomes. Our results provide a glimpse into the enormous scope of applications of such hydrogel devices in drug delivery and tissue engineering, especially for the minimally invasive delivery of large or irregularly-shaped hydrogel constructs (Figure 3- 9 e) laden with active biological ingredients through tight spaces and channels.

5.3.6 Programming Hydrogel Beams Through Multi-Component Assembly: A Practical Guide for Material Selection and Construct Design

As previously discussed, the θ_{max} , τ , and θ_{final} of the hydrogel beams can be independently modulated through multi-component design architectures. Whereas the material composition of the first hydrogel component is typically chosen based on the application, the deployability and final shape of this hydrogel can be further augmented by integrating it with a second component that is specially engineered to meet the desired values of θ_{max} (increase), τ (increase or decrease), θ_{final} (increase or decrease). The findings reported in this study enable us to propose a guide for adopting a broad spectrum of polymeric hydrogels to engineer deployable bi-directional shape-morphing 4D printed gels in the manner described above. Here, we present a systematic approach for designing the second component based on user-defined requirements, given the swelling profile of the first component.

1) An initial difference in swelling rate between the hydrogel layers can provide an additional impetus for enhanced θ_{max} . Hence, the second component should preferably exhibit a large mismatch in swelling rate during the initial time points of the swelling curve. Additionally, the two components should be positioned in different layers such that they complement the photocrosslinking gradient, with the faster-swelling component located at the bottom. If this is not the case, the photocrosslinking gradient and the multi-component swelling differential act as competing driving forces, which results in a considerably lower θ_{max} (refer Figure 3- 10 a, b). 2) To increase the τ , the first hydrogel should be paired with a hydrogel having a slower swelling kinetics and vice versa. This is because shape reversal is a transport-dependent phenomenon where the diffusivity of water molecules plays a significant role. Further optimization of τ can be achieved through modifications in the architectural design of the beams, considering the total thickness of the beam as well as the thickness of the individual gel components. 3) The equilibrium swelling differences between the constituent hydrogel layers can be utilized to tailor the final curvature of the hydrogel beam (θ_{final}). By tuning the equilibrium swelling of the second component in relation to the first component, the final shape of the hydrogel beam can be altered in a manner similar to conventional multi-component 4D shape change mechanisms. For example, if the top component has a lower equilibrium swelling, the beam will tend to increase its final bending angle, and vice versa.

Based on these guidelines, we can determine the required swelling profile of the second component for each of the possible cases: (a) increased τ , increased θ_{final} (b) increased τ , decreased θ_{final} (c) decreased τ , increased θ_{final} (d) decreased τ , decreased θ_{final} (refer Figure 3- 10 (c-f)). The identification of the requisite swelling profile allows for the judicious selection of appropriate polymers for the second hydrogel component. Overall, we envisage that these guidelines will provide a comprehensive framework for designing dynamically reconfigurable hydrogels with tunable functionalities for biomedical and other applications.

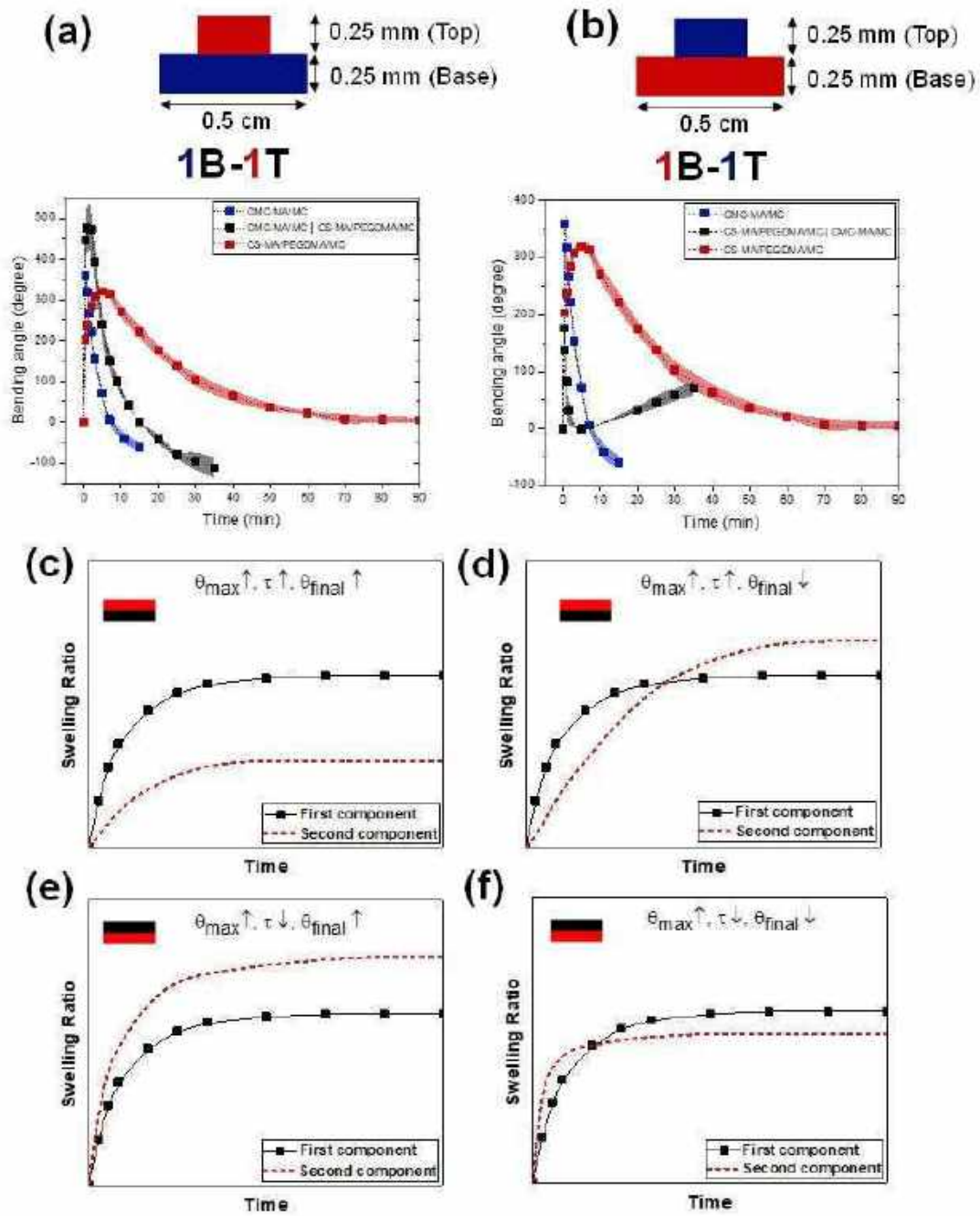


Figure 3- 10: The effect of design in two-component hydrogel structures (a) Bottom layer: CMC-MA/MC, Top layer: CS-MA/PEGDMA/MC (b) Bottom layer: CS-MA/PEGDMA/MC, Top layer: CMC-MA/MC. The shaded region depicts the error bands based on standard deviation of the triplicate measurements. The required swelling profile of the second component in accordance with device requirements (c) increased τ , increased θ_{final} (d) increased

τ , decreased θ_{final} (e) decreased τ , increased θ_{final} (f) decreased τ , decreased θ_{final} . The position (base or top) of the first (shown in black) and second (shown in red) components of the dual-component hydrogel beam is shown in the inset of each of the plots.

5.4 Conclusion

In this work, we introduce a novel platform technology for fabricating deployable hydrogel devices capable of sequential, bi-directional shape transformations upon a single stimulation (immersion in aqueous solutions). The material selection for these devices can be guided by existing data available for already investigated hydrogel systems (from the θ_{max} - τ plot and their bending angle-time curves). Furthermore, the spatiotemporal characteristics of these hydrogel devices can be further optimized by the rational design of multi-component assemblies (as detailed in the previous section) to meet specific clinical requirements. Unlike conventional shape-memory polymers/hydrogels, the final shape of the hydrogel post-deployment can be pre-programmed to better conform to the geometry of the implantation site. Owing to the mild fabrication process and biocompatible stimulation, these deployable devices are ideal for delivering biological cargo through narrow channels or confined spaces in the human body.

Through a proof-of-concept demonstration of these bi-directional shape-morphing hydrogels, we provide biomedical engineers and clinicians with a previously unavailable, biocompatible, safe, and precise method to design programmable and deployable hydrogel-based implantable devices (refer Table 5- 2). Moreover, the underlying actuation mechanism governing the shape transformations, wherein the outcome of the first phase of shape transformation induces the subsequent transformation(s), can be extended to other material systems for the development of dynamically reconfigurable architectures with tunable functionality for applications in soft robotics, tissue engineering, drug delivery, minimally invasive devices, and beyond.

Table 3- 2: Comparative analysis of our work with state-of-the-art bi-directional shape-morphing hydrogels

MATERIAL		SCHEME OF ACTUATION				SHAPE TRANSFORMATIONS			4D BIOPRINTING		GENERAL REMARKS	REF.
<i>Hydrogel composition</i>	<i>No. of hydrogel components</i>	<i>Stimulus</i>	<i>Mode of stimulation</i>	<i>4D Mechanisms</i>	<i>Generalizable approach</i>	<i>Time span</i>	<i>Extent of Deformation (bending angle)</i>	<i>Spatiotemporal tunability</i>	<i>3D-printed?</i>	<i>Live cell encapsulation?</i>		
Photocrosslinkable polymer (CMC-MA or Alg-MA or κ -CA-MA or CS-MA+PEGDMA) + physically entangled polymer (MC)	Single/ Multi	1. Water	1. Bending: Immersion in aqueous solution 2. Unbending: No external stimulation required	1. Folding: Photocrosslinking gradient, dynamic swelling differences between constituent hydrogel layers (for dual-component systems) 2. Unfolding: Differential swelling-induced internal osmolarity gradient, dynamic swelling differences	Yes	1. Bending: Ultrafast, typically within seconds to few minutes 2. Unfolding: Typically varies from a few minutes to hours, depending upon the hydrogel composition	0° to 164° - 476° 0° represent linear configuration; 360° represents ring (full circle) configuration	1. Precise control over magnitude of deformation and duration of shape transformations is demonstrated. 2. Additionally, a systematic guideline is put forth to assist in material selection that align with specific requirements.	Yes	Yes	1. This is the first demonstration where the bi-directional shape morphing behavior is achieved through a single initial mild stimulation. 2. The concept of an induced osmolarity gradient is introduced as a novel mechanism to drive shape transformations in hydrogels. 3. The proposed mechanism is material-agnostic and holds potential for diverse applications.	This work

				between constituent hydrogel layers (for dual-component systems)							<p>4. The pre-programmed shape transformations eliminate the necessity of a secondary <i>in vivo</i> stimulation to trigger a subsequent shape change following deployment.</p> <p>5. The tuneable spatiotemporal behavior of the hydrogel constructs is critical for tailoring their properties to meet clinical requirements.</p> <p>6. The final shape of the hydrogel constructs can be customized to conform to the curvature of implantation site, which may significantly differ from initially printed shape.</p>	
poly(N,N-dimethylacrylamide) (or poly(N-isopropylacrylamide)) + Laponite XLG clay + glucose oxidase +	Single	1. Water 2. Temperature	1. Bending: Immersion in aqueous solution at room temperature	1. Bending: Anisotropic swelling due to shear-induced alignment of fibres	Yes, but not demonstrated in the study.	1. Bending: Fast, typically within minutes	Not applicable	1. Tuneable temporal behaviour is not demonstrated. 2. However, exquisite control	Yes	No	1. The bi-directional shape morphing behaviour is realized by employing two distinct triggers. 2. The suitability of this technique for biomedical	Sydney Gladman <i>et al.</i> , <i>Nat. Mater.</i> , 2016. [18]

glucose + nanofibrillated cellulose (NFC)			2. Unfolding: Heating/Immersion in hot water bath at 50° C	2. Unfolding: Thermoreversible behavior of poly(N-isopropylacrylamide)		2. Unfolding: Not mentioned		over local curvature is achieved through utilization of mathematical models.			<p>applications is limited due to the requirement of temperatures surpassing the physiological temperature (50°C).</p> <p>3. Bioprinting/loading biological cargo within these hydrogels is not feasible due to the high temperature necessary for unfolding. Furthermore, the deswelling-based unfolding may generate osmotic stresses that can adversely affect cell viability.</p>	
Alginate methacrylate	Single	<p>1. Water</p> <p>2. Calcium chloride solution</p>	<p>1. Folding: Immersion in aqueous solution</p> <p>2. Unfolding: Immersion in calcium chloride solution</p>	<p>1. Folding: Photocrosslinking gradient, dehydration gradient</p> <p>2. Unfolding: Deswelling mediated by additional crosslinking with calcium ions.</p>	No	<p>1. Folding: Ultrafast, typically within seconds</p> <p>2. Unfolding: Ultrafast, typically within seconds</p>	Not applicable	<p>1. Shape transformation exclusively from a flat sheet to a tube is demonstrated, with the ability to modulate the tube diameter by adjusting printing conditions.</p> <p>2. Tuneable temporal behaviour is not demonstrated</p>	Yes	Yes (demonstrated only for bending)	<p>1. The bi-directional shape morphing behaviour is realized by employing two distinct triggers.</p> <p>2. Since the unfolding process relies on a deswelling-based mechanism, osmotic stresses may arise, which could compromise cell viability.</p> <p>3. Prolonged drying periods can adversely impact cell viability, while</p>	Kirillov <i>et al.</i> , <i>Adv. Mater.</i> , 2017. [22]

											incomplete drying can lead to semi-folded tubes.	
											4. This technique lacks the capability of achieving complex or large-scale shape transformations.	
Bilayer hydrogel system; each layer is composed of poly(N,N-dimethyl acrylamide-co-stearyl acrylate) (P(DMAAm-co-SA))-based hydrogels with different concentrations of DMAAm and SA monomers	Multi	1. Water 2. Temperature	1. Bending: Immersion in water 2. Unbending: Heating in air/water	1. Bending: Difference in equilibrium swelling between the constituent layers 2. Unbending: Shape memory effect of the layers	No	1. Bending: Fast, few minutes to hours (depending on the water temperature) 2. Unbending: Ultrafast, within seconds	0° to ~350° - 450° 0° represent linear configuration; 360° represents ring (full circle) configuration	1. The layer heights and the ambient temperature was found to affect the bending curvature and response time. 2. The ambient temperature also influences the extent and duration of shape recovery.	Yes	No	1. The bi-directional shape morphing behaviour is realized by employing two distinct triggers. 2. The elevated temperature range (50°C to 70°C) necessary for the unbending process renders these hydrogels unsuitable for biomedical applications.	Shiblee <i>et al.</i> , <i>Adv. Mater. Technol.</i> , 2019. [35]
Trilayer hydrogel. Layer 1: Oxidized (10%) and methacrylated (30%) alginate; Layer 2: methacrylated gelatin, Layer 3: Layer 1: Oxidized	Multi	1. Water	Entire shape transformation process: Immersion in water	The multi-material differences in swelling and asynchronous degradation leads to bi-directional bending.	No	Very slow, typically spanning ~24 hours to complete the entire shape-change process	0° to ~150° in one direction and ~250° in the other direction 0° represent linear	1. Tuneable temporal behaviour is not demonstrated. 2. Desired shape transformations can be programmed	No	Yes	1. The bi-directional shape-morphing characteristics of these hydrogels are governed by the interplay of competitive swelling and degradation mechanisms, necessitating the continuous presence of	Ding <i>et al.</i> , <i>Adv. Sci.</i> , 2021. [26]

(10%) and methacrylated (20%) alginate							configuration; 360° represents ring (full circle) configuration	through hydrogel patterning and design.			stimuli (water) throughout the entirety of the process. 2. Due to the notably protracted nature of shape transformations, these hydrogels lack the requisite promptness for biomedical applications requiring on-demand capabilities.	
N-isopropylacrylamide (NIPAM) with N,N'-methylenebisacrylamide (MBA, the crosslinker) in the water solution of poly(vinyl alcohol) (PVA)	Single	1. Water 2. Temperature	Entire shape transformation process: Cooling from 50° C to 15° C in water	The hydrogel exhibits non-monotonic shape transformation as a consequence of the differential swelling behavior in water during the cooling process, attributed to the interplay of stress and geometry effects.	Yes, but only for responsive hydrogels.	Ultrafast, takes about 10 seconds to complete the entire shape-change process	90° to 0° to 55° (Refer to the article for further details)	1. No spatial or temporal tuneability is demonstrated.	No	No	1. The bi-directional shape-morphing characteristics of these hydrogels necessitate the concurrent presence of two distinct stimuli. 2. As the underlying mechanism relies on stress and geometry factors, the application of this technique is limited to specific shapes and cannot be employed for arbitrary geometries. 3. The exceptionally rapid temporal dynamics associated with this phenomenon introduce practical constraints on its	Zhang <i>et al.</i> , <i>Nat. Commun.</i> , 2021. [25]

											implementation and utilization.	
											4. Live cell encapsulation within these hydrogels is not feasible due to the temperatures required for the shape-transformation process.	
(GB1) ₈ /(FL) ₈ bilayer protein hydrogel	Multi	1. PBS (or water) 2. guanidinium chloride (GdmCl)	1. Bending: Immersion in PBS 2. Unbending (to original linear configuration): Immersion in 6.0 M GdmCl containing buffers	1. Bending: Differential swelling of (GB1) ₈ and (FL) ₈ hydrogels in PBS 2. Unbending: Chemical denaturant (GdmCl) induced different swelling responses of the (GB1) ₈ and (FL) ₈ hydrogels	No	1. Bending: Slow, takes around 1 hour in PBS 2. Unbending: Slow	0° to ~95° 0° represent linear configuration; 180° represents ring (full circle) configuration	1. Tuneable temporal behaviour is not demonstrated. 2. The magnitude of bending deformation can be adjusted by modulating the denaturant concentration and manipulating the layer geometry.	No	No	1. The bi-directional shape morphing behaviour is realized by employing two distinct triggers. 2. The use of chemical denaturants imposes limitations on its applicability in biomedical contexts.	Bian <i>et al.</i> , <i>Nat. Commun.</i> , 2022. [36]
Oxidized and methacrylated alginate	Single	1. Water 2. pH	1. Bending: Immersion in PBS (pH 7.4), or water. 2. Unbending:	1. Bending: Photocrosslinking gradient 2. Unbending: Deswelling at low pH	No	1. Bending: Fast, within a few minutes to an hour 2. Unbending:	0° to ~100° - 700° 0° represent linear configuration; 360° represents	1. Tuneable temporal behaviour is not demonstrated. 2. The extent of bending deformation can	Yes	No	1. The bi-directional shape morphing behaviour is realized by employing two distinct triggers. 2. The unbending process of these hydrogels necessitates a specific low	Ding <i>et al.</i> , <i>Adv. Mater.</i> , 2022. [15]

			low pH (2.0) treatment			Fast, within a few minutes	ring (full circle) configuratio n	be modulated through variations in printing parameters.			<p>pH condition, thereby limiting their applicability to body regions where the pH interval aligns with the hydrogel's pH-responsive range.</p> <p>3. Owing to the requirement of low pH, these hydrogels are not well-suited for cell encapsulation/bioprinting.</p>	
--	--	--	---------------------------	--	--	----------------------------------	--	--	--	--	---	--

5.5 References

1. de Marco, C., S. Pané, and B.J. Nelson, *4D printing and robotics*. Science robotics, 2018. **3**(18): p. eaau0449.
2. Hann, S.Y., et al., *4D printing soft robotics for biomedical applications*. Additive Manufacturing, 2020. **36**: p. 101567.
3. Kim, S.H., et al., *4D-bioprinted silk hydrogels for tissue engineering*. Biomaterials, 2020. **260**: p. 120281.
4. Ding, A., et al., *4D cell-condensate bioprinting*. Small, 2022. **18**(36): p. 2202196.
5. Fernandes, R. and D.H. Gracias, *Self-folding polymeric containers for encapsulation and delivery of drugs*. Advanced drug delivery reviews, 2012. **64**(14): p. 1579-1589.
6. Rivera-Tarazona, L.K., et al., *4D printing of engineered living materials*. Advanced Functional Materials, 2022. **32**(4): p. 2106843.
7. van Manen, T., et al., *4D printing of reconfigurable metamaterials and devices*. . 2021, Commun. Mater: Commun. Mater. p. 2 (1), 56.
8. Wang, Y., et al., *Emerging 4D printing strategies for next-generation tissue regeneration and medical devices*. Advanced Materials, 2022. **34**(20): p. 2109198.
9. Chen, D., et al., *4D printing strain self-sensing and temperature self-sensing integrated sensor-actuator with bioinspired gradient gaps*. Advanced Science, 2020. **7**(13): p. 2000584.
10. Kuang, X., et al., *Advances in 4D printing: materials and applications*. Advanced Functional Materials, 2019. **29**(2): p. 1805290.
11. Jamal, M., et al., *Bio-Origami hydrogel scaffolds composed of photocrosslinked PEG bilayers*. 2013, Adv Healthc Mater Adv Healthc Mater. p. 2: 1142–1150.
12. Zhao, Z., et al., *Hydrophilic/hydrophobic composite shape-shifting structures*. ACS applied materials interfaces, 2018. **10**(23): p. 19932-19939.
13. Lee, Y.B., et al., *Induction of four-dimensional spatiotemporal geometric transformations in high cell density tissues via shape-changing hydrogels*. Advanced functional materials, 2021. **31**(24): p. 2010104.
14. Ding, A., et al., *4D biofabrication via instantly generated graded hydrogel scaffolds*. Bioactive materials, 2022. **7**: p. 324-332.

15. Ding, A., et al., *Jammed micro-flake hydrogel for four-dimensional living cell bioprinting*. Advanced Materials, 2022. **34**(15): p. 2109394.
16. Gugulothu, S.B. and K. Chatterjee, *Visible light-based 4D-bioprinted tissue scaffold*. ACS macro letters, 2023. **12**(4): p. 494-502.
17. K  pyl  , E., S.M. Delgado, and A.M. Kasko, *Shape-changing photodegradable hydrogels for dynamic 3D cell culture*. ACS applied materials interfaces, 2016. **8**(28): p. 17885-17893.
18. Sydney Gladman, A., et al., *Biomimetic 4D printing*. Nature materials, 2016. **15**(4): p. 413-418.
19. Mulakkal, M.C., et al., *Responsive cellulose-hydrogel composite ink for 4D printing*. Materials Design, 2018. **160**: p. 108-118.
20. Lai, J., et al., *4D printing of highly printable and shape morphing hydrogels composed of alginate and methylcellulose*. Materials Design, 2021. **205**: p. 109699.
21. Joshi, A., et al., *4D Printed Programmable Shape-Morphing Hydrogels as Intraoperative Self-Folding Nerve Conduits for Sutureless Neurorrhaphy*. Advanced healthcare materials, 2023. **12**(24): p. 2300701.
22. Kirillova, A., et al., *4D biofabrication using shape-morphing hydrogels*. Advanced Materials, 2017. **29**(46): p. 1703443.
23. Zhang, L., et al., *A biomimetic 3D-self-forming approach for microvascular scaffolds*. Advanced Science, 2020. **7**(9): p. 1903553.
24. Mandal, A. and K. Chatterjee, *Emerging trends in humidity-responsive 4D bioprinting*. Chemical Engineering Journal, 2023. **455**: p. 140550.
25. Zhang, Y., et al., *Differential diffusion driven far-from-equilibrium shape-shifting of hydrogels*. Nature Communications, 2021. **12**(1): p. 6155.
26. Ding, A., et al., *Cell-laden multiple-step and reversible 4D hydrogel actuators to mimic dynamic tissue morphogenesis*. Advanced Science, 2021. **8**(9): p. 2004616.
27. Bajpai, S. and S. Johnson, *Superabsorbent hydrogels for removal of divalent toxic ions. Part I: Synthesis and swelling characterization*. Reactive functional polymers, 2005. **62**(3): p. 271-283.
28. Cooke, M.E. and D.H. Rosenzweig, *The rheology of direct and suspended extrusion bioprinting*. APL bioengineering, 2021. **5**(1).
29. Ahlfeld, T., et al., *Methylcellulose  a versatile printing material that enables biofabrication of tissue equivalents with high shape fidelity*. Biomaterials science, 2020. **8**(8): p. 2102-2110.
30. Villar, G., A.D. Graham, and H. Bayley, *A tissue-like printed material*. Science, 2013. **340**(6128): p. 48-52.

31. Timoshenko, S., *Analysis of bi-metal thermostats*. JOSA, 1925. **11**(3): p. 233-255.
32. Skylar-Scott, M.A., et al., *Voxelated soft matter via multimaterial multinozzle 3D printing*. Nature, 2019. **575**(7782): p. 330-335.
33. Zhang, Y.F., et al., *Fast-response, stiffness-tunable soft actuator by hybrid multimaterial 3D printing*. Advanced Functional Materials, 2019. **29**(15): p. 1806698.
34. Goh, G.L., et al., *3D printing of multilayered and multimaterial electronics: a review*. Advanced Electronic Materials, 2021. **7**(10): p. 2100445.
35. Shiblee, M.N.I., et al., *4D printing of shape-memory hydrogels for soft-robotic functions*. Advanced Materials Technologies, 2019. **4**(8): p. 1900071.
36. Bian, Q., L. Fu, and H. Li, *Engineering shape memory and morphing protein hydrogels based on protein unfolding and folding*. Nature communications, 2022. **13**(1): p. 137.

Research 3

“All-in-one” Ink for Light-based 4D Printing of Conducting, Tough, Anti-freezing, and Cytocompatible Hydrogels

6.1 Introduction

Recently, conducting hydrogels have attracted much interest in the biomedical and biomaterials community to combine flexible and stretchable hydrated polymer structures with intriguing electronic functionalities[1, 2]. These multifunctional materials combining the hydrogel characteristics along with the conductive components, such as electrical conductivity and electrochemical-redox properties, open new opportunities in the biomedical field, such as biosensors[3], soft robotics[4], flexible electronic devices[5], drug delivery[6], tissue engineering[7], health monitors[8], etc. However, conventional preparation techniques such as transfer printing and photolithography are limited to producing simple structural devices[9]. Several constraints of conventional manufacturing tools are increasingly being circumvented by three-dimensional (3D) printing techniques[10-12]. Although there is a limited library of conducting hydrogels reported in the literature, most are not amenable to 3D printing. Digital light processing (DLP)--based 3D printing yields parts of complex design architecture with high accuracy and fidelity necessary to develop and create complex structures[13].

A key limitation of conventional hydrogels is their limited working conditions, such as poor durability for use over extended periods or use in extreme conditions other than ambient conditions, such as low temperatures[14, 15]. Once the temperature falls below the freezing point of water, conventional hydrogels have a strong tendency to freeze. The frozen hydrogels lose their original functionality, including elasticity and conductivity, in the case of a few reported conductive hydrogel formulations, which significantly restricts their practical use in cold environments (such as high altitudes or seasonally low temperatures)[16, 17]. Moreover, typical hydrogels dehydrate rapidly, even at ambient conditions, leading to hardness, distortion, and failure to preserve desirable properties over time. Researchers have developed

organohydrogels that combine an organic solvent with the polymeric network to overcome these challenges[18, 19]. However, organohydrogels typically have poor conductivity at low temperatures, are difficult to polymerize, and are not compatible with DLP-based 3D printing. Organohydrogels are not sufficiently cytocompatible for implantable biomedical applications. Novel polymer formulations based on poly(3,4-ethylenedioxythiophene) (PEDOT), which augments the processability of PEDOT through 3D printing techniques, have been investigated[20, 21]. Recently, it has been demonstrated that PEDOT can undergo copolymerization with various bio-polyesters, such as poly(lactic acid) (PLA) and poly(ϵ -caprolactone) (PCL), resulting in graft copolymers[22, 23]. These copolymers exhibit shear-thinning behavior, making them amenable to direct ink writing (DIW) and show good cytocompatibility. However, these modifications decrease the conductivity and functionality of PEDOT. Therefore, designing multifunctional hydrogels that can withstand freezing and dehydration while maintaining desired mechanical performance, good conductivity, and cytocompatibility, as well as being amenable to additive manufacturing, is a key challenge.

The goal of this study was to design a photocurable and conductive polymer ink based on poly(3,4-ethylenedioxythiophene) polystyrene sulfonate (PEDOT:PSS) intended for processing via DLP-based 3D printing to yield multifunctional hydrogels that can overcome the limitations associated with the current generation of hydrogels. The ink formulations were rationally developed with PEDOT:PSS, acrylamide, synthesized crosslinker pluronic127 dimethacrylate (PF127DMA), and LiCl to impart different properties. The ink was systematically developed based on the processability and mechanical properties of the 3D-printed hydrogels. The properties and performance of the 3D printed hydrogels were characterized for potential application over a wide range of working conditions, such as at

temperatures as low as -80 °C and as high as 45 °C. The inks were explored for their ability to yield shape-morphing 4D-printed hydrogels. The cytocompatibility was assessed for biomedical applications.

6.2 Methods

6.2.1 Synthesis of PF127DMA

Pluronic F127 dimethacrylate (PF127DMA) was synthesized as described in section 2.2.8 of Chapter 2. The formation of the methacrylate group was confirmed by FTIR and ¹H NMR spectroscopy as described in section 2.2.10.1 and 2.2.10.2 respectively, of Chapter 2.

6.2.2 Preparation of conducting hydrogel ink

First, PEDOT: PSS polymer solution was mixed with 13% (v/v) DMSO and 2% (v/v) glycerol. Then, the desired amount of synthesized PF127MA and acrylamide was added to the previously prepared polymer solution and mixed thoroughly until a homogeneous solution was obtained. Then, the desired amount of LiCl was added and thoroughly mixed by vortexing to get a homogenous solution. Subsequently, a consistent volume of 3% (w/v) LAP solution and 30 mM Tartazine solution were incorporated into the mixture before initiating 3D printing. Details of ink compositions are compiled in Table 4- 2.

6.2.3 DLP 3D-printing

Light assisted DLP 3D printing technique was used in this chapter as described in section 2.2.8.2 of Chapter 2.

6.2.4 Characterization of the printed construct

Properties relevant to biomedical applications, such as swelling behavior, degradation studies, water retention, and rheological study, were also performed as described in sections 2.2.10.4, 2.2.10.5, 2.2.10.6, and 2.2.10.9, respectively, of Chapter 2.

6.2.4.1 Mechanical study

Dog-bone structures (15 mm gage length, 4 mm width, 2 mm thickness) were 3D printed to evaluate the mechanical behavior of the printed conducting hydrogel using a universal testing machine (Multitest – 10i, Mechmesin). All measurements of tensile and cyclic loading-unloading were conducted using a 25 N load cell and a displacement rate of 10 mm/min. The engineering stresses (σ) and strain (γ) were calculated using the following equation.

$$\sigma = \frac{F}{A_0}$$

$$\% \gamma = \left(\frac{\Delta l}{l} \right) \times 100$$

F is the applied force, and A_0 is the initial cross-sectional area. l is the gauge length of the dog bone printed hydrogel. Toughness was calculated by evaluating the area under the stress-strain curve, and %Elongation was measured as per the following equation.

$$\% \text{Elongation} = (\% \gamma \text{ at fracture point} - 100)$$

The hysteresis test was performed under various % strain from 20% to 100% at a constant stretching rate of 10 mm/min and immediately unloaded at the same strain speed. Then, the successive loading-unloading test was conducted for 20 cycles at 50% strain. The dissipated

energy was defined as the area in the hysteresis loop encompassing the loading-unloading profile.

6.2.4.2 Dynamic mechanical analysis

The mechanical properties of the printed constructs were assessed using a dynamic mechanical analyzer (DMA Q800, TA Instruments). The fatigue performance of the hydrogels was assessed by DMA by cyclic loading-unloading for 5 cycles under stress of 30 kPa with creep and recovery time of 1 min.

6.2.4.3 Thermogravimetric analysis

The tolerance to dehydration of the hydrogels was determined using thermogravimetric analysis (TGA, (TA Q500). Samples were heated in a nitrogen atmosphere at 5°C / min from 30°C to 300°C.

6.2.4.4 Anti-freezing characteristics

The freezing behavior of the hydrogels was investigated through direct observation and by assessing subsequent deformations. Before testing, the hydrogel samples were subjected to specific temperatures in a freezer for 3 hours. The 3D-printed hydrogel constructs were stored at -80°C for 24 h and then lyophilized using a freeze-dryer (Benchtop Freeze Dryer, Labconco). Then, the freeze-dried samples and as-printed samples were characterized by Fourier transform infrared (FTIR) spectroscopy (Perkin-Elmer Frontier IR/NIR systems) in attenuated total reflection (ATR) mode.

6.2.4.5 Differential scanning calorimetry

For differential scanning calorimetry (DSC), samples (5–10 mg) were sealed in an aluminum pan and then cooled at 5 °C/min to – 80°C from 25°C under a nitrogen atmosphere. After an isothermal period of 30 min, the samples were heated from -80°C to 50 °C at 5 °C/ min.

6.2.4.6 Characterization of electrical properties

Conductivity was calculated by measuring resistance using a standard four-point probe head. Reported values reflect an average over a minimum of three measurements obtained for each condition. Furthermore, frequency-dependent AC conductivity of the printed constructs was measured on disks (diameter of 15 mm and thickness of 1.5 mm) via an Alpha-N analyzer, Novocontrol (Germany), with V_{rms} at 1 V in a wide frequency range of 0.1 Hz to 10 MHz.

Electrochemical impedance spectroscopy (EIS) studies were carried out to evaluate the ionic conductivity using an electrochemical workstation (CHI604E, C.H. instruments) operated in the frequency range from 0.1 Hz to 10^6 Hz, and data were fitted with the model circuit to evaluate the value of the characteristic parameter.

6.2.5 Motion sensing performance tests

A parameter analyzer (Keysight B1500A semiconductor device analyzer) unit was used to collect signals from the hydrogel motion sensor. The 40% LiCl hydrogel was attached to the movement site (e.g., the finger or wrist), and crocodile clips were used to connect the hydrogel to the probe of the analyzer. The assembled hydrogel sensor was then employed to monitor motion signals. The relative resistance change was calculated using the following formula:

$$\frac{\Delta R}{R_0} = \frac{R - R_0}{R_0}$$

Where R_0 refers to the initial resistance, and R refers to the resistance upon applied strain or the bending of the finger or wrist.

6.2.6 4D printing

Mechanical peeling from the build platform was performed very gently to assess the free-form deformation of the printed constructs and digital images were captured to quantify the extent of deformation. Subsequently, to evaluate the programmability of structural deformation, the printed construct was submerged in water and allowed to swell further. Following this, the samples were immersed in ethanol and then again in water to evaluate the programmability and retention of free-form deformation of the printed constructs.

6.2.7 Cytocompatibility

L929 mouse fibroblast cells were used in this study and cultured and proliferated as described in section 2.2.11 of Chapter 2. Then, cells were exposed to hydrogel as follows.

1×10^4 cells were seeded in individual wells of 24-well plates and allowed to adhere and proliferate in fresh medium for 36 hours. Following this incubation period, an equal volume of printed hydrogel constructs for each experimental condition was introduced into the respective wells, and cells were further cultured to evaluate the cytotoxicity of the printed hydrogel materials (as shown schematically in Figure 4- 8 a). The 3D-printed constructs were pre-washed in phosphate-buffered saline (PBS) overnight prior to being placed in contact with the cells within the well plates.

Then, the cytocompatibility was evaluated by Alamar blue assay, Live-dead assay, and F-actin and nucleus staining as described in sections 1.1.9.1, 1.1.9.2, and 1.1.9.3, respectively.

6.3 Results

6.3.1 PF127DMA synthesis

Pluronic F127 dimethacrylate (PF127DMA) were synthesized from precursor polymers PF127, as illustrated in Figure 4- 1 a. The successful methacrylation of PF127 was confirmed by ^1H NMR and FTIR spectroscopy. The signals of proton nuclear magnetic resonance (^1H NMR) found at 1.8, 5.7, and 6.0 ppm confirmed the insertion of methacrylic groups on the chain ends of Pluronic F127, as shown by the numerical peak assignment to the chemical structure (Figure 4- 1 c). Additionally, the FTIR spectra showed characteristic vibration bands for the $-(\text{C}=\text{O})\text{O}$ ester group at 1716 cm^{-1} , which further confirmed successful methacrylation (Figure 4- 1 b).

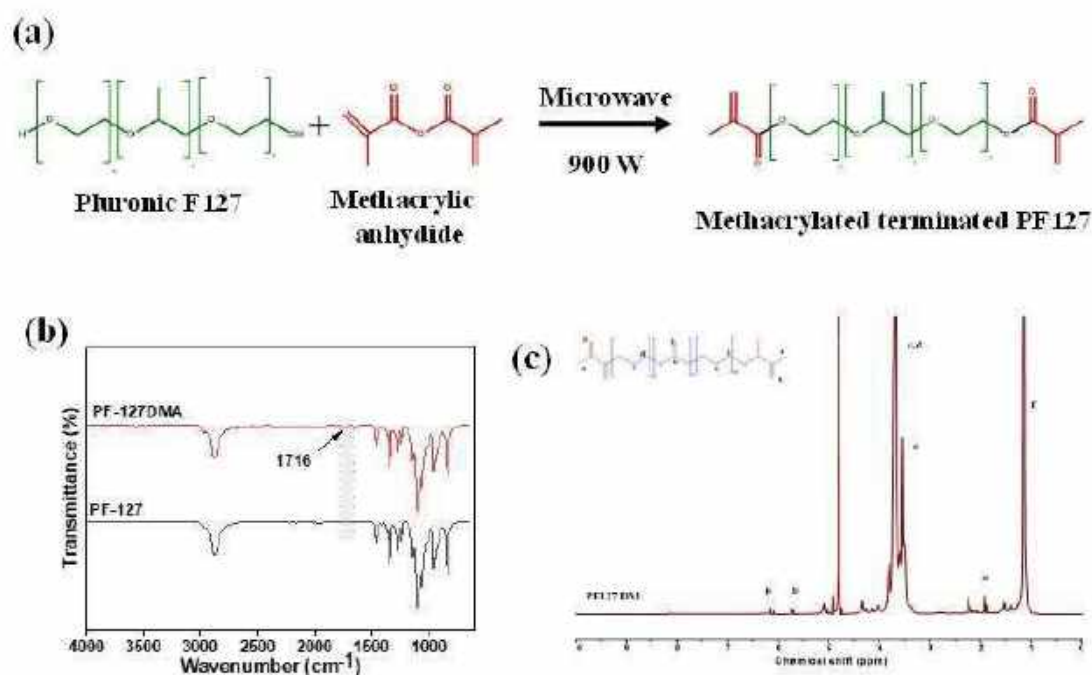


Figure 4- 1: (a) schematic representation of synthesized PF127DMA; (b) FTIR spectra of PF127 and PF127DMA; (c) NMR spectra of PF127DMA

6.3.2 Design strategy and printing technique of the conducting ink

A scheme of the formulation of the polymeric photoink and fabrication strategy to yield 3D-printed conductive hydrogel is presented in Figure 4- 2. A conducting photoink was rationally formulated by incorporating dispersions of PEDOT: PSS in an aqueous solution of low polymer content of approximately 1.1 wt% (11 mg mL^{-1}) as primary network matrix, acrylamide (AM) as a monomer of the secondary network, synthesized PluronicF127 dimethacrylate (PF127DMA) as a crosslinker (Figure 4- 1), lithium phenyl-2,4,6-trimethylbenzoylphosphinate (LAP) as a water-soluble photoinitiator, and tartrazine as a photo absorber to increase the resolution of the printing. The details of ink compositions and ink-development process are compiled in Table 4- 2, and shown schematically in Figure 4- 2 a, respectively. Glycerol and DMSO were added in small quantities to the ink as a solvent doping treatment of PEDOT: PSS aqueous solution for increased conductivity. It was envisaged that their presence would enhance the step separation between PEDOT and PSS and allow the linear orientation of the PEDOT chains[24]. LiCl was added to the ink to impart the anti-freezing property to enable applications in extremely cold environments, which is a key bottleneck of the current hydrogels. The photoink was then processed with a DLP-based 3D printer to additively manufacture conductive hydrogels of intricate geometries (refer Figure 4- 2 (b-d)) and, subsequently, along pre-programmed paths to yield shape-morphing 4D-printed parts.

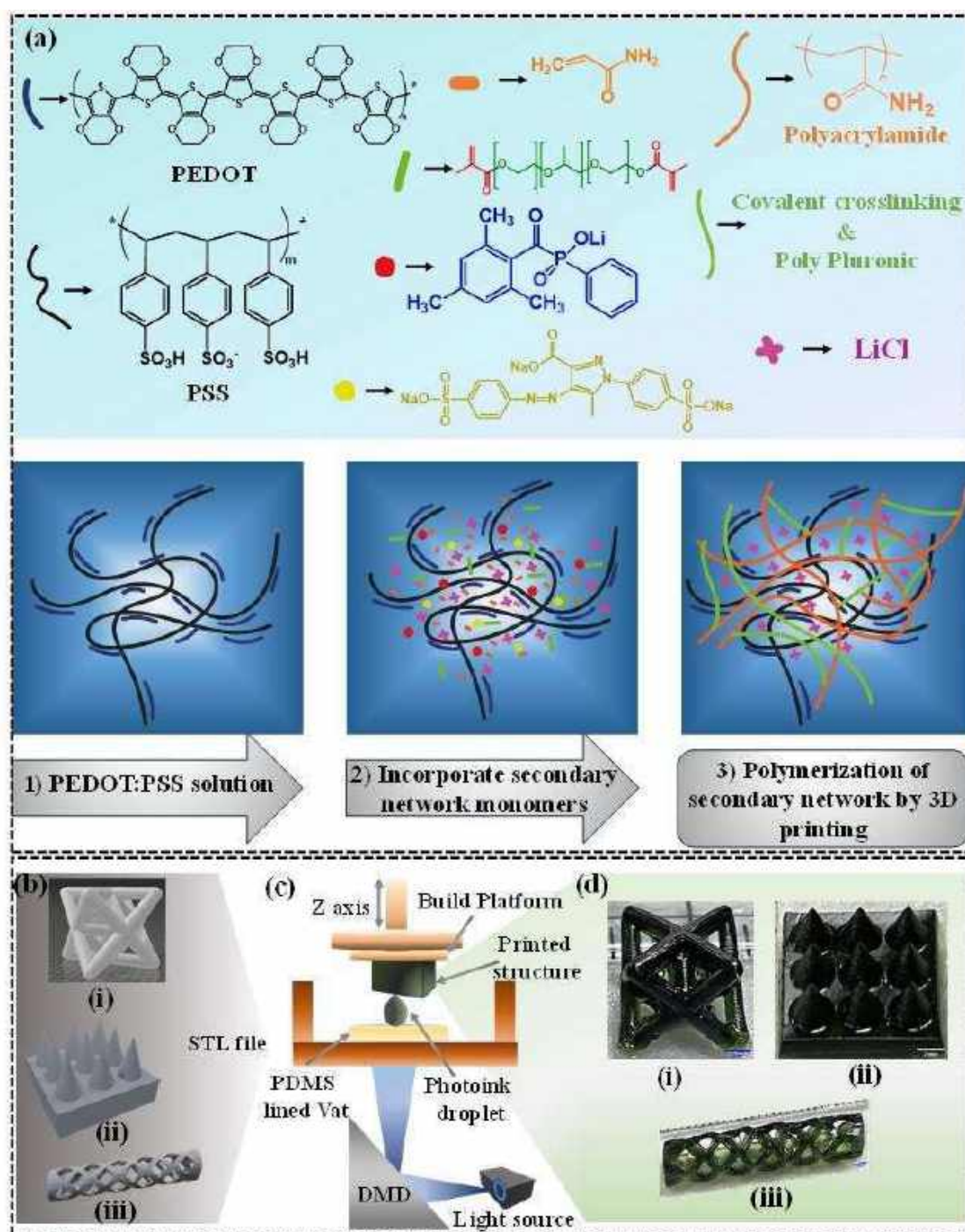


Figure 4- 2: Ink composition and fabrication process to prepare conducting interpenetrating network hydrogels. (a) Scheme for formulating an ink for fabricating conducting hydrogels. First, aqueous solutions of PEDOT: PSS were prepared using DMSO and glycerol to screen

the electrostatic repulsions between PEDOT and PSS. Next, the PEDOT: PSS solution was infiltrated with acrylamide, PF127DMA, LiCl, Tartrazine, and LAP. Finally, the polyacrylamide network crosslinked with PF127DMA plus poly pluronic was formed by polymerizing the monomers via DLP-based 3D printing technique; (b) STL file of different parts of complex geometry (i) octet-truss, (ii) fine needles, and (iii) a biostent; (c) Scheme demonstrating layer-by-layer fabrication by blue light (405 nm) using a DLP-based 3D printer; (d) digital photographs of the 3D-printed parts corresponding to the STL files in (b) (scale bar is 2 mm).

During the printing process, the patterned (as per STL files) 405 nm blue light tailored by a digital micromirror device (DMD) was projected onto the surface of the hydrogel precursor solution to stimulate localized photopolymerization by opening the double bonds on the acrylate functional groups on both the acrylamide and PF127DMA to form permanently crosslinking network and solidified hydrogel structured on the build platform (Figure 4- 2 (b, c)). Layer-by-layer solidification continued by moving the platform upwards until the entire prepatterned hydrogel structure was fabricated. Therefore, programmable 3D objects can be tailored for their structures and functionalities, executing rapid device fabrication without requiring additional steps such as adhesion or assembly. Figure 4- 2 d displays the digital image of the printed structure after removing it from the build plate, which shows the high fabrication precision of our developed ink by using DLP-based 3D printing technique, validated by a printed octet-truss, fine needles, and a biostent (Figure 4- 2 d (i, ii, iii)). They exhibit complexities rivaling or exceeding the challenges of 3D printing the conducting polymer hydrogels.

6.3.3 Mechanical properties of the 3D-printed hydrogels

The presence of photopolymerizable acrylamide monomers and the crosslinker PF127DMA in the ink formulation enables chemically crosslinked hydrogels upon exposure to visible light (405 nm) in the presence of LAP, the photoinitiator, yielding an interpenetrating physical network with the PEDOT: PSS chains. The mechanical properties of the 3D-printed conducting hydrogels can be tailored by tuning the composition of the precursor solutions. To elucidate the tunability of the mechanical characteristics of the hydrogel, we performed tensile tests on hydrogels prepared from different ink compositions (Figure 4- 3). Initially, we studied the effect of monomer concentration on the mechanical properties of the printed conducting hydrogels by varying monomer concentration from 10 wt% to 50 wt% at fixed concentrations of other components and parameters (details in Table 4- 2). It was observed that increased acrylamide content in the ink resulted in a remarkable increase in stretchability, as evidenced by the increased elongation of the 3D-printed hydrogels. Concurrently, fracture strength and toughness exhibited an upward trend with increasing acrylamide content in the ink (Figure 4- 3 (a, d)). With the increase in acrylamide content, the length of the acrylamide polymer chains increases and forms more entanglements with the polymer network, leading to more % elongation (% EL) and toughness in the hydrogel systems. The highest % EL ($\approx 415\%$) was observed for 50 wt % acrylamide concentration. However, the maximum fracture strength (FS, ≈ 20 kPa) and toughness (TS, ≈ 49.5 kJ/m³) were observed at 40 wt% acrylamide with a marginal drop at 50 wt%. It is likely that increased agglomeration due to more entanglements and hydrogen bonding in 50% acrylamide than in 40% led to these observed trends. Thus, the acrylamide content was fixed at 40% for subsequent studies.

Next, we varied the PF127DMA content from 0.5 wt% to 16 wt% to understand the effect of the crosslinker concentration in the 40% acrylamide ink on the mechanical properties of the 3D-printed hydrogels. It was observed that the hydrogels exhibited lower stretchability but relatively higher fracture strength with an increase in the PF127DMA content in the ink (Figure 4- 3 (b, e)). The 3D-printed hydrogel with 0.5 wt% PF127DMA could easily be elongated to nearly 10 times its original length (%EL \approx 960%), whereas it was around 1.6 times for 16 wt% PF127DMA (% EL \approx 50%). With increased PF127DMA content for a given acrylamide concentration, crosslinking points amongst the acrylamide polymer chains increase, leading to the formation of a denser network. Moreover, PF127DMA chains can also form crosslinks between themselves, further enhancing the crosslinking density in the hydrogel. Together, both these phenomena contribute toward lower elongation and higher fracture strength. Notably, the gels at low crosslinker content were weak and prone to rupture and damage while handling. For a good combination of strength, toughness, and handling of the 3D-printed hydrogel, further studies were performed with inks of 40 wt% acrylamide and 16 wt% PF127DMA (hereafter, this composition is denoted as WO LiCl, wherein WO means without). The FS and TS of this hydrogel are \approx 112 kPa and \approx 109 kJ/m³, respectively.

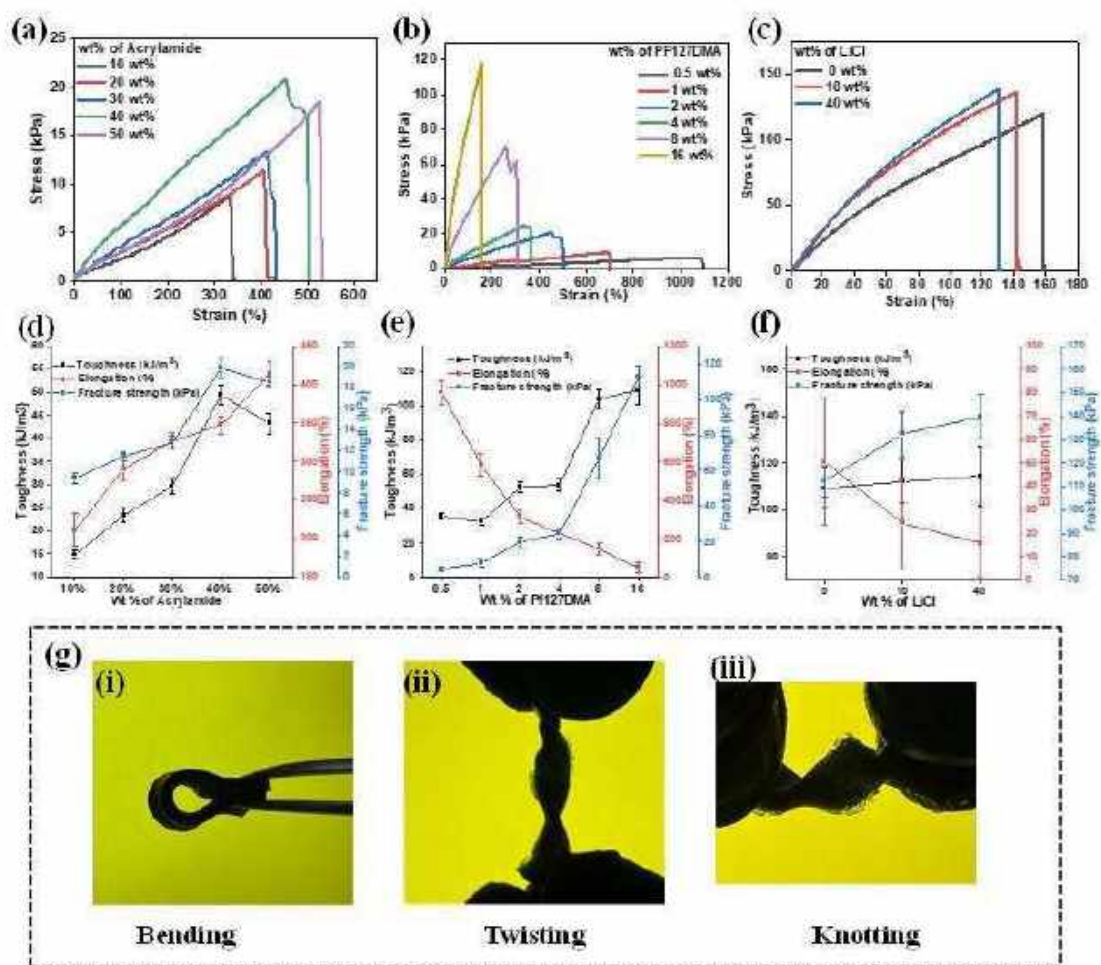


Figure 4- 3: Mechanical characterization of the printed hydrogel prepared from inks of various compositions. (a-c) Tensile stress-strain curves of gels with different contents of (a) acrylamide monomer, (b) PF127DMA crosslinker, (c) LiCl. Plots of toughness, fracture strength, and % elongations from corresponding stress-strain curves for varying contents of (d) acrylamide monomer, (e) PF127DMA, and (f) LiCl. (g) Digital images under various mechanical deformation of the printed constructs (i) Bending, (ii) twisting, (iii) knotting.

Further, we investigated the effect of LiCl addition on the mechanical properties of the fabricated hydrogel. We characterized gels at a lower (10 wt%, hereafter denoted as 10% LiCl)

and a higher (40 wt%, hereafter denoted as 40% LiCl) concentration of LiCl in the ink comprised of 40 wt% acrylamide and 16 wt% PF127DMA (Figure 4- 3 (c, f)). The elongation of the 3D-printed hydrogels marginally decreased ($\% \text{ EL} \approx 24\%$ and $\approx 16\%$ for 10% and 40% LiCl, respectively), and fracture strength marginally increased ($\text{FS} \approx 132 \text{ kPa}$ and $\approx 139 \text{ kPa}$ for 10% and 40%, respectively) with an increase in LiCl concentration. This trend is attributed to the likely occurrence of intermolecular hydrogen bonding after introducing LiCl in the ink. However, the presence of LiCl did not yield statistically significant differences in the toughness of the printed hydrogel ($\text{TS} \approx 112 \text{ kJ/m}^3$ and $\approx 114 \text{ kJ/m}^3$ for 10% and 40%, respectively). Additionally, the printed hydrogel demonstrates resilience to various forms of deformation, including bending, twisting, and knotting, which confirms its inherent flexibility (Figure 4- 3 (i-iii)).

Furthermore, examining the energy dissipation and fatigue resistance of the printed conductive hydrogels under stress is essential for long-term use in devices subjected to repeated mechanical stresses. Thus, the hysteresis energy behavior of these hydrogels was assessed via cyclic tensile loading-unloading tests. The hysteresis loop was indicative of the energy dissipated by the hydrogel during loading-unloading cycles. First, the hysteresis loop of the hydrogels was investigated through a single loading and unloading cycle across diverse strain conditions (Figure 4- 4 (a - f)). It was observed that energy dissipation by the printed hydrogels is minimal. However, as the tensile strain escalated from 20% to 100%, a slight rise in the energy dissipation of the hydrogels was observed. Specifically, for the WO LiCl hydrogel, the dissipated energy increased from $\approx 0.07 \text{ kJ/m}^3$ to $\approx 1.89 \text{ kJ/m}^3$, whereas for the 10% LiCl hydrogel, it increased from $\approx 0.05 \text{ kJ/m}^3$ to $\approx 1.98 \text{ kJ/m}^3$, and for the 40% LiCl hydrogel, it increased from $\approx 0.04 \text{ kJ/m}^3$ to $\approx 2.09 \text{ kJ/m}^3$ (Figures 4- 4 (a - c)). These marginal increases in

energy dissipation at higher strains between the hydrogels were probably due to the presence of the ions in the ink and the loss of ion coordination linking points and hydrogen bonds in the 3D network when loaded. However, no statistically significant differences were observed among the three hydrogel systems.

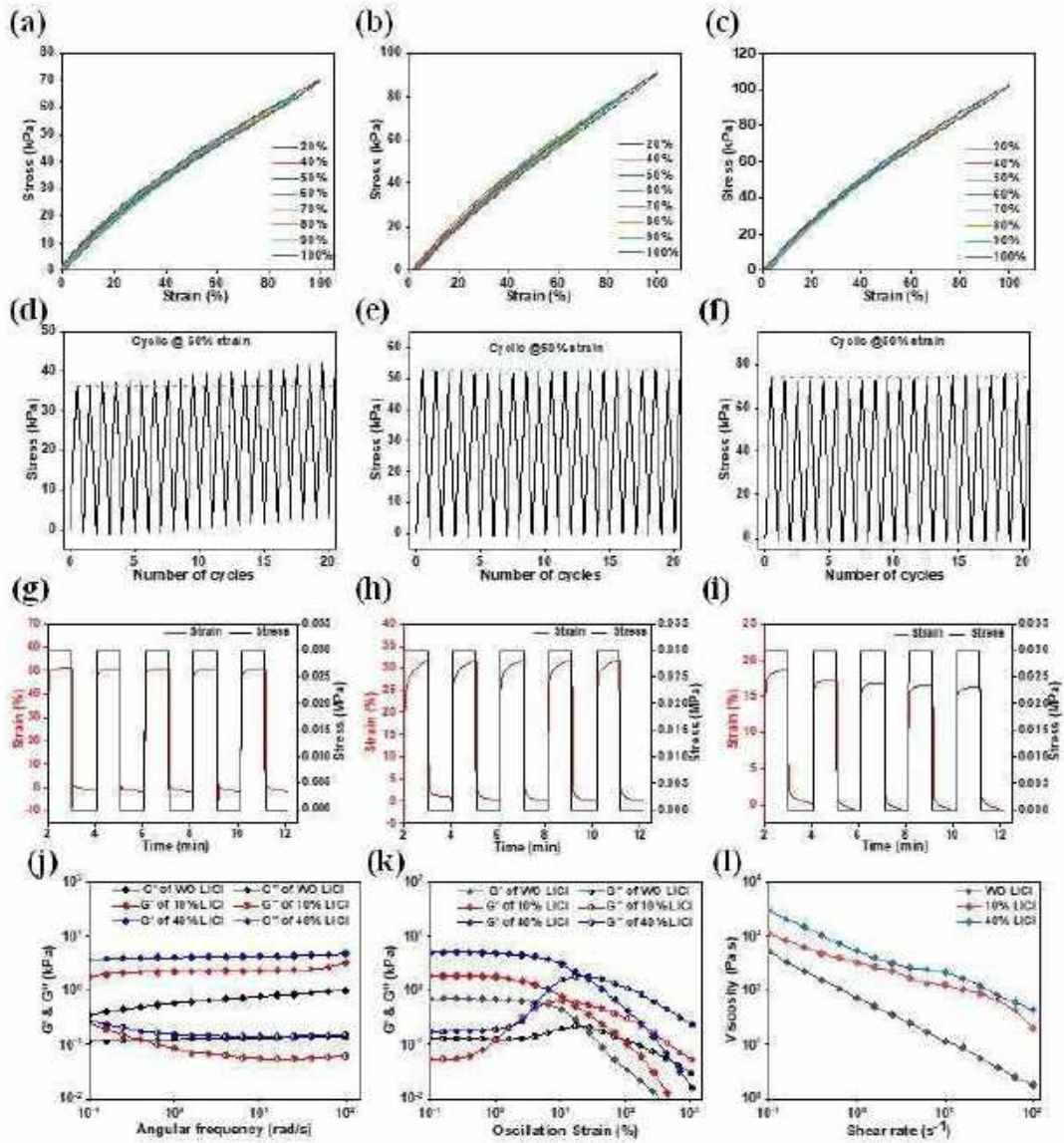


Figure 4- 4: Characterization of fatigue resistance and durability of the 3D-printed hydrogels.

(a-c) The loading-unloading curves of hydrogels under different tensile strains from 20% to

100% of (a) WO LiCl, (b) 10% LiCl, and (c) 40% LiCl. (d-f) The cyclic tensile curve at 50% strain for 20 consecutive cycles of (d) WO LiCl, (e) 10% LiCl, and (f) 40% LiCl hydrogels. (g-i) Dynamic mechanical analysis of the 3D-printed gels to assess fatigue performance and shape-recovery of (g) WO LiCl, (h) 10% LiCl, and (i) 40% LiCl. (j-l) Rheological characterization of the 3D-printed hydrogels: (j) angular frequency sweep from 0.1 to 100 rad s⁻¹ at 0.5% strain, (k) strain amplitude sweep from 1 to 1000% strain at a fixed angular frequency of 10 rad s⁻¹, (l) viscosity measurement with the shear rate variable from 0.1 to 100 s⁻¹.

Furthermore, hysteresis loops of the aforementioned hydrogels were assessed over 20 consecutive loading and unloading cycles at a 50% tensile strain to elucidate the durability and fatigue characteristics of the printed hydrogel structure. It was observed that WO LiCl hydrogel showed slight changes in stress with increasing the number of cycles, whereas no significant changes were observed for 10% LiCl and 40 % (Figure 4- 4 (d - f)). The likely cause of this trend is the water loss from the hydrogel in the case of WO LiCl hydrogel, which makes it stiffer. In the case of 10% and 40% LiCl hydrogel systems, ion-water interactions are induced by Li ions, contributing to an increased stability of the hydrogels over time. However, all hydrogels exhibited a minor decrease in dissipated energy as the number of cycles increased. The WO LiCl hydrogel dissipated energy from 0.57 kJ/m³ to 0.26 kJ/m³, whereas 0.82 kJ/m³ to 0.13 kJ/m³, and 0.73 kJ/m³ to 0.47 kJ/m³ for the 10% LiCl and 40% LiCl hydrogels, respectively (Figure 4- 4 (d-f)). This suggests that elastic deformation occurs rather than plastic deformation in response to applied strains over time. Nevertheless, the hysteresis loops in the subsequent 20 cycles were nearly overlapping, signifying minimal energy dissipation in the hydrogel. Furthermore, the loading curve throughout the cycle predominantly attained the

maximum stress–strain point from the preceding cycle, indicating excellent fatigue resistance characteristics of the hydrogels.

Further, the strain recovery performance of the hydrogel was explored using DMA through five consecutive cyclic loading-unloading cycles with a creep and recovery time of 1 minute under the application of a 30 kPa load (Figure 4- 4 (g - i)). Each hydrogel maintained the corresponding strain upon loading tensile stress of 30 kPa, which recovered more than 95% immediately after unloading and recuperated 100% within 1 minute of unloading the stress. Following five consecutive loading-unloading cycles, the hydrogels retained their structural integrity and manifested a complete recovery of 100%, showcasing robust fatigue resistance and negligible delay in strain recovery. Hence, these findings indicate that hydrogels of this nature hold promise as potential candidate materials for engineering strain sensors in biomedical applications.

6.3.4 Rheological behavior of hydrogels

Rheological studies of hydrogels are essential to characterize the viscoelastic nature of the hydrogels. The dynamic storage modulus (G') and loss modulus (G'') were measured via frequency (ω) and amplitude sweeps. First frequency sweeps were performed, and it was observed that G' (elasticity) is greater than G'' (viscosity) and $\tan \delta (G''/ G') < 1$ within the angular frequency range from 0.1 to 100 rad/s for all three hydrogels (Figures 4- 4 (j)). The storage modulus, G' , increased in the presence of LiCl in the ink, with the following trend: $G'(\text{WO LiCl}) < G'(10 \text{ LiCl}) < G'(40\% \text{ LiCl})$. These results indicate the existence of an entanglement network and a robust elastic gel 3D network, signifying the predominance of the elastic behavior over the viscous nature of the hydrogels. From the frequency sweeps, we selected 10 rad/s to perform the amplitude sweep to understand the linear viscoelastic region

(LVR) and the working windows of the printed hydrogel structures. It was observed that G' of all three hydrogels did not deviate more than 5% of its initial value, up to 5% of oscillation strain, indicating the LVR region of the hydrogel (Figure 4- 4 k). Subsequently, G' of the hydrogels declined quickly and crossed G'' , representing the gel-to-sol transition point and indicating the failure of the hydrogels to a quasi-liquid sol state. In the LVR region, a similar trend of G' was observed as per frequency sweep among the hydrogels, and the cross-over point of the hydrogels did not significantly change in the presence of LiCl. To further understand the viscoelastic nature of the printed hydrogel, viscosity with the shear rate was performed in the range of 0.1 to 100 s^{-1} (Figure 4- 4 (l)). The viscosity of 40% LiCl is higher, followed by 10% LiCl and WO LiCl hydrogel. However, the viscosity of the hydrogels decreased with an increasing shear rate for all three hydrogels, and the hydrogels demonstrated non-Newtonian shear thinning characteristics that are advantageous for biomedical applications. These rheological behaviors exhibited by the hydrogels are characteristics of viscoelastic materials.

6.3.5 Anti-freezing property and dehydration tolerance ability of the hydrogel

Due to the phenomenon of water crystallization, conventional conductive hydrogels exhibit a high propensity to freeze and harden at sub-zero temperatures, thereby limiting their application in cold working conditions. Therefore, the resistance to freezing at extremely low temperatures is a noteworthy feature of interest. Here, we studied the tolerance of these hydrogels to freezing and dehydration. We initially assessed the physical state of the hydrogels at low temperatures based on visual observations of their texture and flexibility (Figure 4- 5 (a, b)). The WO LiCl 3D-printed hydrogel solidified, forming frozen solids, at temperatures below 0°C, and hydrogel became hard, brittle, and white after freezing with nearly no flexibility (Figure 4- 5 b). In contrast, the 10% LiCl hydrogel solidified only at temperatures below -20°C,

whereas the 40 % LiCl hydrogel did not freeze even at -80°C , remaining visibly unchanged (Figure 4- 5 (a, b)). This observation is corroborated by FTIR and DSC measurements. The 3D-printed hydrogel samples were lyophilized for 48 h, and the FTIR spectra of the as-printed and lyophilized samples were assessed to understand the anti-freezing behavior. As expected, the spectra revealed prominent water molecule peaks in the 3000 cm^{-1} to 3600 cm^{-1} range in all three as-printed hydrogels, (Figure 4- 5 c). On the other hand, in the case of lyophilized samples, no discernible water molecule peak was detected for WO LiCl hydrogel after 48 h of lyophilization. Notably, 10% LiCl lyophilized samples displayed a diminished water molecules peak, whereas the 40% LiCl counterpart exhibited an intense peak of water molecules similar to the as-printed samples (Figure 4- 5 c). These findings imply that water molecules within the WO LiCl hydrogel system freeze at -80°C and are subsequently removed during lyophilization. However, in the case of 10% LiCl, partial freezing and loss of water molecules occurred during freezing at -80°C and lyophilization. In contrast, due to its excellent anti-freezing properties, the hydrogel with 40% LiCl experienced no loss of water during lyophilization.

These results were further validated by DSC thermograms (Figure 4- 5 (d, e)). During cooling, the exothermic peak of WO LiCl appeared at -43.3°C , indicating that it froze at such a temperature. For 10% LiCl, the exothermic peak was shifted to -51.6°C , indicating a decrease in freezing point and an improvement in frost resistance. Remarkably, the absence of an exothermic peak was noted for the 40% LiCl printed hydrogel system even upon cooling to -80°C , signifying its complete prevention of water freezing within the hydrogel. This observation underscores the hydrogel's exceptional frost resistance capability, extending down to -80°C . (Figure 4- 5 d). A comparable trend was also evident in the heating curve of the 3D printed hydrogels as temperatures increased from low temperatures, as depicted in Figure 4- 5

e. Upon heating from -80°C , the exothermic peak associated with the melting of ice crystals within the hydrogel was observed at -19.7°C for WO LiCl and at -23.2°C for the 10% LiCl hydrogel. In contrast, no endothermic peak was discerned for the 40% LiCl hydrogel, indicating the absence of ice crystals due to the anti-freezing properties of the hydrogel (Figure 4- 5 e). The outstanding anti-freezing properties of the hydrogel stem from the presence of LiCl in the ink. During freezing, water molecules form hydrogen bonds between themselves, assembling into a crystal lattice. However, in the case of the LiCl-containing hydrogels, Li^{+} and Cl^{-} ions facilitate strong binding between water molecules within the hydrogel network (Figure 4- 5 f). This binding disrupts intermolecular interactions amongst water molecules, thereby impeding the formation of requisite hydrogen bonds and disrupting the bonding network necessary for ice crystal formation. This effectively suppresses ice formation even at temperatures as low as -80°C [25, 26].

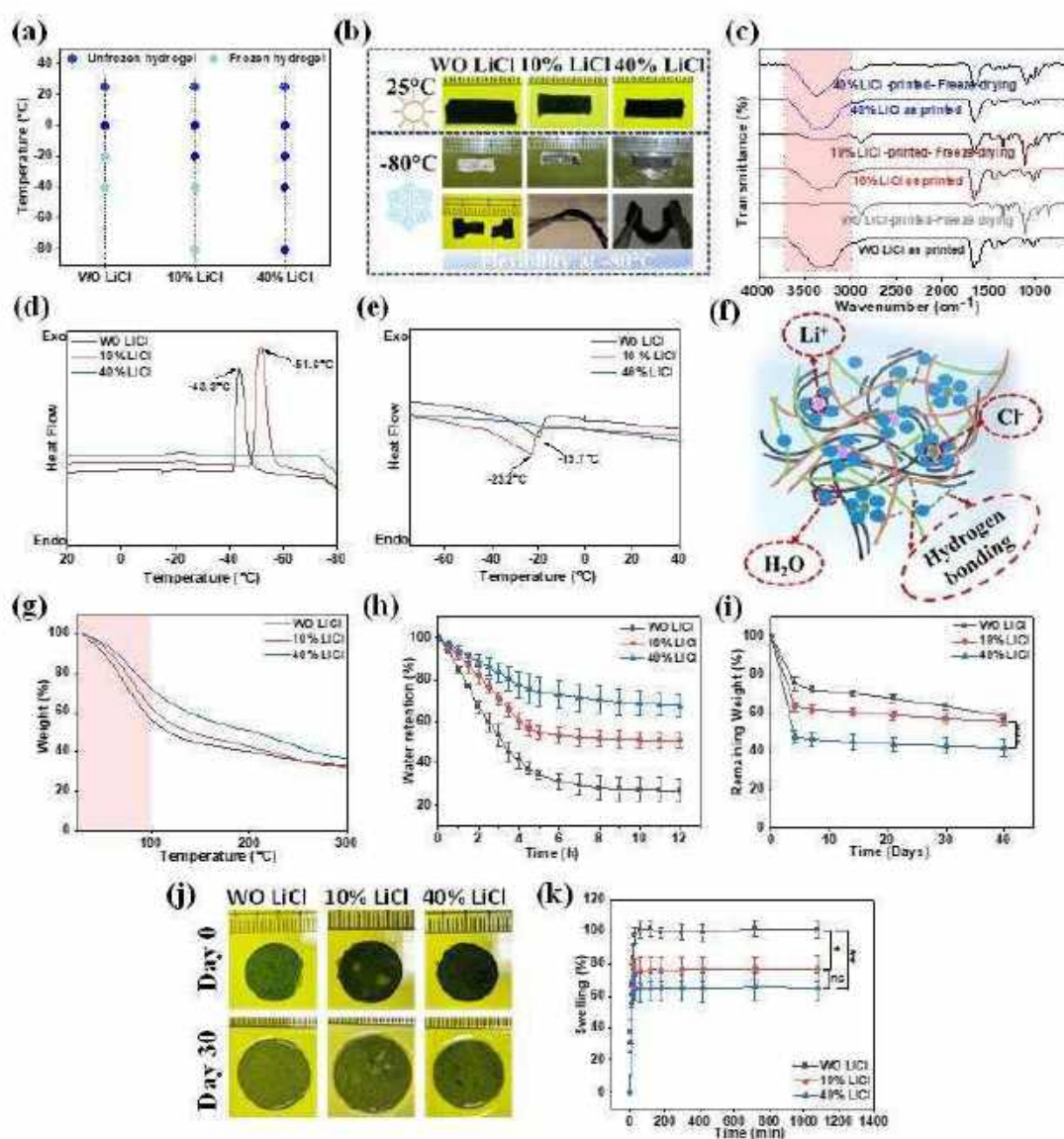


Figure 4- 5: Characterization of anti-freezing and water retention characteristics of the 3D-printed WO LiCl, 10% LiCl, and 40% LiCl hydrogels: (a) Schematic phase diagram revealing frozen and non-frozen conditions at different temperatures. (b) Digital images of the physical appearance and various mechanical deformations of the hydrogels at 25°C and after cooling to -80°C. (c) FTIR spectra of the as-printed and lyophilized hydrogels for 48 h. (d-e) Differential scanning calorimetry (DSC) thermograms for (d) cooling curve (e) heating curve. (f)

Thermogravimetric analysis (TGA) to evaluate the water retention properties of the hydrogels. (g) Quality retention rate curves of hydrogels placed in an oven at 45°C. (h) Degradation profiles and (i) swelling profiles of the hydrogels in PBS at 25° C

In addition, hydrogels typically exhibit low water retention capacity, which significantly curtails their operational lifetime in practical applications. Hence, the dehydration tolerance exhibited in high-temperature environments emerges as a significant characteristic of interest for hydrogels. The thermal stability of 3D-printed hydrogels was initially investigated using TGA (Figure 4- 5 g). The WO LiCl hydrogel exhibited $\approx 44\%$ weight loss in the temperature range of 30°C to 100°C, predominantly due to water evaporation from the hydrogel matrix. This phenomenon was reduced to $\approx 38\%$ in the 10% LiCl hydrogel and $\approx 28\%$ in the 40 wt% LiCl hydrogels, indicating a remarkably augmented dehydration tolerance owing to the presence of LiCl. This enhanced dehydration tolerance was further corroborated through physical observation by placing the hydrogels in the oven at 45°C, and weight was recorded every 30 minutes (Figure 4- 5 h). The mass retention of the hydrogel in the oven for 12 h increased with the incorporation of LiCl in the gel. The quality water retention rate of WO Li, 10% LiCl, and 40% LiCl hydrogels is $\approx 27\%$, $\approx 51\%$, and $\approx 67\%$, respectively. Indeed, the quality of the retention rate improves with an increase in LiCl content in the hydrogel. LiCl enhances the interaction with water molecules, leading to a decrease in the proportion of free water and an increase in bound water within the hydrogel network, consequently reducing water evaporation²⁵. This exceptional anti-freezing capability and water retention efficacy exhibited by the hydrogels render them highly adaptable to various environmental conditions and remarkably stable. This expanded functionality of the hydrogels presented here

significantly broadens the scope of their applications in extreme conditions compared to most hydrogels currently available.

6.3.6 Degradation and swelling properties of hydrogels

The underwater stability of the printed hydrogel structures is essential for applications requiring prolonged use. Therefore, the mass loss of the hydrogels was evaluated with time upon immersion in PBS to investigate the structural stability of the 3D-printed hydrogel constructs (Figure 4- 5 i). It was observed that all three hydrogels demonstrated sharp weight loss initially in the first 4 days. Near 75% of the weight remained for the WO LiCl hydrogel system after 4 days of immersion, whereas $\approx 63\%$ and $\approx 47\%$ remained for 10% LiCl and 40% LiCl hydrogel systems, respectively. After that, the degradation rate was minimal, and the remaining weight of WO LiCl after 40 days was $\approx 58\%$, whereas $\approx 55\%$ and 41% for 10% LiCl and 40% LiCl hydrogels, respectively. The initial weight loss is due to the loss of uncrosslinked acrylamide monomers, uncrosslinked PF127DMA, excess LiCl salt, and photo absorber from the hydrogel matrix. Thereafter, the loss is likely due to diffusing out of the secondary matrix of PEDOT: PSS and the mild degradation of the PF127DMA crosslinker in the hydrogel network. In the 40% LiCl hydrogel, degradation is more due to additional leaching out of the excessive LiCl from the hydrogel matrix. However, after 30 days of immersion, all 3D-printed constructs remained intact and amenable to easy handling (Figure 4- 5 j).

The extensive swelling observed in -conducting hydrogels prepared conventionally via casting methods restricts their utility, particularly in bioelectrochemical and biosensing domains. The swelling behavior of our 3D-printed hydrogels was assessed after immersing them in PBS (Figure 4- 5 k). It was observed that maximum swelling was reached within 60 minutes. The % swelling of the WO LiCl hydrogel is $\approx 100\%$, whereas about $\approx 73\%$ and $\approx 65\%$ for 10%

LiCl and 40% LiCl, respectively. The swelling ratio is higher for the WO LiCl hydrogel system than for the gels with LiCl. The total polymer content is higher in WO LiCl, which leads to a more accessible functional group in the hydrogel matrix, leading to more swelling. Meanwhile, due to the presence of LiCl in the hydrogel system, the polymer content is comparatively lower. Additionally, the functional groups of the polymer interact with Li^+ & Cl^- ions and water molecules within the hydrogel network, which leads to less accessibility of available functional groups to hold new water molecules in the matrix, leading to less swelling.

6.3.7 Conductivity and electrochemical properties of hydrogels

Characterizing the electrical behavior of the 3D-printed conducting hydrogel is vital for its use in many emerging applications, such as bioelectronics and wearable devices. First, the electrical conductivity of hydrogels was calculated by measuring the resistance of the 3D-printed hydrogel by the four-point probe method (Figure 4- 6 a). The conductivity of the WO LiCl hydrogel is $\approx 0.04 \text{ S m}^{-1}$, whereas $\approx 1.22 \text{ S m}^{-1}$ and 3.57 S m^{-1} for 10% LiCl and 40% LiCl hydrogels, respectively. In the case of WO LiCl, conductivity primarily originates from the interpenetrating network of the PEDOT: PSS polymers within the hydrogel network. The conductivity is enhanced in the presence of LiCl, with a 30-fold increase observed for the 10% LiCl hydrogel system and an 89-fold increase for the 40% LiCl hydrogel system. This increase is due to the synergistic effect of the PEDOT: PSS polymer and the Li^+ and Cl^- ions within the hydrogel matrix, facilitated by the strong interaction between the polymer matrix and the ions. Apart from the four probe methods, the frequency-dependent bulk conductivity of printed structures was also measured (Figure 4- 6 b). A similar trend of increasing conductivity with an increase in LiCl content was also observed here. However, 10% LiCl and 40% LiCl hydrogels showed a frequency-independent plateau at lower frequencies, suggestive of the

charge transfer mechanism in multiphasic systems due to PEDOT: PSS matrix phase and Li^+ and Cl^- ions.

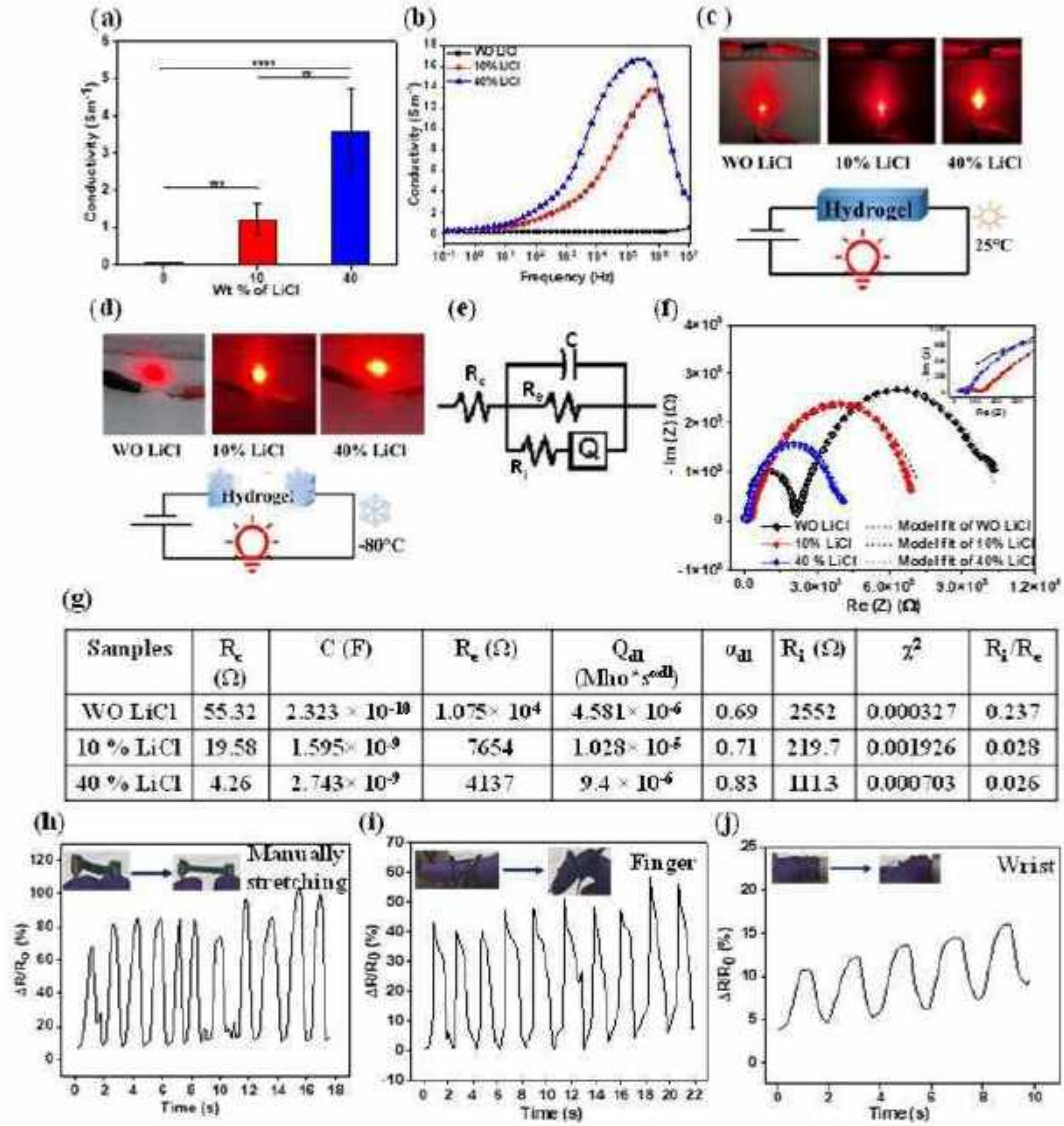


Figure 4- 6: Conductivity and electrochemical characterization of WO LiCl, 10% LiCl, and 40% LiCl 3D-printed hydrogels: (a) Conductivity values of the 3D-printed hydrogel structures were calculated by measuring resistance using a standard four-point probe head. Data are plotted as mean \pm S.D. for $n = 3$. Ordinary one-way ANOVA with Tukey's multiple

comparisons test was performed for (a). ** indicates $p < 0.01$, *** indicates $p < 0.001$, **** $p < 0.0001$. (b) AC electrical conductivity of the hydrogels as a function of frequency. Demonstration of the printed hydrogels functioning as conductors at (c) 25°C and (d) –80°C. (e) Equivalent circuit model representation for fitting the electrochemical impedance spectroscopy (EIS) curve of the hydrogels. R_c , R_e , and R_i represent the solution resistance, charge transfer resistance, and ionic resistance, respectively. C represents the double-layer capacitance. Q represents the constant phase element (CPE), which is used to account for inhomogeneous or imperfect capacitance, and is represented by the parameters Q and α , where Q is the capacitance impedance value and α represents the deviation from ideal capacitive behavior. The true capacitance (C) can be calculated from these parameters by the relationship $C = Q \omega_{\max}^{\alpha-1}$, where ω_{\max} represents the frequency at which the imaginary component reaches a maximum (f) Nyquist plot obtained from performing electrochemical impedance spectroscopy through the hydrogel, overlaid with the plot predicted from the equivalent circuit model (mentioned in (e)). Impedance was measured between 0.1 Hz and 10^6 Hz. (g) Values for all relevant parameters were extracted for the three hydrogel formulations by fitting their EIS data with the equivalent circuit model. (h, i, j) Real-time sensing performance of the 40% LiCl hydrogel as strain sensor in monitoring human activities. (h) Dynamic response to strain under repeated manual stretching of the hydrogel and variation of resistance during human activities of (i) finger bending and (j) wrist bending.

Furthermore, the conductivity of the 3D-printed hydrogels was also studied at low temperatures. The hydrogels act as electrical conductors, as demonstrated by connecting a light-emitting diode (LED) with a battery at room temperature (Figure 4- 6 c). Interestingly, the brightness of the emission did not observably change even when operated at – 80 °C with

the 40% LiCl hydrogel (Figure 4- 6 d). In contrast, the emission intensity markedly decreased for the WO LiCl hydrogel. These findings demonstrate strong ionic and electric transport capabilities even at subzero temperatures for the designer 3D-printed hydrogels presented here.

Electrochemical impedance spectroscopy (EIS) also serves as a responsive indicator for a broad spectrum of physical and chemical properties. There is currently a discernible trend toward the proliferation of impedimetric biosensors. The techniques of impedimetric analysis have been employed to distinguish the development of biosensors and to scrutinize the catalytic reactions of enzymes, nucleic acids, lectins, receptors, whole cells, antibodies, etc. Therefore, for bio-interfacing applications, it is essential to characterize the impedance of the hydrogel as the presence of ions in bodily fluids can additionally contribute to the conductivity of the printed hydrogel electrodes, particularly given the high liquid content of the hydrogels. To decouple ionic and electronic conductivities, we saturated the printed hydrogels in 1 M phosphate-buffered saline (PBS) solution and characterized their impedance using electrochemical impedance spectroscopy (EIS) in PBS as an electrolyte. The intercept of these EIS curves with the real axis is taken as the impedance of hydrogels. The data were fitted to the equivalent circuit model illustrated in Figure 4- 6 e, where R_e , R_c , and R_i represent the electronic resistance, charge transfer resistance, and ionic resistance of the cell assembly, respectively. Q and C represent the constant phase elements and capacitance arising from ionic conduction and double layer formation of the hydrogel, respectively. The two distorted semicircular shapes of the Nyquist plot suggest the presence of comparable ionic and electronic conductivities (refer Figure 4- 6 f and the inset). The parameters extracted from fitting the data to the equivalent circuit model confirm that the ionic and electronic resistances decreased with an increase in LiCl content in the hydrogel (Figure 4- 6 g). In the WO LiCl hydrogel, R_e is $1.075 \times 10^4 \Omega$,

and R_i is 2552 Ω , which decreases one order in the presence of LiCl. R_i sharply decreased to 219.7 Ω and 111.3 Ω for 10% LiCl and 40% LiCl, respectively. This demonstrates that the relative contribution of electronic conductivity to the overall impedance of the hydrogel decreases with the increase of the ionic component, Li^+ & Cl^- in the hydrogel system (Figure 4- 6 g). However, both resistances decrease due to the presence of LiCl in the hydrogel system. The improvement of this conductivity can be attributed to the following two effects. One contribution is that of Li^+ ions in the double network polymer hydrogel, and the other is the π electron conjugated polymer of PEDOT². As the LiCl content increased, more free electrons and ions led to more effective ion transport paths and enhanced ion diffusion kinetics.

6.3.8 Application of the hydrogel for human bodily motion detection

The developed hydrogel demonstrates significant potential as a sensor for monitoring both large-scale and minute human movements due to its excellent electrical conductivity and stretchability. To demonstrate this, we evaluated the sensing performance of a 40% LiCl hydrogel by measuring the changes in relative resistance with time during stretching of the hydrogel. The strain sensor exhibited sharp and rapid real-time changes in resistance in response to manual stretching of the hydrogel (Figure 4- 6 h) and large limb motions, including finger bends (Figure 4- 6 I) and wrist bends (Figure 4- 6 j). These results demonstrate that the 40% LiCl hydrogel-based sensors can be further developed and engineered for adoption in motion monitoring as strain sensors. Notably, the amplitude of finger and wrist bends can be distinctly identified by the width of the signal peak (Figure 4- 6 (i, j)). Furthermore, the signals for the same motion were very consistent, indicating the high sensitivity and superior recoverability of the hydrogel. The excellent sensing performance of the hydrogel suggests its capability to monitor motion in real-time and avoid mechanical damage caused by stretching.

Therefore, the hydrogel can be projected to serve as a stretch-assisted, safe, and precise strain sensor in various fields of application.

6.3.9 Shape-morphing parts: 4D printing

Whereas 3D printing of the ink has already been demonstrated to yield additively manufactured hydrogels of complex and intricate architectures, we next explored the ability to transform DLP-printed constructs in a programmable manner without cumbersome stimulation into shapes that may not be realizable through conventional 3D printing. This facile transformation of the 4D-printed structure is realized through the free deformation of the DLP-printed construct through mechanical peeling off the build plate (Figure 4- 7). The free deformation of the DLP-printed construct occurs spontaneously under the influence of the internal residual stresses that are generated from the layer-by-layer 3D printing process, obviating the need for an external stimulus (moisture, temperature, humidity, light, or electric/magnetic fields). The transformed structure post-DLP-printing retains its altered configuration even in aqueous environments, underscoring the method's simplicity in conferring a permanent transformation to the DLP-printed construct. Additionally, owing to the interplay of geometry and stress effects[27], the transformed construct exhibits far-from-equilibrium shape changes in ethanol. This unique characteristic can be strategically exploited to design dynamic constructs with diverse applications in the biomedical field.

The mechanism of the free-form deformation through mechanical peeling has been elucidated by Zhao et al. [28], albeit not in the context of DLP-based 3D printing. The photopolymerization of the hydrogel precursor is accompanied by volume shrinkage due to covalent bond formation between the monomers (acrylamide) and the crosslinkers (PF127-DA) and is more pronounced at higher crosslinking densities[29]. During the sequential layer-by-layer printing process, a

non-uniform stress gradient is generated, as described in an earlier study[30]. However, since the construct is physically constrained to the build, no deformation is observed at this stage. At the end of the printing process, the last cured layer experiences tensile residual stresses, and the first cured layer experiences compressive residual stresses. When peeled, the physical constraints preventing any shape change are removed, and the construct undergoes free-form deformation (Figure 4- 7 a). The tensile residual stresses result in contraction, while the compressive residual stresses result in expansion. This results in the construct bending with the last cured layer as the concave side (Figure 4- 7 (b, c)). It is important to note that the shrinkage-induced deformation is prominent at higher crosslinker concentrations (16 wt%) and essentially vanishes at lower crosslinker concentrations (4 wt%) when the volume shrinkage is less. At higher thicknesses, the bending stiffness increases, which makes it difficult to bend the rectangular beam. While the shrinkage-induced bending phenomenon is pronounced at a thickness of 1 mm with the beam curling onto itself from both ends, the bending is significantly less pronounced at thicknesses beyond 2 mm (Figure 4- 7 d). Thus, the thickness of the printed construct can be tuned to obtain the desired degree of deformation.

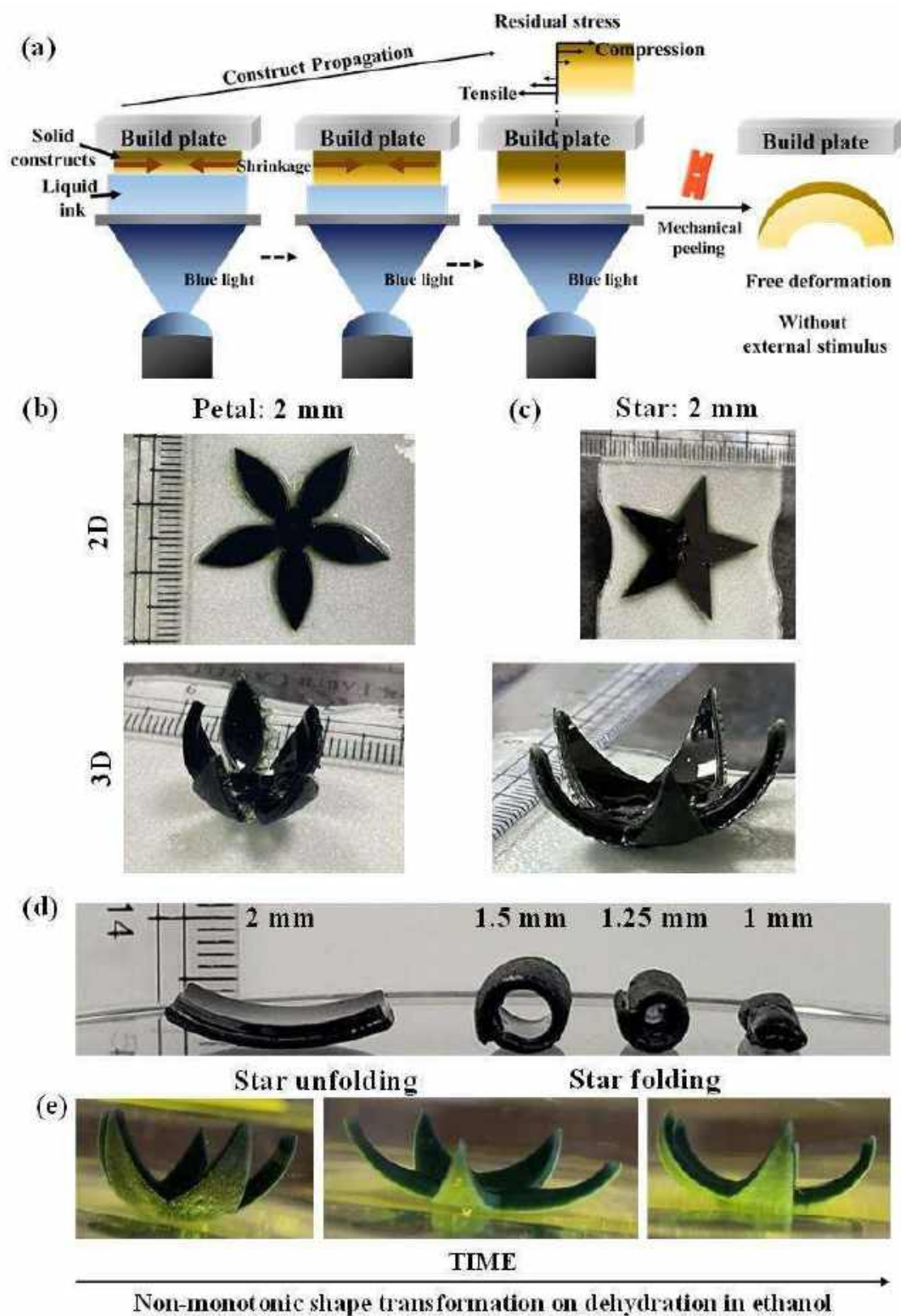


Figure 4- 7: (a) Schematic illustration depicting the free-form deformation of DLP-printed hydrogel on peeling. The 2D to 3D transformation of (b) a petal structure (c) a star structure on mechanical peeling. (d) The degree of curvature of a flat sheet is dependent on the thickness of the printed sheet, with the curvature decreasing with increasing thickness. (e) Non-monotonic shape changes exhibited by these hydrogels (unfolding and then folding again) on dehydration in alcohol.

Owing to mechanical programming, the curved shape presents a non-uniform stress state. The outer surface is in a state of tension, while the inner surface is in a state of compression. The diffusivity of water molecules into the hydrogel is strongly correlated with the stress state. Specifically, the water diffusivity can be expressed as $D = D_0 e^{\sigma_h \Omega / k_B T}$, where D_0 signifies the diffusivity under conditions of zero stress, σ_h denotes the hydrostatic stress derived from the trace of the stress tensor, Ω represents the activation volume governing water diffusion, and $k_B T$ corresponds to the thermal energy. Regions experiencing a state of tension (positive σ_h) exhibit higher water diffusivity, while regions experiencing a state of compression exhibit slower water diffusivity. The geometry plays a minor synergistic effect, with the outer surface experiencing faster diffusion due to the larger surface area. When the swollen hydrogels are placed in ethanol, they undergo dehydration, with the outer surface losing its water content faster than the inner surface due to faster diffusion as a consequence of both stress and geometry effects. This temporal difference in swelling kinetics causes the non-monotonic far-from-equilibrium shape-morphing behavior[27], which leads to the opening of the hydrogel structures as the outer surface experiences faster water loss and shrinks faster compared to the inner surface (Figure 4- 7 e). As a result, the outer surface reaches equilibrium earlier than the inner surface. Next, the construct returns to its initial shape as the inner surface reaches

equilibrium (Figure 4- 7 e). The ability to program (through peeling) and re-program the hydrogels (through dehydration in ethanol) is unique to this system, and such a phenomenon has not been reported in the literature. The programmability of these hydrogels makes them attractive candidates for applications in flexible electronics, biosensing, drug delivery, and tissue engineering.

6.3.10 *In vitro* cytocompatibility of hydrogels

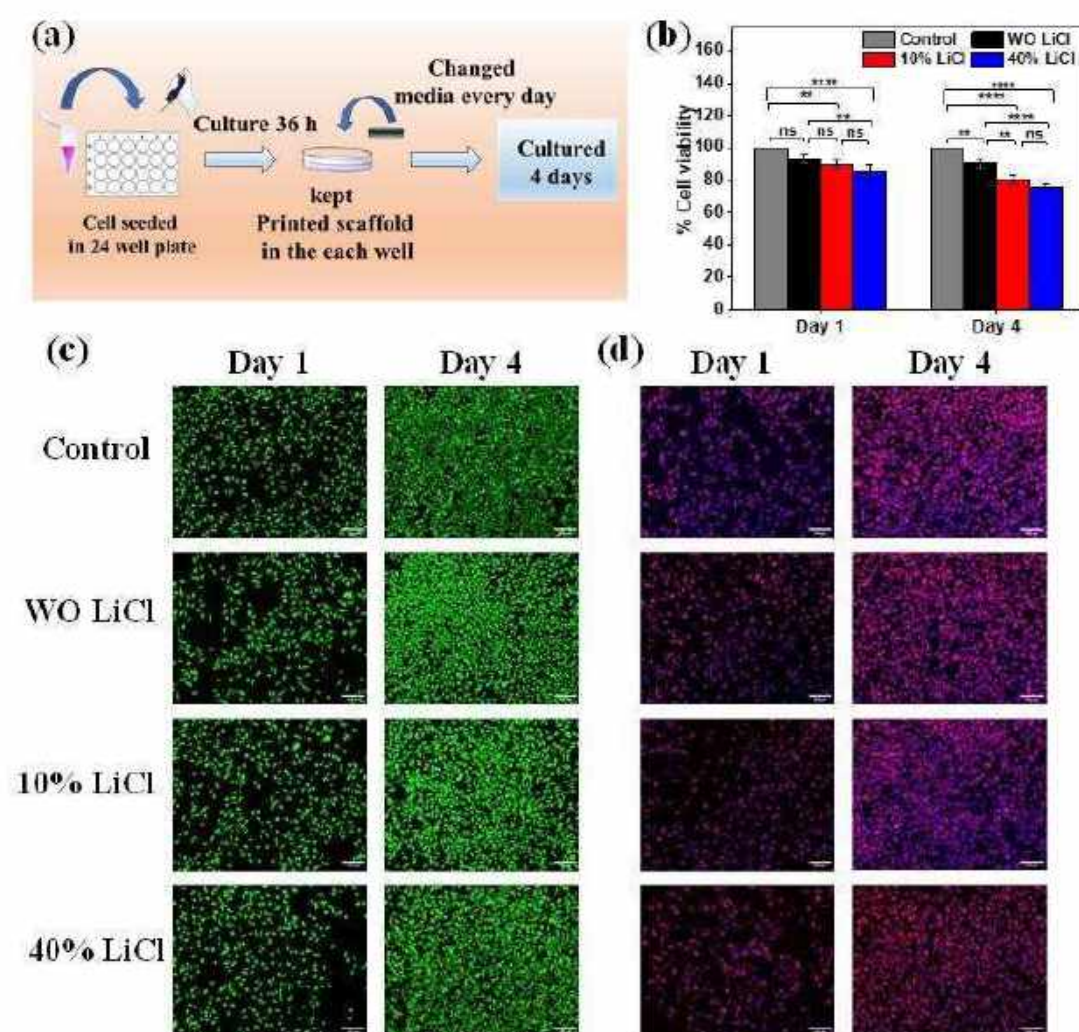


Figure 4- 8: Cytocompatibility assessment of the 3D-printed hydrogel structures against L929 mouse fibroblasts: (a) Scheme summarizing the experimental approach to evaluate the

cytotoxicity of the hydrogels. Cell viability was assessed with respect to the control (cells cultured in fresh medium) by (b) Alamar blue assay, (c) Live (green)- Dead (red) assay, and (d) F-actin (red) and nuclear (blue) imaging to evaluate cell morphology (Magnification 10 \times , scale bar = 100 μ m for all images of (c) and (d)). Ordinary 2-way ANOVA with Tukey's multiple comparisons test was performed for (b). ** indicates $p < 0.01$, **** indicates $p < 0.0001$, and ns indicates statistically non-significant.

Cytocompatibility is essential for applying the conducting hydrogel for biomedical and biosensor applications, particularly if implanted. We studied the cytocompatibility of the 3D-printed hydrogel constructs against L929 mouse fibroblasts (Figure 4- 8). Cells were seeded and cultured for 36 h, and then the 3D-printed gel was placed in the wells, as shown schematically in Figure 4- 8 a, and cultured further to evaluate the effect on the cells. Alamar blue assay revealed that more >80% of cells and >75% of cells were viable after exposure to the gels for 1 and 4 days, respectively, for all three hydrogel formulations (Figure 4- 8 b). However, on day 4, WO LiCl showed >90% cell viability, whereas viability was \approx 80% and \approx 76% for 10% LiCl and 40% LiCl hydrogels, respectively. Additionally, the Live-Dead assay was performed to independently validate toxicity qualitatively (Figure 4- 8 c). It was observed that most cells were alive (green), and the number of cells increased with time, which indicates cells are viable and continue to proliferate in the presence of the 3D-printed gels. However, the number of dead (red) cells increased marginally on day 4 for 40% LiCl gel. This may be due to the release of Li⁺ and Cl⁻ into the culture media. Furthermore, we also observed the morphology of the cells and compared them with the control groups by staining and imaging F-actin and nuclei (Figure 4- 8 d). It was seen that the cell morphology of the sample-treated groups was similar to that of the control group, and no distortion in morphology was observed

for WO LiCl and 10% LiCl gels. However, cells in the presence of the 40% LiCl gels showed some differences in morphology compared to the control group, which could be the effect of Li^+ and Cl^- ions. Taken together, these results suggest that cells are viable in the presence of the 3D-printed hydrogels developed here and could be explored for biomedical applications. More detailed in vivo investigations are warranted to establish the biocompatibility of the hydrogels for implantable applications.

6.4 Discussion

This work presents new polymeric ink formulations that are compatible with state-of-the-art manufacturing technologies, specifically DLP-based 3D printing, for fabricating highly conductive hydrogels with dual electronic and ionic conductivity and highly tunable mechanical properties. We compiled the salient properties of the recently developed conducting hydrogels described in the literature and the findings of this investigation in Table 4- 1 (qualitative summary) and Table 4- 3 (detailed comparison). The unique combination of highly sought properties makes our hydrogels promising candidate materials for integration into wearable and implantable devices, for which the ability to couple high electronic conductivity with low modulus to high modulus and high stretchability is particularly attractive and could also find use in soft robotics and machine-tissue interfaces particularly soft tissues such as the brain, cardiac tissues, and skeletal muscles. In addition, the ability to tune the mechanical properties of our hydrogel without compromising its conductivity makes it an attractive materials platform for various applications in the field of hydrogel-based electronics since it is well known that cells are highly responsive to the mechanical properties of their micro-environment. Our developed conducting hydrogels can provide a pathway for electrical stimulation and recording while maintaining the necessary 3D architecture and offering optimal

mechanical properties tailored for each tissue. These conducting hydrogels could also be developed to be seamlessly incorporated into application-specific devices by 3D printing processes, enabling diverse shapes and complex geometries tailored to specific target applications. Importantly, these hydrogels also exhibit freezing- and dehydration-tolerance properties and show excellent flexibility in extremely low temperatures, as low as -80°C . Therefore, the freezing- and dehydration-tolerant attributes incorporated into our 3D-printed hydrogels render their functionality and durability remarkable for the longer life span of use in terms of stretchability and conductivity concurrently. Another unique attribute of the ink formulation is that it is amenable to 4D printing to yield conducting hydrogels that can also undergo structural deformations in a programmable manner. The 3D-printed gels also show good cytocompatibility. Therefore, these all-in-one ink formulations developed here offer a unique combination of attractive attributes for potential use in diverse applications, including in extremely cold and hot working conditions, unlike the limited working conditions for other hydrogels, and we envisage its role in accelerating advancement in many fields.

Table 4- 1: Comparison of the multifunctional properties of the present study with reports in the literature

✓ and ✗ denote the presence and absence of the functional properties, respectively

	Additive manufacturing	Anti freezing	Dehydration tolerance	Flexibility	Cytocompatibility	4D deformation
Feig et al.	✗	✗	✗	✗	✗	✗
Zhang et al.	✓	✗	✗	✓	✗	✗
Fantino et al.	✓	✗	✗	✗	✗	✗
Jordan et al.	✓	✗	✗	✗	✗	✗
Cai et al.	✗	✓	✓	✗	✗	✗
Cheng et al.	✓	✗	✗	✓	✗	✗
Ge et al.	✗	✓	✓	✓	✗	✗
Chen et al.	✗	✓	✓	✓	✗	✗
Zhang et al.	✓	✗	✗	✓	✗	✗
Kaveh et al.	✗	✗	✗	✗	✓	✗
Larrea et al.	✓	✗	✗	✓	✗	✗
Zhu et al.	✓	✗	✗	✓	✗	✗
This Work	✓	✓	✓	✓	✓	✓

6.5 Conclusion

We have developed photopolymerizable and conductive PEDOT: PSS-based inks and utilized them for additive manufacturing by DLP-based 3D printing to fabricate multifunctional hydrogels. The rapid fabrication process of the 3D printing system involves developing hydrogel by integrating the interpenetrating primary network of PEDOT: PSS and in situ formation of the secondary network of polyacrylamide, which is simultaneously crosslinked with synthesized PF127DMA, which leads to a stable hydrogel network with the desired functionality without additional manufacturing steps. Additional key innovations lie in the multifunctionality of the 3D-printed hydrogels, including tunable mechanical properties, anti-freezing properties, and dehydration tolerance ability through the strong interaction of Li^+ and Cl^- ions with polymer networks. The 3D-printed hydrogels exhibit remarkable mechanical stretchability (% elongation up to 1000%), superior toughness ($\sim 114 \text{ kJ m}^{-3}$), durability

(outstanding fatigue resistance, resilience, and cyclic stability), exceptional anti-freezing properties (until -80°C), and excellent conductivity ($\approx 3.57 \text{ S.m}^{-1}$) and impedance characteristics. Additionally, the 3D-printed constructs can exhibit programmable 4D deformations. The 3D-printed hydrogels demonstrate favorable cytocompatibility in vitro. Given the attractive combination of attractive properties, these 3D/4D-printed hydrogels are promising candidates for application across diverse domains, particularly bio-electronic applications in healthcare and other fields.

Table 4- 2: List of ink compositions used for preparation of 1 mL ink

Nu mbe r	Ink	PEDOT: PSS polymer solution (μL)	Acryla mide (Wt%)	PF127 DMA (Wt%)	LiCl (Wt %)	DMSO (μL)	Glycerol (μL)	Photo initiator (μL of 3 wt% of LAP solution)	Photo absorber (μL of 30 mM of Tartazine)
1	PEDOT:PSS/10% AM/2% PF127DMA	850	10	2	0	130	20	50	25
2	PEDOT:PSS/20% AM/2% PF127DMA	850	20	2	0	130	20	50	25
3	PEDOT:PSS/30% AM/2% PF127DMA	850	30	2	0	130	20	50	25
4	PEDOT:PSS/40% AM/2% PF127DMA	850	40	2	0	130	20	50	25
5	PEDOT:PSS/50% AM/2% PF127DMA	850	50	2	0	130	20	50	25
6	PEDOT:PSS/40% AM/0.5 %PF127DMA	850	40	0.5	0	130	20	50	25
7	PEDOT:PSS/40% AM/1% PF127DMA	850	40	1	0	130	20	50	25
8	PEDOT:PSS/40% AM/2% PF127DMA	850	40	2	0	130	20	50	25
9	PEDOT:PSS/40% AM/4% PF127DMA	850	40	4	0	130	20	50	25
10	PEDOT:PSS/40% AM/8% PF127DMA	850	40	8	0	130	20	50	25
11	PEDOT:PSS/40% AM/16% PF127DMA	850	40	16	0	130	20	50	25
12	PEDOT:PSS/40% AM/16% PF127DMA/ 10% LiCl	850	40	16	10	130	20	50	25
13	PEDOT:PSS /40% AM/16%PF127DMA/ 40 % LiCl	850	40	16	40	130	20	50	25

Table 4- 3: Comparison of our developed conducting hydrogel properties here with reports in the literature. (NA is not available)

Sl. No.	Materials	Additive manufacturing & Techniques	Mechanical tunability	Anti freezing	Dehydration tolerance	Conductivity ($S\ m^{-1}$)	Flexibility	Cytocompatibility	4D deformation	Comments	Ref
1	PEDOT: PSS, Acrylic acid, Bisacrylamide, Ionic liquid	No	Yes	No	No	12 to 23	No	NA	No	<ul style="list-style-type: none"> Difficult to prepare complex structures and geometries through casting. 	Feig et al.[2]
2	Acrylamide, poly (ethylene glycol) dimethacrylate (PEGDMA) and potassium chloride (KCl)	Yes, Micro- stereolithography technology	Yes	No	No	Frequence- dependent conductivity measured	Yes	NA	No	<ul style="list-style-type: none"> Very low conductivity due to the absence of conducting polymer matrix (conductivity comes from only K^+ and Cl^- ions), Low strength. 	Zhang et al.[1]

3	poly (ethylene glycol) diacrylate, polypyrrole, FeCl ₃	Yes, DLP	No	No		0.0074	NA	NA	NA	<ul style="list-style-type: none"> Additional post-printing step required to impart conductivity. 	Fantino et al.[31]
4	2-Acrylamido-2-methyl-1-propanesulfonic acid (AMPSA), acrylamide, N, N-methylenebis (acrylamide) (MBAA)	Yes, stereolithography (SLA) technology	Yes	No	No	0.53	No	NA	NA	<ul style="list-style-type: none"> Additional step required for surface polymerization of the conducting polymer on the 3D printed constructs 	Jordan et al.[32]
5	Poly (acrylamide - co-acrylic acid), Trehalose, and LiCl	NO	Yes	Yes, up to -20° C	Yes	2 to 3	No	NA	NA	<ul style="list-style-type: none"> Difficult to prepare complex constructs using casting technique. Challenging to tune mechanical properties with reported compositions. 	Cai et al.[26]

6	PEDOT: PSS, poly (2-hydroxyethyl acrylate-isobornyl acrylate)	Yes, DLP	NA	No	No	0.312	Yes	NA	NA	<ul style="list-style-type: none"> Additional steps (soaking in an EDOT solution followed by polymerization) required to impart conductivity 	Cheng et al.[33]
7	Acrylamide, cellulose Nanofibrils, LiCl	No	No	Yes, up to -80°C	Yes	2.25	Yes	NA	NA	<ul style="list-style-type: none"> Difficult to prepare complex structures and geometries using the casting technique, Challenging to tune the mechanical properties, Absence of conducting polymeric network (only ionic conductivity), Cannot be used in impedance-based biosensor applications due to only ionic conductance. 	Ge et al.[25]

8	Polyvinyl alcohol bearing styrylpyridinium groups, sodium alginate, ferric chloride, glycerol	NO	Yes	Yes, up to -40° C	Yes	0.38	Yes	NA	NA	Similar to the previous study	Chen et al.[16]
9	ionic monomer made of acrylic acid (AAc) and choline chloride (CCl) complex, poly (ethylene glycol) diacrylate (PEGDA), Nanoclay	Yes, DLP	NA	NA	NA	0.43	Yes	NA	NA	<ul style="list-style-type: none"> • Conduction ionoelastomer is stiffer, • Absence of conducting polymeric network, • No additional advantages. 	Zhang et al.[34]
10	PEDOT: PSS, Collagen 1, Na-Alginate	NO	NA	NA	NA	0.35	NA	Yes	NA	<ul style="list-style-type: none"> • Difficult to prepare complex structures and geometries using the casting technique, • No additional advantages apart from conductivity and cytocompatibility. 	Kaveh et al.[7]

11	PEDOT: PSS, poly (ethylene glycol) diacrylate, ethylene glycol	Yes, DLP	NA	NA	NA	0.71	Yes	NA	NA	<ul style="list-style-type: none"> Apart from 3D printing, this conducting hydrogel system has no additional advantages in terms of water-holding capability, anti-freezing properties, etc. 	Larrea et al.[35]
12	PEDOT: PSS, Acrylamide, poly (ethylene glycol) diacrylate	Yes, stereolithography	Yes	NA	NA	0.08 to 1.7	Yes	NA	NA	This study also has disadvantages similar to those of (11) above	Zhu et al.[36]
13	PEDOT: PSS, acrylamide, PF127DMA, LiCl	Yes, DLP	Yes	Yes, up to -80° C	Yes	1.22 to 3.57	Yes	Yes	Yes	Multifunctional hydrogel with tunable mechanical properties, anti-freezing and dehydration tolerance properties, flexibility, good cytocompatibility, and, most importantly, programmable 4D deformation.	This Work

6.6 References:

1. Zhang, Y., et al., *Ultra-fast programmable human-machine interface enabled by 3D printed degradable conductive hydrogel*. Materials Today Physics, 2022. **27**: p. 100794.
2. Feig, V.R., et al., *Mechanically tunable conductive interpenetrating network hydrogels that mimic the elastic moduli of biological tissue*. Nature communications, 2018. **9**(1): p. 2740.
3. Patel, D.K., et al., *Highly stretchable and UV curable elastomers for digital light processing based 3D printing*. Advanced Materials, 2017. **29**(15): p. 1606000.
4. Zhou, Y., et al., *Highly stretchable, elastic, and ionic conductive hydrogel for artificial soft electronics*. Advanced Functional Materials, 2019. **29**(1): p. 1806220.
5. Yang, H., W.R. Leow, and X. Chen, *3D printing of flexible electronic devices*. 2018, Wiley Online Library: Small Methods. p. 1700259.
6. Bansal, M., et al., *Conducting polymer hydrogels for electrically responsive drug delivery*. Journal of controlled release, 2020. **328**: p. 192-209.
7. Roshanbinfar, K., et al., *Electroconductive biohybrid hydrogel for enhanced maturation and beating properties of engineered cardiac tissues*. Advanced Functional Materials, 2018. **28**(42): p. 1803951.
8. Ge, Q., et al., *3D printing of highly stretchable hydrogel with diverse UV curable polymers*. Science advances, 2021. **7**(2): p. eaba4261.
9. Yang, R., et al., *3D-printed conducting polymer hydrogel-based DC generator for self-powered electromechanical sensing*. Nano Energy, 2023. **117**: p. 108857.
10. Greer, J.R. and V.S. Deshpande, *Three-dimensional architected materials and structures: Design, fabrication, and mechanical behavior*. MRS Bulletin, 2019. **44**(10): p. 750-757.
11. Surjadi, J.U., et al., *Mechanical metamaterials and their engineering applications*. Advanced Engineering Materials, 2019. **21**(3): p. 1800864.
12. Peng, S., et al., *3D printing mechanically robust and transparent polyurethane elastomers for stretchable electronic sensors*. ACS applied materials interfaces, 2020. **12**(5): p. 6479-6488.
13. Nadernezhad, A., et al., *Multifunctional 3D printing of heterogeneous hydrogel structures*. Scientific reports, 2016. **6**(1): p. 33178.

14. Sui, X., et al., *Ionic conductive hydrogels with long-lasting antifreezing, water retention and self-regeneration abilities*. Chemical Engineering Journal, 2021. **419**: p. 129478.
15. Jian, Y., et al., *Biomimetic anti-freezing polymeric hydrogels: keeping soft-wet materials active in cold environments*. Materials Horizons, 2021. **8**(2): p. 351-369.
16. Chen, D., et al., *Anti-freezing, tough, and stretchable ionic conductive hydrogel with multi-crosslinked double-network for a flexible strain sensor*. Chemical Engineering Journal, 2024. **480**: p. 148192.
17. Feng, Y., et al., *Entanglement in Smart Hydrogels: Fast Response Time, Anti-Freezing and Anti-Drying*. Advanced Functional Materials, 2023. **33**(21): p. 2211027.
18. Liu, J., et al., *Ionic conductive organohydrogels with dynamic pattern behavior and multi-environmental stability*. Advanced Functional Materials, 2021. **31**(24): p. 2101464.
19. Wu, Z., X. Yang, and J. Wu, *Conductive hydrogel-and organohydrogel-based stretchable sensors*. ACS Applied Materials Interfaces, 2021. **13**(2): p. 2128-2144.
20. Criado-Gonzalez, M., et al., *Additive manufacturing of conducting polymers: recent advances, challenges, and opportunities*. ACS Applied Polymer Materials, 2021. **3**(6): p. 2865-2883.
21. Zhao, Q., et al., *Robust PEDOT: PSS-based hydrogel for highly efficient interfacial solar water purification*. Chemical Engineering Journal, 2022. **442**: p. 136284.
22. Dominguez-Alfaro, A., et al., *Electroactive 3D printable poly (3, 4-ethylenedioxythiophene)-graft-poly (ϵ -caprolactone) copolymers as scaffolds for muscle cell alignment*. Polymer Chemistry, 2022. **13**(1): p. 109-120.
23. Dominguez-Alfaro, A., et al., *3D Printable Conducting and Biocompatible PEDOT-graft-PLA Copolymers by Direct Ink Writing*. Macromolecular Rapid Communications, 2021. **42**(12): p. 2100100.
24. Lu, B., et al., *Pure pedot: Pss hydrogels*. Nature communications, 2019. **10**(1): p. 1043.
25. Ge, W., et al., *Nanocellulose/LiCl systems enable conductive and stretchable electrolyte hydrogels with tolerance to dehydration and extreme cold conditions*. Chemical Engineering Journal, 2021. **408**: p. 127306.
26. Cai, H., et al., *Trehalose-enhanced ionic conductive hydrogels with extreme stretchability, self-adhesive and anti-freezing abilities for both flexible strain sensor and all-solid-state supercapacitor*. Chemical Engineering Journal, 2023. **472**: p. 144849.

27. Zhang, Y., et al., *Differential diffusion driven far-from-equilibrium shape-shifting of hydrogels*. Nature Communications, 2021. **12**(1): p. 6155.
28. Zhao, Z., et al., *Origami by frontal photopolymerization*. Science advances, 2017. **3**(4): p. e1602326.
29. Bowman, C.N. and C.J. Kloxin, *Toward an enhanced understanding and implementation of photopolymerization reactions*. AIChE Journal, 2008. **54**(11): p. 2775-2795.
30. Huang, Y.-M. and C.-P. Jiang, *Curl distortion analysis during photopolymerisation of stereolithography using dynamic finite element method*. The International Journal of Advanced Manufacturing Technology, 2003. **21**: p. 586-595.
31. Fantino, E., et al., *3D printing/interfacial polymerization coupling for the fabrication of conductive hydrogel*. Macromolecular Materials Engineering, 2018. **303**(4): p. 1700356.
32. Jordan, R.S., et al., *3D printed architected conducting polymer hydrogels*. Journal of Materials Chemistry B, 2021. **9**(35): p. 7258-7270.
33. Cheng, X.-Y., et al., *3D-printed stretchable sensor based on double network PHI/PEDOT: PSS hydrogel annealed with cosolvent of H₂O and DMSO*. 2023. **470**: p. 144058.
34. Zhang, C., et al., *3D printed, solid-state conductive ionoelastomer as a generic building block for tactile applications*. Advanced Materials, 2022. **34**(2): p. 2105996.
35. Lopez-Larrea, N., et al., *Digital light 3D printing of PEDOT-based photopolymerizable inks for biosensing*. ACS Applied Polymer Materials, 2022. **4**(9): p. 6749-6759.
36. Zhu, H., et al., *3D printing of conductive hydrogel–elastomer hybrids for stretchable electronics*. 2021. **13**(49): p. 59243-59251.

Summary of the research work

Summary and future perspective

7.1 Summary

In this research work, various multifunctional self-healing injectable hydrogels were fabricated, and their functionality was systematically investigated to assess their potential for advanced biomedical applications. Additionally, novel hydrogel inks and innovative 4D (bio)printing techniques were developed to demonstrate the shape-morphing behavior of the fabricated hydrogel constructs for advanced clinical application necessitating smart, deployable devices and constructs. The findings of the work presented in this research offer information for the engineering of next-generation injectable hydrogels and smart shape-morphing hydrogels to address the current unmet clinical challenges for improved healthcare.

The first part of the research focused on synthesizing and engineering the polysaccharide-based self-healing injectable hydrogel with multifunctional properties developed as a delivery vehicle in minimally invasive procedures. Single (covalent crosslinking) and double network hydrogels (covalent crosslinking along with ionic crosslinking) were engineered. The double network hydrogels showed significantly superior gelation time and excellent fracture strength along with excellent self-healing efficiency in contrast to the single network hydrogel due to dynamic Schiff-base bonds and ionic crosslinks. The degradation behavior and drug release kinetics from the hydrogels were dependent on the local conditions. The *in vitro* cell study demonstrated that fabricated hydrogels were cytocompatible and can find applications in cell encapsulation. The degradation rate and sustained release profile of antibiotic and anticancer drugs from the hydrogel demonstrated significant efficacy against bacterial and cancer growth, respectively. These results suggest that the degradable and injectable hydrogels developed here could find promising clinical applications for encapsulating and releasing cells and drugs. However, the developed hydrogel lacked intrinsic bioactivity such as antibacterial, antioxidant

properties, and other clinically desirable characteristics, which may lower their potential in applications associated infections.

Therefore, we developed a generalized, facile approach for surface modification of nanomaterials with a bioligand and designed the chemistry to covalently crosslink the particles with a degradable polysaccharide-based injectable hydrogel network that exhibits multifunctional attributes, including self-healing ability, flexibility, and antibacterial properties along with ROS scavenging ability. We synthesized CuO and ZnO nanoparticles and functionalized them with folic acid bioligand to demonstrate the broad applications of our generic approach of surface modification to a wide variety of nanoparticles. Specifically, bioligand-modified CuO nanosheets were incorporated to modify the properties of the hydrogel, and their potential functionality was evaluated. Furthermore, the optimized formulation of our F-CuO-embedded injectable hydrogel exhibited excellent cytocompatibility, blood compatibility, and *in vitro* wound healing performance. Taken together, the F-CuO nanosheet crosslinked injectable hydrogel composite presented herein is shown to be a promising candidate biomaterial with multifunctional properties to develop solutions for addressing chronic clinical challenges.

Whereas injectable hydrogels show great promise, a notable limitation lies in their inability to generate intricate 3D structures with precise spatial control and resolution, essential for applications such as *ex vivo* tissue models, personalized healthcare devices, deployable devices, robotic surgery, and other related biomedical fields. Therefore, in the second part of this thesis, we developed a novel 4D (bio)printing approach that employs biocompatible and versatile biomaterial ink design to encode two opposing shape transformations. These transformations proceed sequentially through the application of only a single initial mild stimulation (water

uptake). To realize this objective, we conceived an innovative 4D shape-morphing strategy in which the activation of the second actuation mechanism occurs as a direct consequence of the conditions established upon completion of the first actuation mechanism, eliminating the need for any secondary external stimulation. We implemented this concept by 3D printing semi-IPN hydrogels, which exhibit a gradient in photocrosslinking density and undergo anisotropic water uptake when immersed in water. This differential water swelling not only triggers the first shape transformation but also sets up an internal osmolarity gradient that drives the second shape transformation in the opposite direction. Our proposed 4D mechanism is material agnostic and can be realized through a multitude of semi-IPN compositions, thereby broadening its scope of application. We also demonstrated how this unique shape-morphing behavior can be leveraged to fabricate pre-programmed, deployable hydrogel devices that are not realizable via current approaches. By achieving multi-step shape transformations on a single stimulation, our developed shape-morphing strategy holds significant promise for automating complex functions by minimizing external interventions and can facilitate the development of smart solutions for outstanding biomedical challenges.

Finally, the potential applications of additively manufactured hydrogel structures extend beyond the realm of tissue regeneration, with further promising use cases in soft robotics, biosensors, human-machine interfaces, wearable devices, and engineered living systems. To this end, we developed a novel hydrogel prepared by DLP-based 3D printing technology with visible light, possessing anti-freezing properties, electrical conductivity, excellent toughness and stretchability, and biocompatibility. The printed conducting hydrogels have good water-holding capability at ambient conditions and freezing tolerance competence over a wide range of temperatures ranging from -80 to 45 °C. The inks are amenable to the manufacturing of 4D-

printed hydrogels that can elicit pre-programmed structural deformations. Collectively, this work presents new material formulations for designing ultrafast programmable electronic devices with printed hydrogel electronics for various applications and can perform under extreme environmental conditions.

In summary, the work presented in this thesis is critically important for developing tunable, multifunctional, affordable, self-healing injectable hydrogel systems and 4D printable inks and techniques that will find applications in healthcare, biosensors, and soft robotics for addressing clinical needs.

7.2 Scope for future work

(i) Scope for the advancement of injectable hydrogel

There are still several challenges that need to be addressed. In order to address issues with current injectable hydrogels, such as adhesive properties with inadequate adhesion in wet physiological conditions, tunable degradation kinetics, mechanical strength, and dependency on traditional closure techniques, there is an urgent need to develop novel injectable bioadhesive agents. Clinical requirements for injectable adhesives hydrogel are multifaceted for use in various environments. In addition, several surgical processes need to seal two dissimilar types of surfaces with a significant difference in their materials properties, such as attaching prostheses to bone surfaces, fixing the tendon to bone, and bonding heart patches to heart surfaces. Hence, there is a large unmet potential need for developing interfacial materials with graded mechanical properties and transitional composition to minimize stress concentration associated with contact deformation and secondary trauma to the soft tissues. Unfortunately, until now, there are no reported synthetic injectable bioadhesive hydrogels with such graded composition and characteristics. In the long term, research and development in

this field should focus on the critical areas that need improvement. Notably, one of the fundamental goals of developing the new multifunctional injectable hydrogel is clinical translation and commercialization. Therefore, development of new injectable hydrogel systems should be undertaken in close collaboration with clinicians to identify and meet the specific medical challenges and demands and validate them through relevant preclinical testing.

(ii) Scope for the advancement of 4D printing

Similarly, in the case of 4D printing of hydrogels, there are many unmet needs despite the emergence and rapid advancement in this field owing to its extensive applicability across various research fields. Further developments will require advancements in responsive chemical compositions, novel synthesis methodologies, and post-processing techniques to confer shape-morphing capabilities. Additionally, materials and mechanisms can be fused to enable sophisticated functionalities. In the realm of biomedicine, significant attention has been directed toward utilizing biocompatible materials based on these principles. However, there has been a notable absence of a focused application-oriented approach. Clinical application considerations are often lacking, leading to design processes devoid of clinical insights. Consequently, despite significant advancements, state-of-the-art 4D printing technologies remain largely in proof-of-concept stages and have not attained commercial viability. To address this challenge, a thorough investigation is necessary to discern how existing 4D printing methodologies can effectively tackle defined clinical challenges. Again, this endeavor should entail close collaboration with clinicians to ascertain material selection, specific shape transformations, suitable actuation methods, actuation forces, and biocompatibility criteria for each application. Combining experimental approaches with computational methods such as finite element modeling can provide more robust insights in a quicker time frame. Existing

experimental data can be used to train machine learning and deep learning algorithms to predict shape changes, design material and energy-efficient shape modifications, and navigate the vast design space for optimal solutions.

S

List of Publications and Conference presentations

Publications included in this thesis

Peer-reviewed journal articles (in reverse chronological order)

1. **Mondal, P.**, Mandal, A. and Chatterjee, K., 2024. “All-in-one” ink for light-based 4D printing of conducting, tough, anti-freezing, and cytocompatible hydrogels. *Chemical Engineering Journal*, p.153883.
2. **Mondal, P.** and Chatterjee, K., 2024. Multibiofunctional Self-healing Adhesive Injectable Nanocomposite Polysaccharide Hydrogel. *Biomacromolecules*.
3. **Mondal, P.**, Mandal, A. and Chatterjee, K., 2023. Bi-Directional Shape Morphing in 4D-Bioprinted Hydrogels on a Single Stimulation. *Advanced Materials Technologies*, 8(19), p.2300894.
4. **Mondal, P.**, Chakraborty, I. and Chatterjee, K., 2022. Injectable Adhesive Hydrogels for Soft tissue Reconstruction: A Materials Chemistry Perspective. *The Chemical Record*, 22(11),p.e202200155.
5. **Mondal, P.** and Chatterjee, K., 2022. Injectable and self-healing double network polysaccharide hydrogel as a minimally-invasive delivery platform. *Carbohydrate Polymers*, 291, p.119585.

Other publications (in reverse chronological order)

1. Kumari, S., **Mondal, P.**, Tyeb, S. and Chatterjee, K., 2024. Visible light-based 3D bioprinted composite scaffolds of κ -carrageenan for bone tissue engineering applications. *Journal of Materials Chemistry B*, 12(7), pp.1926-1936.
2. Kumari, S., **Mondal, P.** and Chatterjee, K., 2022. Digital light processing-based 3D bioprinting of κ -carrageenan hydrogels for engineering cell-loaded tissue scaffolds. *Carbohydrate Polymers*, 290, p.119508.
3. Rajput, M., **Mondal, P.**, Yadav, P. and Chatterjee, K., 2022. Light-based 3D bioprinting of bone tissue scaffolds with tunable mechanical properties and architecture from photocurable silk fibroin. *International Journal of Biological Macromolecules*, 202, pp.644-656.

4. Ghosh, S., **Mondal, P.**, Vel, B.R. and Chatterjee, K., 2020. Effect of dual crosslinking on physico-chemical properties of hydrogels prepared from chitosan and alginate. *Journal of Metallurgy and Materials Science*, 62(3and4), pp.31-40.

Patents included in this thesis (*in reverse chronological order*)

1. Mondal, P., Mandal A., Chatterjee, K. (2024) A printable conducting ink composition, a three-dimensional hydrogel, and implementations thereof (Indian Patent No. 202441019308). IPTel India office
2. Mondal, P., Mandal A., Chatterjee, K. (2023) A 4D Printed Hydrogel, Method of Preparation, And Implementations Thereof (Indian Patent No. 202341028595). IPTel India office

Other Patents— (*in reverse chronological order*)

3. Kumari, S., Mondal, P., Chatterjee, K. (2023). A Photocurable Ink Composition for Bioprinting and Methods Thereof (Indian Patent No. 202341018932). IPTel India office.
4. Chakraborty, I., Mondal, P., Maity, S., Chatterjee, K., and Bose, S. (2021). A method for preparation of Polyurethane composite material and composites thereof (Indian Patent No. 202141038867). IPTel India office.

List of conference presentations

1. Pritiranjana Mondal & Kaushik Chatterjee (2023) “Nanoparticle impregnated injectable and self-healing polysaccharide-based hydrogel system with multi biofunctional properties for biomedical applications” (poster presentation) materials today conference 2023, Singapore.
2. Pritiranjana Mondal & Kaushik Chatterjee (2023) “Injectable and self-Healing double network polysaccharide hydrogel as a minimally invasive delivery platform” (poster presentation) IWAM 2023, Dubai, United Arab Emirates.

Declaration

I, Pritiranjana Mondal, hereby declare that I am the first (main) author of this research work titled “*Multifunctional hydrogels with injectable, self-healing, and shape-morphing capabilities for biomedical applications*” and that the work reported here has been carried out by me at the Department of Materials Engineering, Indian Institute of Science, Bangalore, India, under the supervision of Prof. Kaushik Chatterjee.

August 2024

Indian Institute of Science, Bangalore

A rectangular box containing a handwritten signature in dark ink. The signature is written in a cursive style and appears to read 'Pritiranjana Mondal'.

Pritiranjana Mondal